High-resolution Direct Stochastic Optical Reconstruction Microscopy of the human kinetochore chromatin

Dissertation

zur Erlangung des akademischen Grades doctor rerum naturalium

(Dr. rer. nat)

vorgelegt dem Rat der Chemisch-Geowissenschaftlichen Fakultät der
Friedrich-Schiller-Universität Jena
von Dipl. Ing. Šumanovac Šestak Ivana
geboren am 4.Dezember 1983. in Zagreb, Kroatien

Gutachter:

1. Prof. Dr. Rainer Heintzmann, Chemisch-Geowissenschaftliche Facultät, Friedrich-Shiller-Universität Jena
2. Prof. Dr. med. Thomas Cremer, Facultät für Biologie, Ludwig-Maximilians-Universität München

Tag der Verteidigung: 26.8.2020

Abstract

The kinetochore is a chromatin-protein complex on the chromosome centromere. Kinetochore attache chromosomes to the microtubules of the spindle apparatus, recognize attachment to microtubules, and regulate the progress of mitosis. The kinetochore protein complex is built on the periphery centromere chromatin. It seems that kinetochores react to forces of the spindle apparatus microtubules in their interior. Due to the limited resolving power of the optical microscope and limitations of electron microscopy, the spatial arrangement of kinetochore protein and chromatin complex is unresolved. In this thesis, the human periphery centromere chromatin assembled with CENP-A (kinetochore chromatin in further text), on which kinetochore complex is built, was imaged by high-resolution optical microscopy called direct Stochastic Optical Reconstruction Microscopy (*d*STORM). Resolving power of less than 30 nm was achieved, and the architecture of more than 900 kinetochores in different sub-stages of interphase and mitosis was resolved.

Kinetochore chromatin was formed in a rectangle between 250 and 400 nm long and between 150 and 270 nm wide. It was composed of parallel and orthogonal lines between 12 and 75 nm wide. The arrangement of kinetochore chromatin in mitosis was narrower and longer than in interphase. In interphase, subtle changes in the dimensions of kinetochore lines were measured. The mitotic toxin nocodazole disturbed kinetochore chromatin organization. The discovered change of arrangement of the kinetochore chromatin assembled with CENP-A during the cell cycle could be the physical mechanism of recognition of proper attachment and positioning of the chromosomes at the equatorial plate. Based on the discovered kinetochore structure and behavior in the cell cycle, a new shoo-lace model of assembly and function of kinetochore chromatin is suggested.

Contents

Introduction

The role of centromeres and kinetochores

In mitosis of eukaryotes, the hereditary molecules in the form of chromosomes attach to the spindle apparatus microtubules at their narrowed part called the centromere. A chromatin-protein complex called the kinetochore is formed on the centromere. Kinetochores attach chromosomes to the spindle apparatus microtubules and participate in the alignment of chromosomes at the equatorial plate and in the separation of sister-chromatids into daughter cells. On the electron-microscopic images of the kinetochore, it is possible to distinguish three layers of different density (Luykx, 1965; Brinkley and Stubblefield, 1966; and Jokelainen, 1967). In the kinetochore, there are more than 80 different centromere-kinetochore proteins distributed in three groups: the Constitutive Centromere Associated Network (CCAN) super complex, the Knl1-Mis12-Ndc80 (KMN) super complex, and the Spindle Assembly Checkpoint (SAC). Even though much is known about the function of specific kinetochore proteins, their spatial arrangement is unknown. The recent progress of techniques of optical microscopy with high resolving power enables a ten-fold increase of optical microscope resolution up to 20 nm or better. With the application of these techniques, the architecture of the centromere chromatin and the kinetochore, as well as the internal arrangement of its proteins, might be distinguished, and their function could be better understood.

Genetic and epigenetic characteristics of the kinetochore chromatin

Kinetochore DNA on the centromere contains specific sequences of nucleotides. Kinetochore DNA of vertebrates occupies a region of chromosomes and vertebrate kinetochores attach to the microtubule fiber made up of around 20 microtubules. The human kinetochore DNA contains a specific sequence 171 base pairs long called the α-satellite and a sequence called CENP-B Box. Together they create complex iterations (Earnshaw and Rothfield 1985, Masumoto et al. 1989). Despite the specific centromere sequence, the centromere narrowing and the functional human kinetochore can be formed on the parts of chromosomes without the α-satellites (Amor and Choo 2002), and the place of their formation is determined epigenetically. Functional centromeres without alpha DNA, called neocentromeres have been clinically detected in about a hundred cases of healthy people and specific sequences are not necessary for the formation of the functional kinetochore (Marshall et al. 2008.). In the text below, I will write about the human kinetochore unless specified otherwise.

All functional eukaryotic kinetochores contain specific centromere histones, variants of the H3 histone. In humans, this protein is called Centromere protein A (CENP-A), and it transfers the information about the place of formation of the future kinetochore (see Mellone and Allshire 2003; Black and Bassett 2008, Santaguida and Mussachio 2009). The CENP-A is located in intermittent regions along the centromere DNA, and its regions alternate with the regions of the classic H3 histone (Blower et al. 2002 Ribeiro et al. 2010, see Allshire and Karpen 2008). CENP-A forms an octamer with other histone proteins (Hasson et al. 2013), and the crystallographic structure of

$(CENP\text{-}A\ H4)_2$ tetramers is well known (Sekulić et al. 2010). CENP-A is incorporated in centromeres in the G1 phase of the cell cycle by the recognition of its domain called the Centromere Targeting Domain (CATD) (Black et al. 2004).

Centromere sequences evolve quickly, and they are very diverse amongst closely related species. Kinetochore proteins are exceptionally variable amongst species in their composition and number, despite its essential and conserved role. The theory of centromere drive connects evolutionary development and the diversity of centromeres and kinetochores with their mechanical role. According to this theory, a change of the centromere sequence and kinetochore proteins can give to the chromosome a selective advantage in asymmetric female meiosis due to the improved mechanical characteristics. The centromere sequence and centromere histone constantly adjust to one another to optimize mechanical characteristics and increase the chance to be transferred to the oocyte and the next generation (Hernikoff, Malik 2002).

The composition and function of kinetochore proteins on the centromere

Biochemical and molecular research of centromere and kinetochore proteins began with the discovery of anti-centromere antibodies (ACA) in the serum of patients with autoimmune disease scleroderma. The ACA specifically recognizes Centromere proteins A, B, and C (Earnshaw and Rothfield, 1985). The centromere chromatin with about 17 so far known proteins forms a complex network called the Constitutive Centromere Associated Network (CCAN). In mitosis, other kinetochore proteins of the Knl-1 -Mis-12- Ndc 80 (KMN) supercomplex attach to this network, and that way attach the kinetochore with the spindle apparatus microtubules. Besides microtubules, the proteins of the biochemical signal network Spindle Assembly Checkpoint (SAC) also attach to the KMN super complex. The SAC postpones the progress of mitosis and the anaphase until all chromosomes are correctly attached to the spindle (rev. in Santaguida and Musacchio 2009). The Constitutive Centromere Associated Network (CCAN) is present on the centromere during the whole cell cycle, the Mis12 complex and the Kinetochore Null 1 (KnL1) occupy the centromere in the G2 phase of the cell cycle. At the same time, other components such as the Nuclear Division Cell 80 NDC80 complex and the SAC are included in prophase and prometaphase, thus forming a complete and functional kinetochore.

The composition and formation of the CCAN

CCAN consists of Centromere proteins A (CENP-A), CENP-C, CENP H/I/K complex, CENP-L, CENP-M, CENP-N, complex CENP O/P/Q/R/U, and CENP-T/W/S/X complex. CCAN forms a base to which other kinetochore proteins are attached (McClelland et al. 2007; Cheeseman et al. 2008). It is known how CCAN is formed and what the function of its components is. CENP-A and CENP-T attach directly to the centromere DNA. CENP-A is a histone protein. CENP-T creates a CENP-TWSX complex that has domains similar to histone binding domains. CENP-A binds CENP-C and CENP-N, and with their help, other proteins of the CCAN are mutually connected and cooperatively attach to the centromere chromatin. CENP-C, CENP-T/W, and CENP-H/I/K complex attach the KMN complex to the

kinetochore, thus attaching the kinetochore to the spindle apparatus microtubules (Liu et al. 2003, see Rago et al. 2015).

The architecture of CCAN forms a mechanical structure which protects the centromere from overstretching during the pulling or pushing of the kinetochore by microtubules. Inhibition of expression of the CENPT, CENPC, and CENPH /I cause centromere overstretching in mitosis (Suzuki et al. 2014). The stretching of the kinetochore influences the signaling and regulation of a proper attachment of the chromosomes through the aurora B kinase and control of the progress of the cell cycle (Lampson and Cheesman 2011).

The quantity, mobility, and attachment of CCAN proteins changes during the cell cycle (Hellwig et al. 2008, Hemmerich et al. 2009). In metaphase, the region of the CCAN shrinks by about 10 nm (Suzuki 2014). A lack of CCAN proteins disturbs the formation of a functional kinetochore, attachment to the spindle apparatus, and the chromosome alignment at the equatorial plate. Therefore, a decrease in the quantity of CENP-H causes stabilization of kinetochore microtubules, it decelerates oscillations and postpones the onset of anaphase. A lack of CENP-O weakens the kinetochore-microtubule fibers and increases the frequency of monopolar spindles. CENP-H/I/K and CENP-O/P/Q/R/U complexes function as antagonists. A lack of CENP-L and CENP-O causes irregularities in the polymerization of microtubules that disturb the creation of pushing forces. CCAN is not only a physical basis for attachment of other kinetochore proteins to the centromere, but it also participates in the fine regulation of the positioning of chromosomes at the equatorial plate. (McClelland et al. 2009, also see in Westhorpe and Straight 2013).

The structure of the kinetochore-microtubule attachment

The kinetochores attach to the kinetochore fiber microtubules through the Knl1-Mis12-Ndc80 (KMN) super complex. The KMN super complex consists of the Kinetochore null 1 (Knl1) protein, the 4-subunit Mis-segregation 12 (Mis12) complex, and the Nuclear division cycle 80 (Ndc80) heterotetramer. In mitotic prophase, the KMN complex attaches to the CCAN through CENP-C and CENP-T. CENP-C attaches to the Ndc80 complex through the Knl1 and Mis 12 complexes. CENP-T first attaches to the Ndc 80 heterotetramer, and then the Knl1 and Mis 12 complexes attach. Various regulatory proteins control the attachment of the centromere to the KMN network through CENP-C and CENP-T. Aurora B kinase enhances the attachment of CENP-C to the KMN network, while the Cyclin-dependent kinase 1 (CDK1) enhances the attachment of CENP-T to the KMN network (see Rago et al. 2015.).

The kinetochores attach to the microtubules through the elongated Ndc 80 (Nuclear division cycle 80 heterotetramer). On its kinetochore side, two proteins of the NDC 80 heterotetramer Ndc 80 (in humans also called Highly expressed in cancer protein 1 (Hec1)) and Nuclear filamentous 2 (Nuf2) attach the Mis 12 protein to the kinetochore. On the opposite edge of the NDC 80 heterotetramer, proteins Spindle Pole Component 24 (Spc24) and Spc25 attach the microtubules (see Foley et Kapoor 2013). The inhibition of the KMN super complex prevents attachment to the spindle apparatus (see Santaguida and Musaccio 2009).

Kinetochores attach to the dynamic plus end of microtubules. Microtubules are attached to kinetochores while they grow and polymerize and while they are shortening and depolymerize. The ability of the kinetochore to attach to depolymerizing microtubules ensures the oscillations of metaphase chromosomes at the equatorial plate and the movement toward opposite poles in the anaphase (Koshland et al. 1988, Coue et al. 1991).

Kinetochore regulation of the cell cycle

Two main control mechanisms ensure the correct segregation of chromosomes. One is the destabilization of improper microtubule attachment by the Aurora B kinase, and the other is the postponement of division by the Spindle Assembly Checkpoint (SAC) until all kinetochores are properly attached and positioned at the equatorial plate. The proteins of both mechanisms are active on unattached or improperly attached kinetochores (Lampson and Cheesman 2011).

Kinetochore regulation of the spindle apparatus attachment

Prometaphase kinetochores attach to microtubules in different ways: by monotelic, syntelic, merotelic, and bivalent attachments. The monotelic attachment is an attachment of only one sister-kinetochore to the spindle apparatus. The syntelic attachment is the attachment of both sister-kinetochores to the same spindle apparatus pole. The merotelic attachment is the attachment of the same kinetochore to both spindle poles. Only correct attachments where sister-kinetochores are attached to opposite spindle poles enable correct segregation of chromosomes. Initial random kinetochore-microtubule attachments are corrected by detaching of improperly attached microtubules until all chromosomes are bivalently attached, and each sister-kinetochore turned towards the opposite spindle pole. Attachments of the kinetochore to the microtubules need to be dynamic enough to be corrected if they are improper and stabilized if they are bivalent and contribute to the proper orientation of the chromosomes. For correct chromosome segregation, it is essential to selectively destabilize improper attachments (Rieder et al. 1995.).

The Aurora B kinase destabilizes improper attachments. It is localized and active on unattached and improperly attached chromosomes. Aurora B kinase phosphorylates the NDC 80 heterotetramer on improperly attached kinetochores reducing its affinity for microtubules. It prevents the abatement of the Spindle Assembly Checkpoint (SAC) before the proper attachment of chromosomes (Lampson and Cheesman 2011). With early inactivation of the Aurora B kinase, the merotelic and syntelic attachments of microtubules to the kinetochores are stabilized (Ditchfield et al. 2003, Hauf et al, 2003).

The Aurora B kinase is localized in the inner centromere and its substrates toward the outer kinetochore are centripetally phosphorylated in gradient. The phosphorylation of its substrate Ndc 80 heterotetramer is reduced on stretched kinetochores. Excess stretching of centromeres and kinetochores, caused by a decreased CENP-C, CENP-T, and CENP-H concentration, reduces the phosphorylation of the substrates of Aurora B kinase Knl1 and Ndc80/ Hec 1 (Suzuki et al. 2014). According to the spatial distance model, the phosphorylation gradient of the Aurora B kinase

substrate is formed because its peripheral substrates are less accessible. The phosphorylation of Aurora B kinase peripheral substrates is, according to the spatial distance model, additionally reduced by the kinetochores being stretched by the pulling of microtubules. Niklas observation 1967 that kinetochore pulling by a micromanipulation glass needle in live cells stabilizes the attachment to microtubules also supports the spatial distance model, but it is still not known whether pulling stabilizes microtubule attachment directly, or by intermediation of the regulatory proteins. The spatial distance model explains the correction of monotelic and sintelic attachments because they stretch the kinetochore weaker than proper and merotelic attachments (Ditchfield et al, 2003, Liu et al. 2009), but it is still not clear how the Aurora B kinase inside of the centromere connects with distant substrates on kinetochore periphery (Lampson and Cheesman 2011).

The pulling of the kinetochore might be necessary for correction of improper microtubule attachments in prometaphase, for stabilization of kinetochore-microtubule fibers, and for removing the components of SAC from kinetochores (Famulski and Chan 2011, Maresca and Salmon 2010, Kasuboski et al. 2011, Lampson and Cheeseman 2011, Bakhoum et al. 2009, Silkworth and Cimini 2012). A decrease in the quantity of CENP-C and CENP-H through the iRNA increases the extensibility of the CCAN, reduces the phosphorylation of the Ndc complex through the Aurora B kinase, and increases removing of the Mad 1 component of SAC from the kinetochore. The microtubules are attached more stably to more flexible kinetochores with a decreased quantity of CENP-C and CENP-H in regards to native kinetochores (Suzuki 2014). Therefore, the flexibility of the kinetochore chromatin regulated by CCAN proteins might be necessary for the regulation of kinetochore attachment to microtubules through the Aurora B kinase and the SAC mechanism.

Kinetochore regulation of cell cycle progression

The progress of the cell cycle depends on the Aurora B kinase and the SAC biochemical signal network. SAC postpones the anaphase until all kinetochores are properly attached and positioned at the equatorial plate. It detects the attachment of kinetochores to the microtubules and the tension of the kinetochore. It is active on unattached and improperly attached kinetochores in the prometaphase and metaphase (see in Musacchio and Salmon 2009). Just one unattached kinetochore activates SAC and postpones the division by several hours (see Foley et Kapoor 2013). The SAC consists of Mitotic Arrest Deficient 1 (Mad1), Mad2, Mad3, and Budding Uninhibited by Benomyl3 (Bub3), as well as kinases Monopolar Spindle (Msp1) and Bub1. The deletion of SAC proteins causes the onset of anaphase before bivalent attachment and alignment of all chromosomes, as well as aneuploidy. SAC attaches to the kinetochore via the KMN network (see in Foley et Kapoor 2013).

After proper attachment and alignment of the chromosomes, the activity of the SAC must diminish, and its elements must be removed from the kinetochore. Two mechanisms participate in the decrease of SAC activity: one depends on the attachment, and the other depends on the pulling of the kinetochores by microtubules. Kinetochores can distinguish and separately signal the absence of attachment or just the absence of pulling. In this way, kinetochores finely sense proper attachment and positioning of chromosomes in the division plane. When microtubules attach to a kinetochore, Mad1, Mad2, Bubr1, and CDC20 are removed and relocated from the kinetochore towards the

centrosome. The SAC is more sensitive to the kinetochore unattachment than to the absence of forces exerted by microtubules. Unattached kinetochore postpones the anaphase by several hours, and ultimately prevents the breakdown of anaphase inhibitor cyclin B. The inhibition of kinetochore pulling decelerates the breakdown of cyclin B and postpones the anaphase by only approximately twenty minutes (Uschida et al. 2009). Attached but unpulled kinetochores have more Bubr1 than attached pulled microtubules. Attached unpulled microtubules have no Mad2, the primary indicator of the detachment of microtubules from the kinetochore.

Kinetochore stretching in the regulation of the progress of mitosis

Fluorescence microscopy enables the imaging of kinetochore stretching and shrinking during microtubule pulling and pushing in mitosis of live cells. The pulling of the kinetochore by microtubules causes slight distancing between the centers of localization of kinetochore proteins and inactivates the SAC (Maresca and Salmon 2009, Uchida et al. 2009, Suzuki 2014). Stretching of kinetochores by pulling with microtubules might be necessary for correcting improper microtubule attachments in prometaphase (Silkworth and Cimini 2012). The stretching of the kinetochore does not depend solely on the stretching of the inner centromere chromatin; kinetochore stretches and shrinks differently from the inner centromere (Uchida et al. 2009). The stretching of kinetochore between the kinetochore chromatin protein CENP-C and more peripheral SAC protein CdC20 is not exclusively passive; there is an active mechanism of kinetochore shrinking during prometaphase oscillations at the equatorial plate. When the kinetochore changes its course at the equatorial plate and starts moving towards the pole, it simultaneously starts to shrink actively. After shrinking, the kinetochores passively stretch (Dumont et al. 2012).

The pulling of the inner kinetochore assembled with CENP-A was investigated by immunoelectron microscopy of chicken DT40 cells. An area of maximally pulled CENP-A is wider than the same area in the absence of pulling by microtubules. The pulling by microtubules on electron microscope images is achieved by inhibition of the anaphase onset with the molecule Mg 132. Depolymerization of microtubules with nocodazole achieves the state without pulling (Suzuki et al. 2011). However, nocodazole itself changes the size and the shape of the kinetochores (Hoffman et al. 2001).

Optical-microscope and electron-microscope images of different parts of the kinetochore and kinetochore chromatin point to their complex mechanics during mitosis. Unfortunately, they are acquired by imaging of different kinetochore proteins, difficult to interpret into a joint image. (Brinkley and Stublefield 1966, Jokalainen 1967, Roos 1973, McEwen et al. 1998, Saitoh et al. 1992, Wan et al. 2009, Dong et al. 2007, Marshall et al. 2008, Ribeiro et al. 2010, Suzuki 2014) Furthermore, the imaged behavior of the kinetochore during different sub-stages of mitosis also might differ, as it seems from the obtained microscopy data. Over-expression of fluorescently labeled CENP-A causes its incorporation into the kinetochore chromatin in four time-greater quantities. Over-expressed CENP-A occupies a broader area of centromere chromatin than the native CENP-A. The center of localization of fluorescently labeled CENP-A with increased gene expression is around 20 nm towards the centromere interior in comparison to the kinetochore chromatin assembled with natively expressed quantities of CENP-A (Suzuki et al. 2014.). Chromatin assembled with over-expressed levels of CENP-A is more susceptible to stretching during the stretching of the inner centromere than the same part of the kinetochore chromatin assembled with native quantities of CENP-A (Wan et al.

2009). Unfortunately, gene technology that could successfully substitute the native proteins with their fluorescent versions in the human cells is not yet available. In chicken DT40 cells, it is possible to substitute the native kinetochore proteins with similar quantities of fluorescent kinetochore proteins by knock-in gene technique, but the chicken and the human kinetochores differ in the number of attached microtubules. Chicken kinetochores in DT40 cells attach to only a few microtubules, while human kinetochores in HeLa cells attach around 20 microtubules. The difference in the number of attached microtubules might significantly influence the forces and the stretching within the kinetochore (see Gregan et al. 2011). A genetic fluorescent tag itself might change the incorporation of CCAN proteins into the kinetochore.

The structure of the kinetochore

On electron micrographs of the kinetochores of rats and rat kangaroos, two similar layers of high electron density separated by a layer of low density are visible (Jokalainen 1967, Roos 1973). Microtubules attach to the outer layer of the rat kangaroo kinetochore, and in their absence along with the outer layer of the kinetochore, a layer of fine threads called fibrillar corona appears (Brinkley and Stublefield 1966, Roos 1973). The recognizable three-layer kinetochores in rat kangaroo cells appear in prometaphase. In prometaphase, they have different shapes, depending on the attachment to the spindle apparatus microtubules. The prometaphase kinetochores oriented on the equatorial plate are stretched and unstructured, while the monotelic kinetochores shadowed for microtubule attachment on one side have one layer. Only unshadowed prometaphase and metaphase kinetochores have three layers (Roos 1973). On the electron microscopic images of the kinetochore obtained by the high-pressure freezing and freeze substitution technique, the kinetochores consist of a layer 50-75 nm thick, made of threads 10-20 nm thick. On the outer side of the chromosome, it is surrounded by a layer 150 nm thick, made of threads 9 nm thick (McEwen et al. 1998).

On modern high voltage electron microscopic tomography images, the kinetochore consists of a network of sticks 10-20 nm thick. Upon the attachment of microtubules, the network becomes irregular. That network is transversally 35-40 nm thick and in places has darker and lighter parts distributed in three layers (Dong et al. 2007). Electron microscopic micrographs obtained by different imaging and preparation techniques since the 60s until today significantly differ. Their common characteristic is the thread structure, while the three-layer structure is hardly recognizable on the newer electron micrographs with high resolving power, obtained by imaging samples prepared with high-pressure freezing and freeze substitution technique (Dong et al. 2007). First electron micrographs of chromatin also significantly differ from more recent cryo-electron tomography investigation. The first electron microscopy of unfolded chromatin shows parts of chromatin thick around 30 nm. Based on those images together with x-ray crystallography investigation, a model of 30 nm solenoidal super-coiled chromatin was built (Finch and Klug 1976). Structures that would correspond to the 30 nm solenoidal fiber were not found on more recent cryo-electron tomography micrographs of mitotic chromosomes (Eltsov et al. 2008).

Immunoelectron microscopy localized the CENP-C and the CENP-A in the inner kinetochore layer (Saitoh et al. 1992). The CENP-A occupies the periphery of the centromere and the inner kinetochore layer. It is assembled along 2/3 or 236 nm of the centromere constriction in the area that is transversally thick 96 nm, or 1/3 of the thickness of the chromosome. In the direction between sister kinetochores area with CENP-A is 151 nm thick, and it occupies 1/3 of centromere constriction in this direction (Marshall et al. 2008). On immunoelectron micrographs, the CENP-A has two lines separated from each other around 32 nm (**Figure 1**). Unfortunately, the immunoelectron microscopy technique, as well as other electron microscopy techniques, could not show the structure formed by kinetochore chromatin proteins due to sparse labeling of CENP-A with antibodies attached to metal balls used in immunoelectron microscopy.

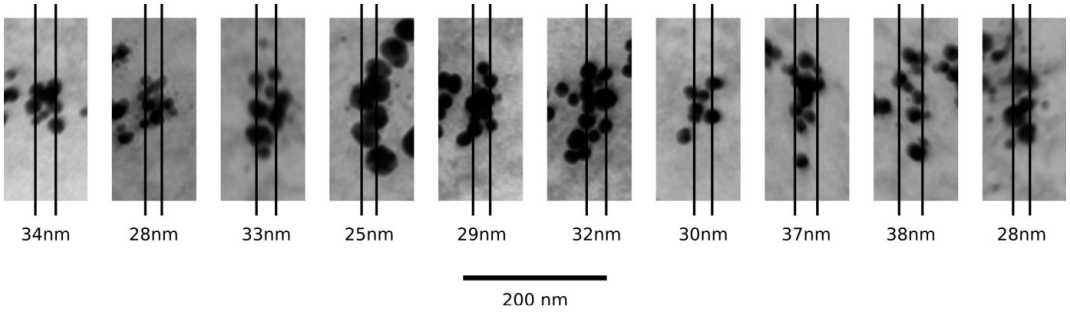

Figure 1. The immunoelectron tomography micrograph of the kinetochore chromatin, occupied with CENP-A. CENP-A was recognized with immunoglobulin primary antibodies and secondary antibodies labeled with metal balls, visible as black dots. The measured distance between the centers of lines of golden balls is between 25 and 37 nm. The image is taken from Marshall et al. 2008 with the permission of the author and the publisher.

Distances between centers of emission of individual fluorescently labeled kinetochore proteins have been determined with the so-called delta method (Varma et al. 2013, Wan et al. 2009, Suzuki et al. 2014). CENP-A and CENP-C are according to that measurement the closest to the interior of the centromere. CCAN proteins CENP-H, CENP-M, CENP-L, CENP-N, CENP-K, and CENP-C, are near CENP-T and CENP-I, and they are colocalized with the peripheral edge of CENP-A. According to the measured distances between the centers of emission of CENP-A and the other CCAN proteins, only a smaller portion of CENP-A can bind other CCAN proteins (Suzuki 2014). CENP-A, CENP-C, and CENP-H are colocalized in intermittent regions on the unfolded kinetochore chromatin. Those regions alternate with regions of CENP-T (Blower et al. 2002, Ribeiro et al. 2010).

The relative distances between kinetochore proteins are measured with the delta method (Wan et al. 2009) and FRET (Hellwig et al. 2009), but the spatial arrangement of kinetochore proteins and the organization of the kinetochore chromatin are still not known due to the limited resolving power of the optical microscope. In the past ten years, optical microscopy has developed tremendously, and many techniques of optical microscopy with high resolving power have been discovered. They might be used for resolving the spatial arrangement of kinetochore proteins and kinetochore chromatin.

Optical microscopy techniques with high resolving power

Optical microscope resolving power depends on the light wavelength, on the incoming angle of light from the sample to the objective, and the refractive index of the medium between the sample and the objective. The maximal resolving power determines the smallest periodicity in the sample, which can be distinguished by a microscope i.e. the Abbe's limit:

$$\Lambda = \frac{\lambda}{2n\sin(\alpha)} = \frac{\lambda}{2NA}$$

Where Λ is the smallest periodicity in the structure that can be resolved with the light microscope, λ is the wavelength of the light, n is the refractive index of the medium, α is the half opening angle of the objective, and NA is the numerical aperture of the objective. Samples closer than the resolution limit can be seen if they are brighter than the background, but they will not be visible separately.

An image obtained by an optical microscope is a convolution of the distribution of fluorophores in the sample and the point spread function (PSF) of the microscope. The optics of the microscope blurs the image, so the point source of light which goes through it is seen as a blurred cloud, i.e. PSF. The point sources of light closer than the resolution limit appear connected like one distorted cloud. In practical cases, besides the wavelength of light, objective opening, and refractive index between the observed sample and the objective, the ability to resolve biological structures also depends on the contrast and density of labeling within the observed structure. The light which comes into the microscope outside of focus reduces the contrast. Selective illumination of the focal plane can, therefore, improve the contrast and bring the resolution closer to the theoretical limit.

For high-resolution microscopy structures of interest have to be carefully and specifically labeled with reporter molecules. According to the Shannon sampling theorem (Shannon 1949) and the Nyquist criterion (Nyquist 1928), the density of labeling molecules in the sample must be at least twice as high as the desired resolving power. For resolving power of thirty nm, structures of interest have to be labeled at least every fifteen nm. This labeling density is not easy to achieve in fluorescence microscopy and immunoelectron microscopy because here, primary and secondary immunoglobulin antibodies, which can be together bigger than fifteen nm, are used for the labeling of specific proteins. Together with a gold bead, used as a reporter molecule in immunoelectron microscopy, the size of the labeling construct can be bigger than twenty nm.

The maximal resolving power of the light microscope, determined by the Abbes limit and the contrast in the sample, can be increased by computer processing of the acquired micrographs, selective sample illumination, and manipulation of photochemical properties of the labeling fluorophores. Deconvolution microscopy slightly increases the resolution beyond the theoretical Abbe's limit by calculating the most probable arrangement of fluorophores, which produced the obtained image. The High-Resolution Structured Illumination Microscopy (HRSIM) selectively illuminates the sample with stripes to transfer information of higher periodicity than Abbe's into the objective by the Moiré effect. After that, the images with resolution twice as Abbe's limit are reconstructed from striped images (Heintzmann and Cremer 1999, Gustafsson 2000). Stimulation

Emission Depletion microscopy (STED) increases the resolution by reducing the area of fluorescence emission. In STED, the size of the fluorescence emission area is reduced by stimulated spontaneous de-mission of fluorescence with a ring of stimulating light around the excitation beam (Hell and Wichmann 1994, see in Schermelleh et al. 2010).

Total Internal reflection microscopy (TIRF) enhances the contrast and depth resolution by exciting only fluorophores 100 nm near the coverslip with the so-called evanescent wave. The evanescent wave is formed by the reflection of excitation beams from the coverslip. The excitation beam is reflected when directed toward the sample under a certain angle. The evanescent wave in the sample quickly loses strength, and 100 nm from the coverslip is not strong enough for fluorophore excitation. If the angle under which the excitation beam falls on the sample decreases below the critical angle, it will not reflect from the coverslip, like in TIRF, but it will penetrate the sample under a highly inclined angle and illuminate the inclined plane within the sample. This way, only the inclined plane around the sample focus is illuminated, and the contrast is enhanced, and such illumination is called Highly Inclined Light-sheet Optical microscopy (HILO). TIRF enhances the contrast near the coverslip and is suitable for imaging cellular structures of the outer surface of the cell, while HILO enhances the contrast deep in the sample and is suitable for imaging the structures within the cell, such as the nucleus (Tokunaga et al. 2008).

Apart from the progress of mathematical processing of micrographs and the enhancement of contrast by manipulating the illuminated area, the number of newly synthesized fluorescent molecules for labeling has increased. The research of their physical and photochemical properties enables the manipulation of their emission (Heilemann et al. 2005). This enables precise localization of individual fluorescent molecules in the fluorescently labeled samples and enhancement of resolution in high-resolution localization light microscopy.

High-resolution localization light microscopy

High-resolution light microscopy is a fluorescent microscopy method where specifically fluorescently labeled sample is imaged in a standard fluorescent microscope. An increase in the resolution is achieved by the localization of individual fluorescent molecules by computer processing of acquired images. Localization of individual molecules is enabled by the manipulation of their fluorescence by different light and chemical conditions during imaging. It enables spatial and temporal segregation of fluorescence of close molecules. When only one molecule of fluorophore shines in an area as big as the diameter of a fluorescent cloud of one fluorescent molecule or PSF of the microscope, it can be precisely statistically localized within its fluorescent cloud (Betzig et al. 2006, Hess et al. 2006, Rust et al. 2006). Fluorescent molecules are localized at the top of the Gaussian curve approximated on the histogram of photons collected by camera pixels (Thompson et al. 2002). Sequential imaging and precise localization of all molecules in the sample one by one with the pointillist method reconstructs a high-resolution image where it is possible to distinguish tiny structures, otherwise blurred in the optical microscope. The precision of localization scales with the inverse square root of the number of detected photons (see Schermelleh et al. 2010)

In biological samples, localization precision reaches up to thirty nm, but localization precision has no physical limit, and it can be enhanced with brighter fluorophores and better detectors. Resolving power of thirty nm, achieved with *d*STORM, is the highest resolving power achieved by the light microscope. It could be used to resolve the structure of the human kinetochore chromatin in the scale between twenty and two hundred nm to distinguish the structures inside of it. During the writing of this thesis, kinetochore chromatin was imaged with *d*STORM and other high-resolution light microscopy methods. Those *d*STORM images of Immunofluorescently labeled CENP-A revealed rosette-like clusters 250-300 nm wide in the G1 phase of the cell cycle (Andronov et al. 2019).

There are many techniques of localization microscopy called Photo Activation Light Microscopy (PALM), Stochastic Reconstruction Microscopy (STORM), direct Stochastic Reconstruction Microscopy (*d*STORM) (Heilemann et al. 2008), GSDIM (Ground-State Depletion and Individual Molecule return (Fölling et al. 2008), etc. They differ by the way how they achieve spatial and temporal segregation of fluorescence of individual molecules and by the used fluorophores. Photo-Activation Light Microscopy (PALM) achieves spatial and temporal separation of fluorescence molecules by photo-activating genetic tags such as DronPA, Padron, Eos, and others (Hess et al. 2006).

Spatially and-temporally segregated fluorescence in STORM is achieved with fluorophores constituted of a molecule of activation fluorophore and a molecule of reporter fluorophore. Reporter fluorophore fluoresces only after activation by light of a different wavelength than the excitation light (Rust et al. 2006). In STORM (Rust et al. 2006), *direct* STORM (*d*STORM) (Heilemann et al. 2008), and GSDIM (Foelling et al. 2008), small organic fluorophores are used for fluorescent labeling. Labeling with organic fluorophores is better for investigation of the chromatin structure than labeling kinetochore proteins with fluorescent tags by genetic fusions. Over-expression of genetically fused fluorescently tagged kinetochore proteins in human cells alters their function and the way how they incorporate in the kinetochore (Suzuki 2014). Small organic fluorophores are much brighter than genetically fused fluorescent tags, and they can be localized more precisely. In this way, a better resolution can be achieved if the samples are labeled densely enough and if the illumination of individual fluorophore molecules is well temporally and spatially segregated.

*D*STORM and GSDIM use small, commercially available organic fluorophores. Their fluorescence is temporally and spatially segregated by turning most fluorophores in the sample into dark states by chemical conditions and by the power of excitation laser. That way, a small number of random distant molecules are stochastically activated and simultaneously fluoresces. The dark states are triplets and radicals. They are created by the excitation of fluorophores with very bright light under reducing conditions (**Figure 2**). They are inherent to all fluorophores due to their non-linear response to strong excitation. The research of non-linear behavior of numerous fluorophores enabled the discovery of the molecular mechanism of the creation of dark states and proper manipulation of fluorescence with light strength and chemical surroundings (Vogelsang et al. 2008, Heilemann et al. 2009). In this thesis, I studied the kinetochore chromatin using *d*STORM because among the techniques of optical microscopy with high resolving power, *d*STORM achieves the highest resolving power, and it can be used with easily available fluorophores and optical parts that were available to me.

More than five years ago, in the scientific literature, a resolution of *d*STORM of about 10 nm was demonstrated (Huang et al. 2012), as well as two-color and three-dimensional imaging in high-resolution (Löschberger et al. 2012, Huang et al. 2008). *d*STORM was used to discover the structure of the microtubule-organizing centers (MTOCs) in centrosomes (Mennella et al. 2012), periodicity of the cytoskeletal structures of the proteins actin and spectrin in axons (Xu et al. 2013), for imaging of the nanoscale organization of ESCRT machinery, necessary for mediating HIV abscission (Van Engelenburg et al. 2014), for investigation of organization of 4-fold linear Ca^{2+}signalling in sperm flagella (Chung et al. 2014), for imaging of organization of A spindle-like apparatus in bacteria (Ptacin et al. 2010), for the determination of *in vivo* target search kinetics of regulatory non-coding RNA (Fei et al. 2015), to image T-loop formation in telomeres (Doksani et al. 2013), and to image the spatial organiation of CENP-A clusters (Andronov et al. 2019). Nevertheless, all the experiments described in this thesis were finished in 2014, and the writing of this thesis was mostly finished and corrected before the publication of rosette-like clusters of CENP-A by Andronov et al.

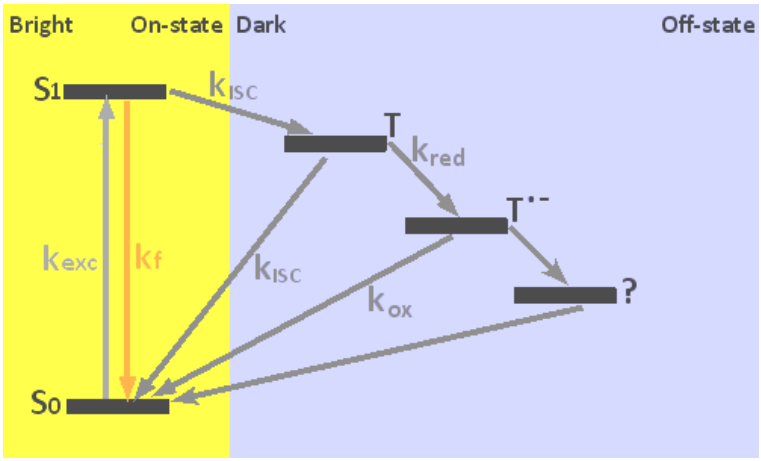

Figure 2. Reactions in the reversible photoswitching of Alexa-fluorine and ATTO dyes. Upon the excitation of the dye molecules (k_{exc}) into the first excited singlet state (S_1), fluorescence can be emitted (k_f), and the molecule goes to the ground state (S_0.) Excited molecule (S_1) can by intersystem crossing (k_{isc}) get triplet electron configuration (T). A molecule in the excited triplet state (T) can be reduced (k_{red}) with thiols (RS red) to become a reduced triplet radical (T^{*-}). Triplet can also go through intersystem crossing (k_{isc}) to the ground state (S_0). A molecule with the electron configuration of the triplet radical (T^{*-}) after oxidation with molecular oxygen (O_2,) (k_{ox}) becomes the electron configuration of the ground state (S_0). Alternatively, triplet radicals can react with other molecules in the embedding medium and become other nonfluorescent species (grey). The figure is adjusted from Heilemann et al. 2009 and taken with the permission of the publisher.

The aim of the research

The kinetochore chromatin on the periphery of the centromere is a physical basis for the formation of the complete functional kinetochore complex. Kinetochore chromatin participates in the creation of centromere tension and forces, necessary for the correction of improper microtubule attachments by the control mechanisms of Aurora B kinase and Spindle Assembly Checkpoint (SAC), and the progress of mitosis. The spatial arrangement of kinetochore proteins and the structure of kinetochore chromatin in the scale between 20 and 200 nm have not been resolved till recently (Andronov et al 2019), during the finishing of the writing of this doctoral thesis. The recent development of the methods of optical microscopy, especially the method of localization microscopy direct Stochastic Optical Reconstruction Microscopy (*d*STORM), increases the resolving power of the optical microscope up to 30 nm or more. It could be used to distinguish the spatial arrangement and the structure of kinetochore chromatin and its changes during the cell cycle.

The aim of this research is:

- To improve and adjust the method of direct Stochastic Optical Reconstruction Microscopy (*d*STORM) for imaging of the kinetochore chromatin with high-resolution
- To discover the structure of the human kinetochore chromatin assembled with CENP-A in the scale between 10 and 200 nm and to examine whether it changes during the cell cycle.
- To examine the influence of the forces of the spindle apparatus microtubules on the structure and dimensions of the kinetochore chromatin assembled with CENP-A
- To examine how the mitotic toxin nocodazole influences the structure and the dimensions of the kinetochore chromatin.

Knowing the structure of the human kinetochore chromatin in different phases of the cell cycle might explain how it withstands the forces of microtubules, detects correct attachment of chromosomes, and regulates the progress of the cell cycle. The imaging of the kinetochore chromatin of cells treated with nocodazole will show how nocodazole influences the structure of kinetochore chromatin. These images might explain a possible connection of the inner structure of the kinetochore chromatin with the regulation of proper attachment of chromosomes.

Along with the research of kinetochore chromatin, perfecting the *d*STORM method for application on chromatin might enable the research of the organization and spatial arrangement of other parts of the chromosome essential for its function, such as the telomere and chromosome regions, which will contribute to the understanding of the maintenance of gene stability and genome integrity.

Material and methods

Material

Cell culture

Table 1. Reagents used in the cell culture

Reagent	Manufacturer
Alconox	Sigma Aldrich (Steinheim)
Bovine serum albumin	Sigma Aldrich (Steinheim)
Catalase from bovine liver	Sigma Aldrich (Steinheim)
Cysteamine, 98%	Carl Roth (Karlsruhe)
D+ Glucose	Merck (Darmstadt)
Dulbecco´s Modified Eagle Medium (DMEM)	PAA (Pasching, Austria)
Ethanol absolute	Cark Roth (Karlsruhe)
Fetal bovine serum heat inactivated	PAA (Pasching, Austria)
Formaldehyde 37 %	Cark Roth (Karlsruhe)
Glucose oxidase from Aspergillus niger, type X-S	Sigma Aldrich (Steinheim)
Glutaraldehyde	Cark Roth (Karlsruhe)
Methanol absolute	Carl Roth (Karlsruhe)
MG132	Merck (Darmstadt), Cayman chemical
NaOH (Natriumhydroxide)	Cark Roth (Karlsruhe)
Nocodazole	Merck (Darmstadt)
PFA (Paraformaldehyde)	Sigma (München)
Prolong gold	Molecular probes (Eugene, USA)
RO3306 Cdk1 Inhibitor IV	Merck (Darmstadt)
Sodium borohydride NaBH4	Sigma Aldrich(Steinheim)
Thymidine ≥99% (HPLC), Fluka,	Sigma Aldrich(Steinheim)
Triton X 100	Serva (Heidelberg)

Table 2. Material for the cell culture

Medium /supplement	producer
DMEM (low Glucose1g/l with L-Glutamine)	PAA (Pasching Austria)
FBS (heat-inactivated)	PAA (Pasching Austria)
Trypsin/EDTA (0,05% /0,02% in D-PBS)	PAA (Pasching Austria)
10X PBS (used as 1X)	Carl Roth (Karlsruhe)
Cells	
HEp-2 (ATCC CCL-23)	CCL-23, American Tissue Culture Collection (ATCC)

Devices:

- incubator Hera Cell 150
- HeraeusWater purification system MiliQ Reference A+ (M Millipore)

Fluorescent sample labeling

Table 3. Buffers used for fluorescent labeling of the samples

Buffer	content
Blinking buffer	PBS, 10% glucose, a small crystal of glucose oxidase, a small crystal of catalase, 50 mM cysteamine
Blocking buffer	1%BSA in PBS
Formaldehyde fixation buffer	4% formaldehyde in PBS
Glutaraldehyde fixation buffer	3,5 % formaldehyde, 0,2% glutaraldehyde in PBS
Permeabilisation buffer	0,25 % Triton X-100 in PBS
Quenching buffer	0,1 % Na BH4 in PBS

Oligonucleotides for fluorescent labeling of DNA origami rectangles:

- CAAGCCCAATAGGAACCCATGTACCGTAACAC
- TATCACCGTACTCAGGAGGTTTAGCGGGGTTT
- ACCCAAATCAAGTTTTTTGGGGTCAAAGAACG

Oligonucleotides are at 5’ end attached to the Alexa Fluor 488 dye via the N-hydroxysuccinimide - ester.

Table 4. Primary antibodies used for fluorescent labeling of the samples All listed primary antibodies recognize human antigens.

Name	Source and the clonality	Manufacturer
Anti –α-Tubilin antibody clone DM1A	Mouse monoclonal	Sigma Aldrich (Steinheim)
Anti CENP-A	Mouse monoclonal	Kinja Yoda, Japan
Anti CENP-A clone 3-19	Mouse monoclonal	MBL (Woburn, USA)
Anti CENP-B	Rabbit polyclonal	Kinja Yoda, Japan
Anti CENP-C	Guinea pig polyclonal	Kinja Yoda, Japan
ACA serum	Human polyclonal	Uniklinik Jena
CENP-F antibody NB 500-101C	Rabbit polyclonal	Novus Biologicals (Littleton, CO, USA)
CENP-H Antibody (FL-247)	Rabbit polyclonal	Santa Cruz Biotechnology
Anti CENP-I SAB 2100405	Rabbit polyclonal	Sigma Aldrich(Steinheim)
CENP-K Antibody (40.3)	Mouse monoclonal	Santa Cruz Biotechnology
CENP-M AntibodyN17	Rabbit polyclonal	Santa Cruz Biotechnology
Anti CENP- O, SAB 3500108	Rabbit polyclonal	Sigma Aldrich(Steinheim)
CENP-P antibody	Guinea pig polyclonal	Tatsuo Fukagawa
Anti CENP-Q	Mouse monoclonal	Kinja Yoda, Japan
Anti CENP-T	Mouse polyclonal	Kevin Sullivan, USA
Anti-CENP-T (ICEN22)	Rat monoclonal	MBL (Woburn, USA)
Phalloidin Alexa 647	An organic molecule, chemical synthesis	Molecular probes (Eugene, USA)

Table 5. Secondary antibodies used for the fluorescent labeling of the samples. All secondary antibodies were produced by Dianova, Hamburg

Reactivity	Description
Goat anti-guinea pig Alexa 488	Anti-human IgG connected with Alexa Fluor 488
Goat anti-human IgG Cy 5	IgG connected with cy5 (Indodicarbocyanin)
Goat anti-mouse Cy2	Goat anti-mouse connected with Cy2 (Carbocyanin)
Goat anti-mouse Cy3	IgG connected with Cy3 (Indocarbocyanin)
Goat anti-mouse Alexa 488	Anti-mouse IgG connected with Alexa Fluor 488
Goat anti-mouse Alexa 647	Anti-mouse IgG connected with Alexa Fluor 647
Goat anti-rabbit Alexa Cy2	Anti-rabbit IgG connected with Cy2 (Carbocyanin)
Goat anti-rabbit Cy3	Anti-rabbit IgG connected with Cy3 (Indocarbocyanin)
Goat anti-rat Alexa 488	Anti-rat IgG connected with Alexa Fluor 488

Materials for assembly of the microscope

Table 6. Parts of the first version of the *d*STORM microscope

Component of the optical setup on the optical table	Supplier
Mechanical parts and carriers of the optical components	
"KM 1" kinematic mirror mount,	Thorlabs, (Newton, USA)
Iris diaphragm ID 12 Thorlabs (Newton, USA)	Thorlabs, (Newton, USA)
M1-Threaded 30 mm Cage Plate	Thorlabs, (Newton, USA)
ER cage assembly rods	Thorlabs, (Newton, USA)
Optical components	
Dielectric mirror- 400-750 nm, Thorlabs (Newton, USA)	Thorlabs, (Newton, USA)
2.5 cm mounted N-BK7 plano-convex lens f=250 mm LA1461-A-ML	Thorlabs (Newton, USA)
2.5 cm mounted N-BK7 plano-convex lens f=50 mm LA1131-A-ML	Thorlabs (Newton, USA)
Source of light	
473 nm laser, 150 mW B100MA5A3-00721354	An unknown producer from China.
Parts of the microscope	
Tube lens: Lens AC254-200-A-MC400-700 nm brass coating f=200 mm	Thorlabs (Newton, USA)
Objective: Plan Apochromat 63X oil immersion, NA 1,4e	Carl Zeiss Jena
Filters and mirrors for fluorescent microscopy	
Fluorescence excitation filter set 9: Excitation filter BP 450-490hb -- Beam splitter FT 590 Emission filter LP515	Carl Zeiss Jena
Fluorescence excitation filter set 15	Carl Zeiss Jena
CCD camera Imager Intense	La Vision , Germany

Table 7. Parts on the optical table used in the assembly of the second version of the *d*STORM microscope

Component of the optical setup on the optical table	Supplier
Mechanical parts and carriers of the optical components	
KM 1" kinematic mirror mount,	Thorlabs, (Newton, USA)
Rew B breadboard 45 cm × 60 cm × 12,6 cm	Thorlabs, (Newton, USA)
Iris diaphragm ID 12 Thorlabs (Newton, USA)	Thorlabs, (Newton, USA)
M1-Threaded 30 mm Cage Plate	Thorlabs, (Newton, USA)
ER cage assembly rods	Thorlabs, (Newton, USA)
Optical components	
Dielectric mirror- 400-750 nm, Thorlabs (Newton, USA)	Thorlabs, (Newton, USA)
Acousto-optic filter AA. AOTFnc-400.650TN,	AA optoelectronics (Orsay, France)
Absorptive neutral density filter, optical density 4, NE40A	Thorlabs (Newton, USA)
Absorptive neutral density filter, optical density 2, NE20A	Thorlabs (Newton, USA)
Longpass dichroic mirror 425 cutoff DMLP425	Thorlabs (Newton, USA)
Longpass dichroic mirror 505 DRSP EL97123427	Omega optical
Longpass dichroic mirror 561 DRLP	Unknown producer
Sources of light	
405 nm laser LSR-405-NL2-250	An unknown producer from China
473 nm laser, 150 mW B100MA5A3-00721354	An unknown producer from China
532 nm solid-state laser	An unknown producer from China
660 nm diode laser 500 mW	MQ photonics (Soehrewald)
Parts of the microscope	
Body of the microscope Axiovert 100M	Carl Zeiss Jena
Tube lens from the other Axiovert 100 M microscope f= 164,5 mm	Carl Zeiss Jena
IX2-NPS Stable nosepiece stage Olympus (Tokyo Japan)	Olympus (Tokyo Japan)
Objective: Plan Apochromat 63x oil immersion, NA 1,4e	Carl Zeiss Jena
Fluorescence excitation filter set 9: Excitation filter BP 450-490 Beam splitter FT 590 Emission filter LP515	Carl Zeiss Jena
Fluorescence excitation filter set 15	Carl Zeiss Jena
Camera adapter 60C 1"	Carl Zeiss (Jena)
Camera Andor EMCCD Ixon X3 model DU 897D-CSO#BV	Andor (Belfast UK)

Table 8. Parts of the final version the *d*STORM microscope

Component of the optical setup on the optical table	Supplier
Mechanical parts and carriers of the optical components on the table	
"KM 1" kinematic mirror mount,	Thorlabs, (Newton, USA)
Rew B breadboard 45 cm × 60 cm × 12,6 cm	Thorlabs, (Newton, USA)
SH05 shutter	Thorlabs, (Newton, USA)
SC10 shutter controller, Thorlabs (Newton, USA)	Thorlabs, (Newton, USA)
Iris diaphragm ID 12 Thorlabs (Newton, USA)	Thorlabs, (Newton, USA)
Optical components on the table	
Dielectric mirror- 400-750 nm, Thorlabs (Newton, USA)	Thorlabs, (Newton, USA)
Acousto-optic filter AA. AOTF nc-400.650TN,	AA optoelectronics (Orsay, France)
Acousto-optic driver AA. MDS 8C-B66-2274.158	AA optoelectronics (Orsay, France)
2.5 cm mounted N-BK7 plano-convex lens f=250 mm LA1461-A-ML	Thorlabs (Newton, USA)
2.5 cm mounted N-BK7 plano-convex lens f=50 mm LA1131-A-ML	Thorlabs (Newton, USA)
Lens AC254-150-A-MC400-700 nm brass coating f=150 mm,	Thorlabs (Newton, USA)
Lens AC254-30-A-MC400-700 nm brass coating f=150 mm,	Thorlabs (Newton, USA)
Absorptive neutral density filter, optical density 4, NE40A	Thorlabs (Newton, USA)
Absorptive neutral density filter, optical density 2, NE20A	Thorlabs (Newton, USA)
Longpass dichroic mirror 425 cutoff DMLP425	Thorlabs (Newton, USA)
Longpass dichroic mirror 505 nm cutoff DMLP 505	Thorlabs (Newton, USA)
Longpass dichroic mirror 567 nm cutoff DMLP567	Thorlabs (Newton, USA)
Sources of light	
Argon laser Inova 90 A series	Coherent (Santa Clara, USA)
405 nm laser LSR-405-NL2-250	An unknown producer from China
473 nm laser, 150 mW B100MA5A3-00721354	An unknown producer from China
532 nm solid-state laser	An unknown producer from China
660 nm diode laser 500 mW	MQ photonics (Soehrewald)
Parts of the microscope	
Body of the microscope Axiovert 100M	Carl Zeiss Jena
Tube lens from the other Axiovert 100 M microscope f= 164,5 mm	Carl Zeiss Jena
IX2-NPS Stable nosepiece stage Olympus (Tokyo Japan)	Olympus (Tokyo Japan)

Objective: Plan Apochromat 100 × oil immersion, NA 1,4	Carl Zeiss Jena
Filters and mirrors for fluorescent microscopy	
BrightLine HC 640/40 filter	Semrock (Rochester USA)
589IY25 long pass filter	Comar (Linton UK)
BrightLine FF740-Di01-25x36, Semrock (Rochester USA)	Semrock (Rochester USA)
BrightLine HC, 794/160, Semrock (Rochester USA)	Semrock (Rochester USA)
Fluorescence excitation filter set 9: Excitation filter BP 450-490 Beam splitter FT 590 Emission filter LP515	Carl Zeiss Jena
Fluorescence excitation filter set 15	Carl Zeiss Jena
Camera adapter 60C 1”	Carl Zeiss (Jena)
Camera Andor EMCCD Ixon X3 model DU 897D-CSO#BV	Andor (Belfast UK)

Auxiliary parts:

- Laser power meter (Nova-II, Ophir)
- Sheer plate (Thorlabs)
- Polarising filter (Thorlabs)

Software:

- Micromanager, version 1.4, (https://micro-manager.org/)
- Image J, (http://downloads.imagej.net)
- AOTF controlling software: Multi Digital Synthesizer Software (MDS), AA Optoelectronics (Orsay, France)

Methods

Preparation of biological samples

Cell culture and synchronization

I imaged fluorescently labeled kinetochores, microtubules, and actin filaments in Hep-2 cells. I cultured Hep-2 cells for fluorescence microscopy on high precision coverslips No 1.5 as per protocol suggested by Dempsey (Dempsey et al. 2011). Before growing cells on coverslips, I cleaned them with a 15-minute sonication in the following solutions: 1% Alconox solution, absolute ethanol, 1 M solution of potassium hydroxide, and Mili-Q-water. Between every sonication, I washed the coverslips with Mili-Q-water. I dried the cleaned coverslips with compressed air, stored them in a glass Petri dish, and autoclaved for 10 minutes at 121°C.

For fluorescent microscopy of kinetochores in mitosis, I synchronized Hep 2 cells with thymidine and RO3306 molecules (**Table 9**). Thymidine inhibits DNA synthesis and prevents cells to from entering the S phase of the cell cycle. RO3306 inhibits Cyclin-dependent kinase 1 and prevents the beginning of prophase. To synchronize cells and increase the portion of cells in mitosis, I grew the cells on coverslips in a growing medium composed of DMEM medium supplemented with FBS (hereinafter: growing medium) in an incubator with 9.6% CO_2 at 37°C. When cells covered approximately 20% of the coverslip, I added thymidine in the growing medium to the final concentration of 200 µM. After 18 hours of incubation with thymidine, I washed the coverslips with cells two times with PBS and transferred them into fresh DMEM medium with 10% of FBS. 8 hours after adding the fresh medium, I again added thymidine for 18 hours. After the second incubation with 200 µM thymidine I washed the coverslips with cells in PBS and transferred them into fresh DMEM growing medium for 4 hours. Then I added RO 3306 into the growing medium to the final concentration of 10 mM and incubated the coverslips with cells in that medium for 4 hours. After incubation with RO3306, I washed the medium with PBS and replaced it with the growing medium with 35 µM Mg132. After the described protocol, around 70% of cells were in prometaphase or metaphase.

I investigated with fluorescence microscopy the influence of cytostatic and microtubule depolymerizing nocodazole on kinetochore structure. To study the influence of nocodazole, I incubated cells in step 7 (**Table 9**) in growing medium with 1µg/ml nocodazole.

For fluorescence microscopy of Hep-2 cells in the G1 phase, I fixated cells on coverslips after the end of the second incubation with thymidine, i.e. after the end of step 4 (**Table 9**). For enrichment of Hep-2 cells on the coverslip that are in the S phase, I fixated cells on the coverslip cells 4 h after the second incubation with thymidine, i.e., during step 5. For enrichment of Hep-2 cells on the coverslip that are in the G2 phase, I fixated the cells after 4-hour incubation with RO3306 (step 6, **Table 9**).

Table 9. Sequence of the applied growing media for cell synchronization. To increase the number of mitotic cells in the sample and the portion of cells in other phases of the cell cycle, I synchronized them by changing the growing medium (DMEM with 10% FBS), and the growing medium with addition of thymidine, RO3306, Mg132 or nocodazole.

Step	Medium	Duration
1	DMEM with 10% FBS	approximately 24 hours
2	DMEM with 10% FBS and with 200 µM thymidine	16-18 h
3	DMEM with 10% FBS	8-9 h
4	DMEM with 10% FBS and 200 µM thymidine	16-18h
5	DMEM with 10% FBS	4h
6	DMEM with 10% FBS and 10 mM RO3306	4h
7	DMEM with 10% FBS and 35 µM Mg132 or DMEM with 10% FBS and 1µg/ml nocodazole*	2h

*The medium with nocodazole was added only when the influence of nocodazole on the kinetochore structure had been examined.

Immunofluorescent labeling for *d*STORM

I imaged with *d*STORM kinetochores labeled with primary antibody *Anti-CENP-A, clone 3-19*, MBL antibodies. I stained antibodies with fluorescent dye *Alexa Fluor 647* with *Antibody labeling kit* (Molecular probes) as per the manufacturer's instruction. Before fluorescent labeling of kinetochores in Hep-2 cells, I briefly washed coverslips with cells in PBS buffer heated to 37° (**Table 11**). I washed the coverslips with cells in warm PBS buffer to prevent the cold shock and to prevent the depolymerizing of the kinetochore microtubules. After washing, I fixed the cells by immersion in 4% formaldehyde in PBB for 5 minutes at room temperature and then washed coverslips with cells with PBS 3 times for 10 min. After washing from fixative, I quenched the background fluorescence caused by aldehyde fixation by incubation of the coverslips with HEP-2 cells in a freshly prepared solution of 0.1% $NaBH_4$ in PBS 3 times for 3 minutes.

For fluorescent labeling of cells for *d*STORM I permeabilized the cell membrane of fixated and quenched cells for the passing of labeling antibodies Anty-CENP-A-Alexa Fluor 647, DM1α anty-tubulin antibody and Phalloidin Alexa Fluor 647 by immersing coverslips with Hep-2 cells in 0.25 % solution of Triton-X 100 in PBS (**Table 11**). Then I washed the solution of Triton x-100 by immersing coverslips with cells 3 times in clean PBS buffer. After the permeabilization of the cell membrane with Triton-x 100, I blocked non-specific antibody binding by immersing the coverslips with cells in a blocking buffer (1% w/v BSA in PBS). Then I incubated Hep-2 cells for 1 h with 100 µl of the solution of the labeling molecule Anty-CENP-A Alexa Fluor 647, or DM1α anty-tubulin antibody, or Phalloidin-Alexa Fluor 647, all diluted with blocking buffer by disposing of coverslips with the cells on top of the drop with the solution of antibodies. A list of antibodies with used concentrations is shown in **Table 10**.

Table 10. Antibodies used for the labeling of cells for *d*STORM imaging

Antibody	concentration
Anty-CENP-A Alexa Fluor 647	1/100
DM1α anti-tubulin antibody	1/400
Phalloidin Alexa Fluor 647	1/20

When I fluorescently labeled samples with fluorescently stained primary antibody Anti-CenpA-Alexa-Fluor-647, or phalloidin-Alexa-Fluor-647, after the incubation with fluorescent labeling molecules I washed the coverslips with Hep-2 cells three times for ten minutes with PBS (**Table 11**). After washing the solution of fluorescent labeling molecules, I dried the coverslips with cells by sequential dipping for five seconds in thirty percent ethanol solution, then in the seventy percent, then in ninety percent, and then in the absolute ethanol at minus twenty °C. The dry coverslip with cells I placed on the microscope slide with a small well filled with blinking buffer for *d*STORM and pasted the coverslip with immersed cells to the microscope slide with Picodent Twinsil two-component adhesive (**Table 11**).

For *d*STORM resolution test measurements and testing of the kinetochore specificity of antibodies, I immunofluorescently labeled microtubules with non-fluorescent primary antibody DM1α and kinetochores with corresponding nonfluorescent primary antibodies (**Table 26**). After the incubation of the primary antibody, I washed coverslips with Hep-2 cells with a blocking buffer three times for

ten minutes. Then I incubated the cells with fluorescent secondary antibodies five hundred times diluted in a blocking buffer (**Table 5**). I washed the secondary fluorescent antibodies in PBS three times for ten minutes and then dried by sequential dipping in ethanol solution and prepared the cells for microscopy, as described in the previous paragraph and (**Table 11**).

For labeling the actin filaments with phalloidin-Alexa-Fluor-647, I used the same protocol like immunofluorescence (**Table 11**) but I skipped the blocking step and I diluted the phalloidin-Alexa-Fluor 647 with PBS instead of blocking buffer. I incubated Hep-2 cells with phalloidin-Alexa-Fluor-647 for twenty minutes and then washed them with PBS three times for three minutes. Then I prepared the samples with labeled actin filament fibers for *d*STORM as described in the previous paragraph and Table 11.

For kinetochore fluorescent labelling, I examined kinetochore specificity of sixteen different antibodies (**Table 4** chapter Material). Kinetochores were immunofluorescently labeled with them according to the same protocol for immunofluorescent labeling I used for *d*STORM with a couple of exceptions (step 2 **Table 11**). I examined the ability of the tested antibodies to label the kinetochores in dilutions 1/100, 1/200, 1/400, 1/800.

Preparation of the test samples of the DNA origami

DNA origami rectangles with the dimensions of 50 nm × 70 nm were prepared and imaged on AFM by Andreas Kopielski (**Figure 7**). They were prepared from plasmid DNA and oligonucleotides, which folded plasmid DNA into a rectangle as described in Rothemund 2006. The only exception was that 3 oligonucleotides from the hybridization mixture were fluorescently labeled with a single molecule of Alexa Fluor 488. Their sequence is shown in the chapter Material.

DNA origami rectangles were disposed on an etched glass coverslip by incubating solution with DNA origami rectangles 5 minutes on a coverslip and then washing them with Mili Q water. After washing, they were dried and imaged on the AFM microscope to confirm the preservation of the rectangle shape. After AFM measurement, DNA origami rectangles disposed on the glass coverslip were embedded in a blinking buffer without cysteamine and imaged by *d*STORM. For AFM measurement, DNA origami rectangles were deposited on plastic Mica slides and imaged with AFM microscope as described in Rothemund 2006.

Table 11. Protocol for immunofluorescent labelling of the sample. The table shows the sequence of steps of immunofluorescent sample labeling, the composition of used solutions, and the duration of incubation with each solution. The difference in treatments between cell labeling for STORM and cell labeling for antibody testing is marked in brackets next to the treatment and the solution.

step	treatment	solution	duration
1	washing	PBS	short
2	fixation	Formaldehyde or Glutaraldehyde* or methanol -20°C→3,4,8**	10 minutes
			5 minutes
			20 minutes
3	washing	PBS	3x short
4	quenching	0,1% NaBH4 in PBS	3x 10 min.
5	washing	PBS	3x short
6	Permeabilization (only aldehyde fixation	0,25% Triton x 100 in PBS	3 min
7	washing	PBS	3x 3 min
8	blocking	1% BSA in PBS	1hour
9	Primary antibody incubation	Antibodies diluted with blocking buffer (table 3)	1 hour
10	washing	1% BSA in PBS	3x 10 min
11	Secondary antibody incubation	Antibodies 500 times diluted with blocking buffer	1hour
12	washing	PBS	3x10 min
13	Drying (only *d*STORM)	30% ethanol 70% ethanol 90% ethanol absolute ethanol -20°C	5s each concentration
14	Embedding	Blinking buffer (only *d*STORM) or	no incubation
		Prolong gold (only antibodies testing)	overnight
15	Sealing (only *d*STORM)	Picodent component A+B	1 min

*When methanol was used as a fixative, I skipped the sample permeabilization.
**Glutaraldehyde and Methanol were used as fixatives only in the testing measurement of the kinetochore specificity of the antibodies.

Assembly of the *d*STORM microscope

The first version of the transmission *d*STORM microscope

I assembled the first *d*STORM microscope on the body of the Zeiss Axiovert 200 microscope. For imaging for *d*STORM I used optical components of the detection path inside of this microscope. I assembled optical components on the illumination part of the microscope on the optical table next to the microscope from lenses and mirrors (**Figure 3**, **Table 6**). I arranged optical components of the excitation path of the optical setup to illuminate samples during imaging for *d*STORM with parallel laser light. Excitation of the sample with parallel light should enable uniform illumination during imaging, necessary for control of the blinking of fluorescent molecules.

Before the assembly of the optical parts for illumination, I removed all the optical components from the back opening of the microscope. I pointed the beam of the 478 nm laser (300 mW MQ photonics) to the back opening of the microscope so that it passes through the objective hole. I guided the laser beam into the back opening of the microscope by using two guidance mirrors with fine regulation of inclination angle, the so-called angled mirror, about 10 cm away (M1,**Figure 3**), and position mirror about 30 cm away from the angle-mirror (M2, **Figure 3**,). I placed the guidance mirrors so that the incoming laser beam reflects from the angle of the mirror at right angles before entering the microscope. I chose such an arrangement of mirrors for beam guidance because the movement of an angled mirror significantly shifts the angle of the excitation beam in the field of view in the microscope. At the same time, by moving the angle of illumination in the field of view, the position of the laser beam in the field of view only slightly changes. The opposite occurs when moving the positioning mirror; then, the position of the laser beam in the field of view of the microscope changes significantly, but the angle of the illumination changes only slightly. When a laser beam passed through the microscope objective hole, I adjusted the position and the angle of the beam path with the position and the angle-mirror. I adjusted the beam path so that it goes through three targets. I hung the firs target over the back opening of the microscope. Second target was screwed at the bottom of the objective. The third target was on the ceiling above the microscope.

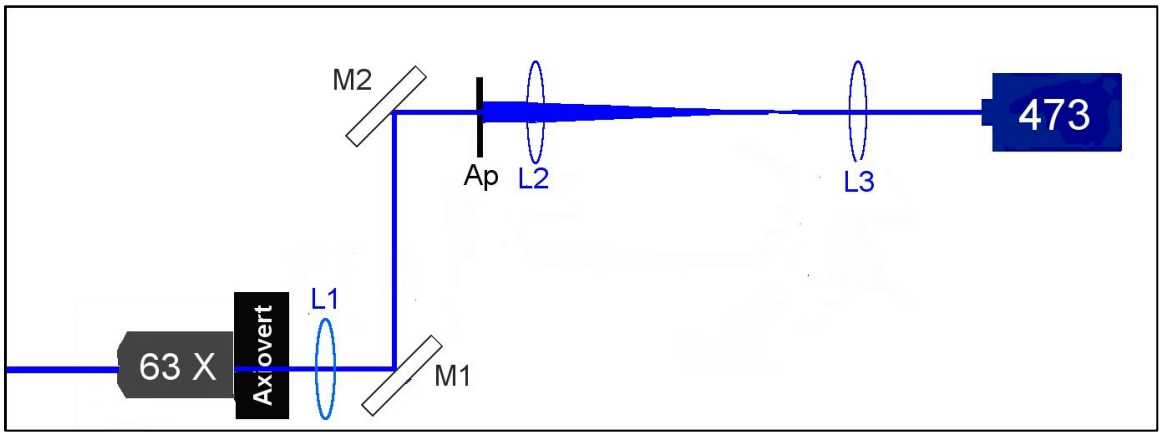

Figure 3. Illumination path of the first version of the *d*STORM microscope. Illumination path of the optical setup is composed of the 180 mW 473 nm laser (473), the telescope, composed of a planoconvex lens of a focal distance f=50 mm (L3), and a planoconvex lens of a focal distance f=250 mm (L2), aperture (Ap), position mirror (M2), angle mirror (M1), tube lens with focal distance f=200 mm (L1), body of the Axiovert 200 M microscope (Axiovert), and a 63x magnification oil immersion objective (63x). The microscope body, together with optical parts inside, is depicted as a black rectangle (Axiovert). Optical components with precise information about their properties and producers are listed in **Table 6**.)

After I passed the excitation beam through the microscope, I removed the target from the objective opening, and I screwed in the objective with magnification 10 ×. Then I corrected the angle and the position of the laser beam with the position mirror and the angle-mirror so that the laser beam after passing through the objective falls on the same marked place on the ceiling. I repeated the correction procedure for the oil objective with magnification 63 ×.

After leading the laser beam through the microscope and the objective, I inserted in the microscope the tube lens for the illumination. On the outside of the back opening of the microscope, I screwed a carrier with rails. I inserted a tube lens with the focal length of 200 mm (L1, **Figure 3**) in the carrier for precise movement and placed it together with the carrier for precise movement on the carrier with rails around the back opening of the microscope.

After inserting the lens on the microscope, I adjusted the position of the lens so that the laser beam passes through its center. Then I adjusted the distance of the tube lens from the microscope by moving the tube lens away from the microscope opening so that the excitation beam which passes through it and the 10 × objective hits the same spot on the ceiling as the beam before inserting the tube lens. The tube lens was in the correct position from the microscope, according to its focal length, when the laser beam passing the microscope was parallel or as small as possible on the marked spot on the ceiling. On the assembled microscope, I attached the CCD camera and slightly adjusted the position of the excitation beam so that it illuminates the center of the fluorescent sample imaged by the camera.

To ensure uniform illumination of the sample, I expanded the excitation beam five times with a telescope. Edges of the expanded laser beam have a smaller intensity than the middle of the beam; therefore, I blocked them with an aperture. I expanded the beam with the telescope composed of two lenses with focal lengths of 250 mm (L2, **Figure 3**) and 50 mm (L3, **Figure 3**) separated by 300mm and placed in the carrier with rails. In this way, the axial position of lenses could be adjusted without modifying their angle. I inserted the telescope in front of the position mirror in the incoming direction of the excitation beam. After inserting the telescope on the path of the excitation beam, I adjusted the angle of lenses to make them vertical i.e., coaxial to the incoming laser beam. I checked if the laser beam is coaxial by tracking the laser reflection from the lens by using the target with the hole in the center. When the laser reflection returns to the same hole as the incoming beam, the lens is coaxial. I checked if the laser beam is coaxial when inserting every new optical part. I checked if the laser beam is parallel after passing through such an assembled telescope with the sheer plate. I adjusted the axial position of lenses, so the laser beam is parallel after passing through the telescope. When building the optical system, I avoided lenses with small focal length to prevent aberration of the beam by sharp focusing, when light does not behave by following the laws of radial optics.

The second version of transmission *d*STORM microscope with the fine control of the light intensity

Due to the instability of the Axiovert 200M microscope and the inability to insert mechanical parts for objective stabilization, I assembled another *d*STORM microscope on the Axiovert 100M microscope. For the illumination tube lens, I used the tube lens from the emission path of light extracted from the other Axiovert 100M microscope. Apart from that, the Axiovert100 microscope had an embedded post-magnifying lens, which additionally magnifies the microscope image by 2.5 times, which ensured the projection of every PSF (or the cloud of every fluorescent molecule) on nine or more pixels of the EMCCD chip. Therefore, every PSF was sampled correctly according to the Nyquist-Shannon sampling theorem.

Small solid-state excitation lasers of wavelengths 660 nm, 532 nm, 473 nm, and 405 nm I screwed on a metal plate (Rew B breadboard). The metal plate with excitation lasers I screwed to the active pneumatic optical table (**Figure 4**). The effectiveness of many optical components, such as the Acousto-optic tunable filter (AOTF), depends on the direction of the polarization of the laser beam. Therefore, I checked the direction of the polarization of the laser beams with polarizing filter, and I screwed the lasers to the plate in the direction in which the polarization of the outgoing beam was vertical. I joined the laser beams with dichroic mirrors into one line so that they pass through two apertures 10 cm away from each other, at the exit from the plate. Between these two apertures, I placed the Acousto-optic tunable filter (AOTF), which finely regulates the intensity of the laser beams with wavelengths between 400 and 650 nm. With the AOTF I finely adjusted the strength of excitation light and like this controlled the number of fluorescent molecules in the sample for STORM imaging. I placed two movable Neutral density filters with strength 2 and 4 on the plate with the lasers. Together they decreased the strength of the excitation beam million times for illumination during the observation of the sample, where blinking and strong excitation was not necessary.

The third version of the TIRF/HILO *d*STORM microscope with a stable focus

To increase the contrast in the sample, I assembled the third *d*STORM microscope with TIRF/HILO sample illumination (**Figure 5** and **Figure 6**). I introduced the beam into the microscope and aligned it as described in the chapter about the first version of the *d*STORM microscope. Then, I have inserted the TIRF mirror (M1, **Figures 6** and **7**) like an angle-mirror into the place of the back focal plane of the tube lens in the direction away from the microscope. The back focal plane of the tube lens is where the image of the sample is in focus, and where the image of the field aperture from the Köhler illumination system is in the focus. The image of the sample and the image of the field aperture are faithfully transmitted to the back focal plane of the tube lens because two lenses separate them away from each other by their focal lengths. In such a configuration, by changing the angle of the TIRF mirror (M, figures 6 and 7), the place of entry of laser beam into the tube lens and the angle of sample illumination was changed. At the same time, the position of the area of the sample illumination remains the same. After inserting the TIRF mirror, 30 cm in front of it in the excitation of the incoming excitation beam, I inserted the position mirror (M2, **Figure 6** and **Figure 7**).

To achieve even illumination of the sample, I expanded the excitation beam five times with a telescope (L5 and L4, Figure 6, and Figure 7), and I blocked the peripheral region of the laser beam with an aperture. Before inserting the telescope and the aperture on the path of the excitation laser beam, I placed two lenses with a focal length of 15 cm on the illumination path (L2, L3). I inserted lens (L1) between the TIRF mirror (M1) and the angle-mirror (M2), and the other (L3) 15 cm behind the field mirror (M2). I inserted the illumination aperture in the back focal plane of the second lens. The image of the aperture of excitation light was faithfully transmitted into the image plane, and it successfully blocked the weaker intensity laser light. In this way, the sample was evenly illuminated during imaging. To prevent the sample from blenching when the camera is not imaging, on the path of excitation light, I inserted an automatic shutter. The shutter was automatically opened by the camera during imaging and closed immediately after imaging.

To increase the stability of the sample during prolonged *d*STORM imaging, I placed the sample on the stable sample carrier. I attached stable sample carrier into the objective carrier of the microscope. I screwed in a 100 × oil objective of numeric aperture 1.4 in a sample carier and placed the sample above the objective.

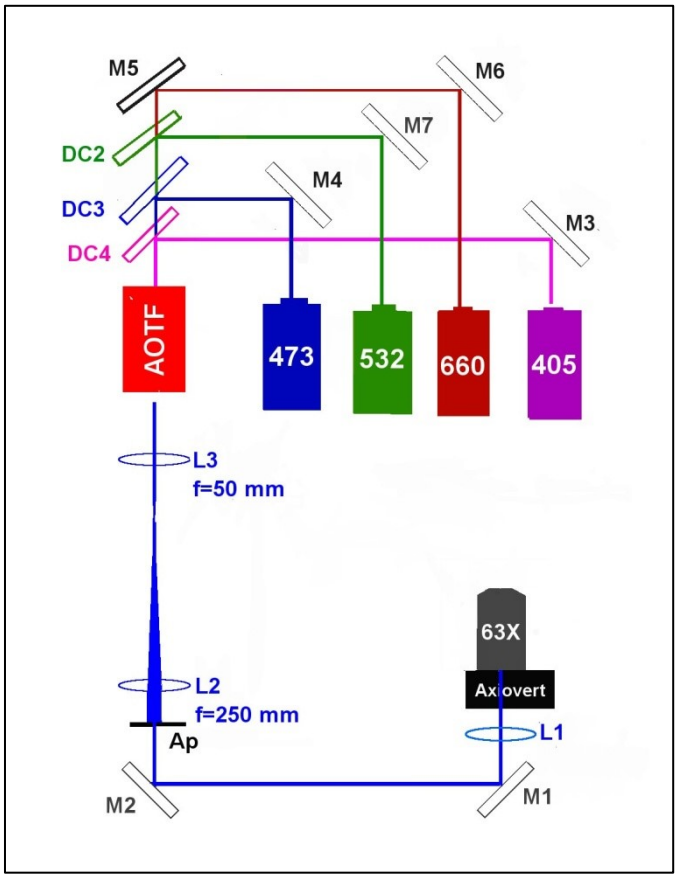

Figure 4. Illumination path of the second version of the *d*STORM microscope. The illumination path of the optical setup is composed of the 473 nm laser (473), 660 nm laser (660), 532 nm laser (532). Mirrors M3-M7 reflected the laser light through or from dichroic mirrors: 567 nm long-pass dichroic mirror (DC2), 505 nm long-pass dichroic mirror (DC3) and 425 nm long-pass dichroic mirror (DC 4) into the same line which goes through the Acousto-optical transmission filter (AOTF). After passing through the AOTF, laser line passes through lenses of focal length f=50 mm (L1) and focal length 250 mm (L2) and the iris aperture (Ap), then it is reflected from mirrors and (M2 and M3) to the tube lens (L1) and into the microscope (Axiovert) and through the 63 × objective (63 ×). The microscope body, together with optical parts inside, is depicted as a black rectangle (Axiovert). Optical components with precise information about their properties and producers are listed in **Table 7**).

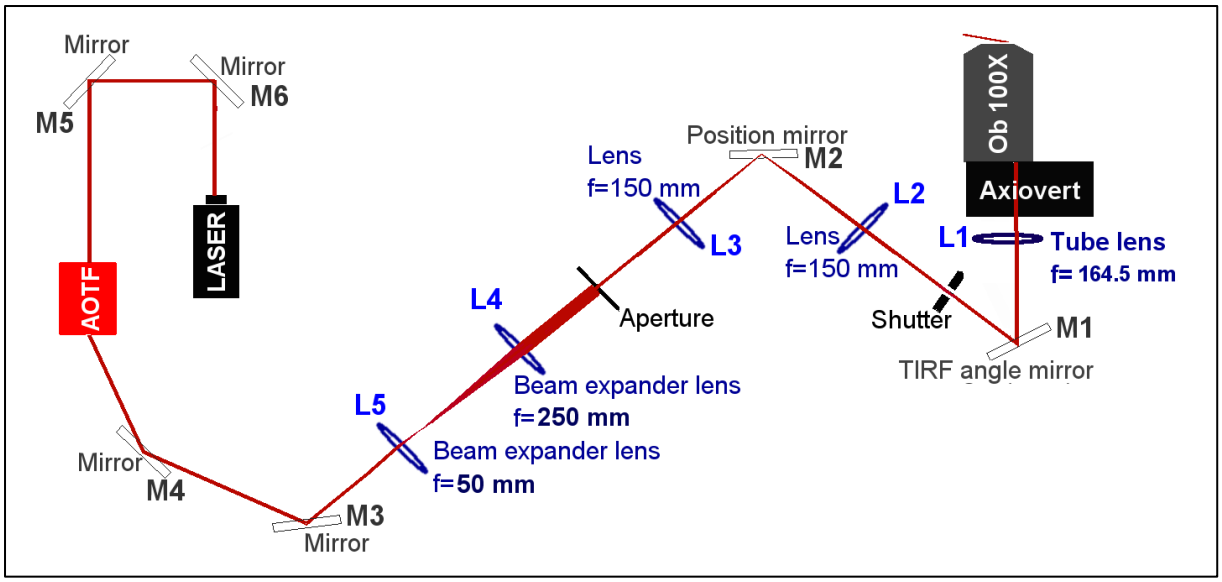

Figure 5. Scheme of the optical parts on the illumination path of the third and final version of the stable *d*STORM TIRF/HILO microscope. The beam from 660 nm laser (LASER) is reflected with two mirrors (M5 and M6) through acousto-optic tuneable filter (AOTF), and from two mirrors (M4 and M3) through the beam expander composed of the two lenses (L5 and L4). After the beam expander the beam goes through an aperture to the lens L3, then is reflected from the position mirror (M2) through lens (L2),then through the shutter to the TIRF angle mirror (M1)The lase beam is reflected from the TIRF angle mirror (M1) to the tube lens (L1) and the microscope (Axiovert) and through the 100x objective (Ob100 ×). Optical parts of the illumination part inside of the microscope body are symbolically represented with the black box named Axiovert. Ob100 ×

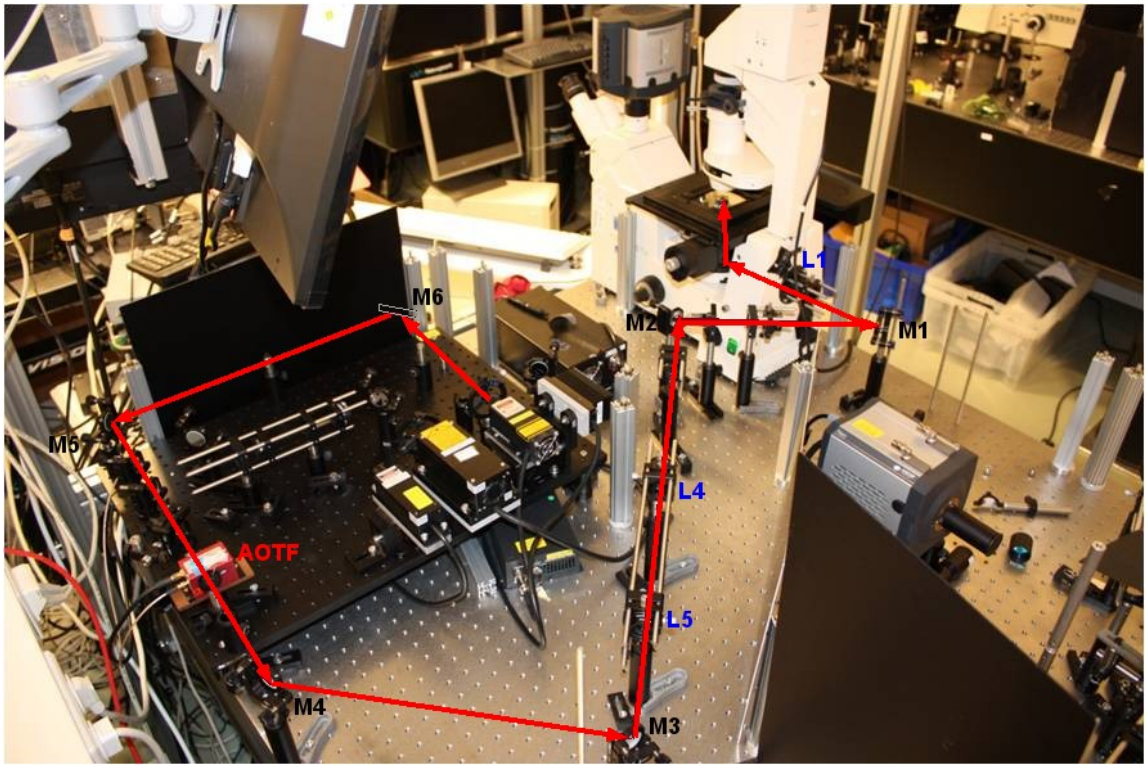

Figure 6. Photography of a third version of the self-build stable TIRF/HILO *d*STORM microscope in the phase of improvement. The beam from 660 nm laser (LASER) is reflected with two mirrors (M5 and M6) through acousto-optic tunable filter (AOTF), and from two mirrors (M4 and M3) through the beam expander composed of the two lenses (L5 and L4). After the beam expander the beam goes through an aperture to the lens L3, then is reflected from the position mirror (M2) through lens (L2), then through the shutter to the TIRF angle mirror (M1) The lase beam is reflected from the TIRF angle mirror (M1) to the tube lens (L1) and the microscope (Axiovert) and through the 100x objective (Ob100 ×).

Imaging of the blinking for *d*STORM

I positioned and imaged the samples in the program Micromanager, version 1.4. Micromanager controlled the camera and the automatic shutter. I controlled AOTF with the program Multi Digital Synthesizer (MDS software). I searched through the samples with excitation light dimmed 10 000 times with two ND filters. Before imaging the illumination for *d*STORM, I additionally magnified the image 2.5 times by inserting the post-magnification lens within the microscope. Then I manually adjusted the HILO angle so that it illuminates the focal plane and made a few images of the cells with an exposure time between 50 and 100 ms. Then I removed the ND filters and adjusted the strength of the excitation laser by adjusting the AOTF so that the strength of the excitation light for imaging of illumination is around 8 kW/cm^2. I adjusted the strength of the light for *d*STORM so that all fluorophores in the sample transit into a dark state at most 2 seconds after the beginning of exposure to the bright light. During imaging, I adjusted the strength of excitation light so that during 3-10 consecutive images, between 5 and 10 molecules simultaneously shine. I imaged samples with the back-illuminated electron-multiplying charged-couple device (EMCCD) camera Ixon X3 model DU 897D-CSO#BV from Andor(Belfast, UK) using around 180 × 180 pixels with camera settings like described in Table 12). For *d*STORM, I took 60000 images of blinking.

Table 12. EMCCD camera settings during imaging for *dSTORM*

Parameter	Setting
CCD Temperature	-68 °C
Exposure Time	15 ms
Electron Multiplier Gain	300
Frame Transfer	on
Baseline Clamp	Enabled
Vertical Shift Speed	1,7 µs
Vertical Clock Voltage Amplitude	Normal
Horizontal Readout Rate	5 MHz
Pre-Amplifier Gain	5,1x

For imaging the samples of microtubules labeled with Alexa Fluor 488 dye and DNA origami rectangles, I used the 488 nm argon laser line. For imaging the samples of microtubules labeled with Cy 3 dye, I used the 532 nm Solid State Diode (SSD) laser. For imaging the samples of microtubules, actin filaments, and kinetochores labeled with Alexa 647 dye, I used the 660 nm SSD laser.

Data processing

*D*STORM reconstruction

I made the *d*STORM reconstructions of the blinking images in the program Quick-PALM (Henriques 2009.) with program parameters like described in table 12. Quick-PALM works as a plug-in within the ImageJ program. First, I calculated the table with coordinates of localizations. Then I reconstructed the high-resolution image with the desired pixel size from the table of localizations.

Table 13. Quick PALM program parameters for *d*STORM reconstructions

Parameter	**setting**
Minimum signal to noise ratio	10
Maximum FWHM	4 pixels
Image plane pixel size	64 nm
Minimum symmetry	0%
Local threshold (% maximum intensity)	20
Maximum iterations per frame	1000

The calculation of localizations in program QuickPALM is based on the determination of the two-dimensional Gaussian curve from the histogram of photoelectrons gathered on the EMCCD chip of the camera. The position of the fluorophore is then defined as the top of the two-dimensional Gaussian curve approximated on a two-dimensional histogram of photons collected on the EMCCD chip (Thompson et al. 2002). For a proper reconstruction, each PSF which is used for the calculation of localization must come from only one molecule of the fluorophore. Images of the samples with the

visible structures of the cell, I acquired at the beginning of the measurement for *d*STORM, contain many overlapping PSF. They were not analyzed to find localizations of blinking molecules. Only images captured 10 or more seconds after the beginning of bleaching were used for the reconstruction. They contained only separated individual blinking molecules. On those images, the original fluorescent structure visible before the bleaching is not visible due to the transition of most of the fluorophores into the dark state.

QuickPALM processes every image in the sequence separately, so the fluorophore that shines on several consecutive images will be localized separately every time. By turning the localization table into an image with arbitrary pixel size, the program will join a grey level to every localization depending on the precision of localization to a pixel within whose area the localization was found. When displaying two localizations in the area of one same pixel, their grey levels will be added, and it will appear as one localization.

Testing the stability of the microscope

The movement of the miscroscope during imaging would cause movement of the sample. The movement of the sample during *d*STORM imaging should be significantly smaller than the desired resolution power one wants to achieve if no drift-correction procedure is used. For that reason, I tested the stability of the microscope by imaging fluorescent beads with the diameter of 100 nm for every 5 seconds during two hours I reconstructed the images of the fluorescent beads with the Quick-PALM program as *d*STORM reconstructions. The shifting of the microscope during a measurement would cause the elongation of balls on the reconstructed image in the same direction. I measured the difference between the horizontal and vertical diameter of the beads on images reconstructed with Quick-PALM. The diagonal movement of the sample in regards to the measured dimension would have the same result in the subtraction like no movement. I also measured dimensions of the reconstructed fluorescent beads in the direction of angle 45° in the image and perpendicular to it. On reconstructed images, I measured the diameter of reconstructed beads structures that had PSF on wide-field images big between 200 and 300nm and were separated at least 300 nm from the neighboring PSF. The shifting of the sample during a measurement would cause the elongation of balls on the reconstructed image in the same direction.

Statistical analysis and measurement of the DNA origami

To test the resolution of the *d*STORM microscope, I compared images of the DNA origami on *d*STORM and Atomic Force Microscope (AFM) images. AFM images were made by Andreas Kopielski as per the protocol described in Rothemund 2006. DNA origami rectangles were designed to make a rectangle 50 nm wide and 100 nm long (**Figure 7**). One molecule of Alexa-Fluor 488 was placed on one long side of the rectangle. Diagonally from this fluorophore, two other fluorophores were placed on the opposite side of the rectangle. Molecules of fluorophores were placed to make a triangle and to be separated 30 nm, 82 nm, and 102 nm. I measured the distances of individual fluorophores on DNA origami rectangles manually on *d*STORM reconstruction images with pixel-size of 1 nm in the

program ImageJ. For the preliminary analysis and searching, I used the *d*STORM images with pixel-size of 10 nm.

Fluorophores distant between 15.56 nm and 50 nm on *d*STORM images, I considered as fluorophores from the DNA origami rectangles placed to the distance of 30 nm. Fluorophores separated below 15.56 nm I considered as multiple localizations of one fluorophore. I set 15 nm as a limit because that is the standard deviation of the distance between fluorophores separated below than 50 nm. I set the value of 50 nm as the upper limit to avoid overlapping with the measurement of the distance between the third fluorophore, placed on the DNA on origami to be separated from the first two molecules of the fluorophores around 70 and around 100 nm (**Figure 7**). When the same fluorophore on DNA origami was localized more than once, I measured the distance between the centers of multiple localizations.

To determine the resolution power of the third version of the self-build TIRF/HILO microscope I measured the distance between multiple localizations of the same fluorophore on the DNA origami or the distance between fluorophores distant below 15.56 nm.

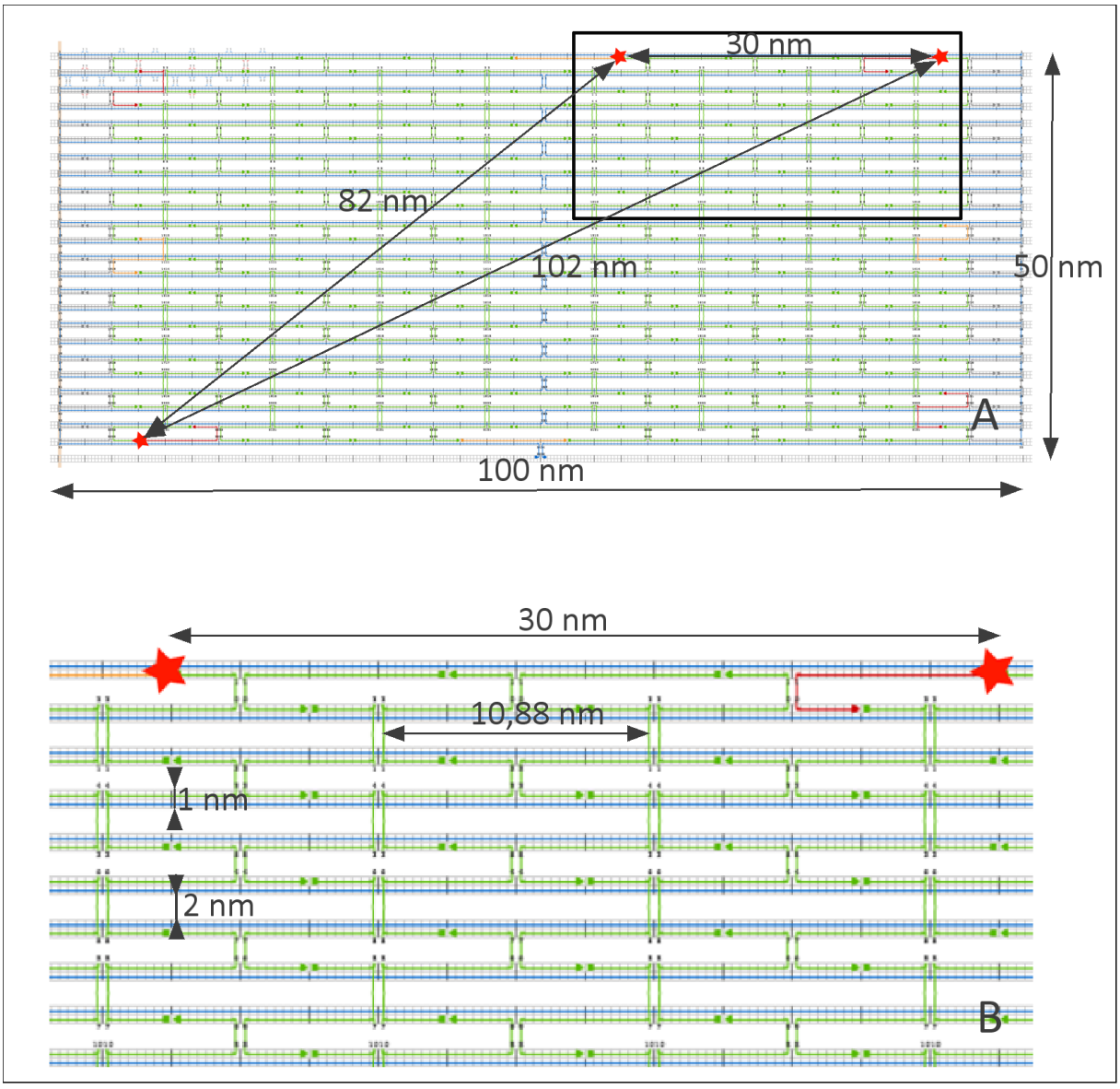

Figure 7. A) A scheme of the DNA origami rectangle test sample with predicted dimensions. DNA origami rectangles were designed to create a rectangle 50 nm wide and 100 nm long. On DNA origami rectangles, three individual molecules of Alexa 488 fluorophore (red star) are placed to be separated 30 nm, 82 nm, and 102 nm. **B)** Magnified detail from the frame in the image with the predicted dimensions of the inner structures. Cross-linking of two parallel lines inside of the rectangle should be separated 10.88 nm, the predicted distance between two parallel DNA strands is 2 nm, and the predicted thickness of the DNA strand is 1 nm.

Statistical analysis and measurement of the kinetochores

I measured the dimensions of the kinetochores on *d*STORM reconstructed images with a pixel size of 10 nm. I determined pixel size of 10 nm arbitrarily because I aimed to achieve resolution below 30 nm. I estimated this resolution to be necessary to resolve the kinetochore chromatin due to its compactness described in previous research (Ribeiro et al. 2010.). The bigger is the precision of localisations, and the smaller is the pixel size, lower is their accuracy. I displayed the calculated table of *dSTORM* localisations like an image with pixel size 10 nm, because this was the bigger pixel size where calculated localisations appeared connected in a compact structure with resolved details of

specific and fine pattern. On images with pixel size 20 nm and bigger, fine details inside of the kinetochore structure remained unresolved. On images with pixel size 5 nm and smaller, individual localisations appeared as distanced dots where it was difficult to observe and to measure specific patterns. On *d*STORM reconstructions, localisations determined more precise were displayed brighter. Before the measurement of kinetochore dimensions, I adjusted the contrast on *d*STORM reconstructions to se as many as possible details within the kinetochore.

For precise *d*STORM reconstruction, the blinking of individual fluorophores has to be bright and short. Longlasting bright events are caused by the simultaneous blinking of close molecules due to the insufficient reduction potential of the blinking buffer or by insufficient laser intensity to produce reversible dark states effectively. Another reason for imprecise localization is the out of focus position of the sample. Imprecise localizations are visible in the reconstructed images as the round shapes of samples that are not round and with bright details in the center (Henriques et al. 2009).

For reconstructions of the kinetochore chromatin, I used only blinking images with bright states shorter than 150 ms. I considered the reconstruction of a kinetochore valid if the reconstruction contained localizations without details twenty or more times brighter than the rest of the structure. I did not measure kinetochores of cells where more than a third of reconstructed kinetochores are deficient because such a significant portion of improperly reconstructed kinetochores is caused by uneven illumination of the sample, or by buffer depletion due to the long sample observation and imaging.

To recognize in which phase of the cell cycle the reconstructed cell is, I measured the portion of paired kinetochores, the distance between sister kinetochores, the number of pairs of the sister kinetochores on the spindle axis and the standard deviation of the angle between the axis between sister kinetochores.

Measurement of the length and width of the kinetochore chromatin

I manually measured the dimension of the kinetochores in the program ImageJ. The *d*STORM reconstructions showed that their shape and structure look like a compact rectangle. Before measuring the dimensions, I drew a rectangle around every kinetochore. The measurement of the kinetochore width and length are graphically shown in figure 12. I measured the length of the kinetochore to be parallel with the longer side of the rectangle, and width to be parallel with the shorter side. The only exception is the separate measurement of the length and width of the paired kinetochores. I measured the width of the paired kinetochores parallel with the side of the rectangle, which is under a smaller angle in regards to the axis between the sister kinetochores. I measured the length of paired kinetochoes as the remaining side. Dimensions measured this way are specified in the text. I measured the length where the kinetochore is the longest and width where the kinetochore is widest. Some kinetochores had a tail on one side. I measured their dimensions to the end of the tail. On some reconstructions of the kinetochores, it was possible to see intermittent parts of localizations distant from the rest of the compact structures. I considered them parts of the kinetochore if they were closer than 50 nm to the compact part or if there were three or more of

them. The structures of kinetochores, which are less than 50 nm apart, I considered to be one kinetochore, while those further apart, I counted as two separate kinetochores.

Measurement of the thickness and distance between the threads within the kinetochore chromatin

I defined the thickness of kinetochore threads as the full width at the half maximum (FWHM) on the intensity plot of the profile pulled through the kinetochore (**Figure 8**). To avoid the artificial variations caused by accidental pulling through a single pixel due to the "pixelization" of the image, I made the intensity plot by averaging values on five pixels. I did the averaging in the program ImageJ by adjusting the thickness of the profile line on five pixels. I selected that width because by observing the kinetochores, I determined that most threads can be distinguished as separate structures at around 50 nm, which are five pixels in the reconstructed analyzed image. When measuring the width of several neighboring threads with different brightness, I measured the thickness of all threads at the half maximum of the dimmest threads with the lowest peak of intensity. Width of the threads with lows of intensity brighter than the halve maximum of the dimmest threads I measured between lowest values of the intensity plot. I measured the width between their minima (**Figure 8**).

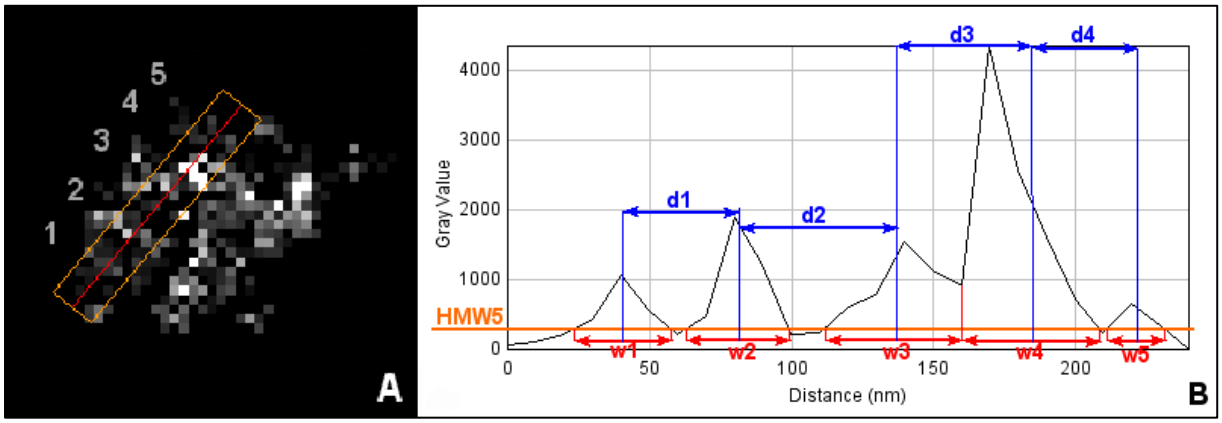

Figure 8. Measurement of the thickness and distance between kinetochore threads. A) *d*STORM reconstruction of a kinetochore. On the reconstructed image, a red profile line is drawn to perpendicular to kinetochore lines (1-5). A profile line is set to be thick 5 pixels (orange). **B)** Intensity plot across a profile drawn over the kinetochore threads. The intensity plot is calculated by averaging intensity values of 5 pixels on the line perpendicular to the marked profile line. The thickness of kinetochore threads (w1-w5) is measured at the half maximum of the thread with the lowest intensity (w5). Threads 3 and 4 are separated with lows of intensity bigger than the HMW5. Their width is measured between the lowest intensity value and HMW5. Distance between kinetochore fibers (d1-d4) is measured between the middle of the fiber width at the HMW5.

I measured the distance between the centers of kinetochore threads on the same intensity plot as the width. I defined the center of each thread as the center of the length between points of intersection of the plot intensity and the line, which defines the position of the half-maximum intensity of the dimmest thread (**Figure 8**).

Arrangement of cells according to the phases of the cell cycle

I arranged the reconstructed cells according to the phases of the cell cycle as per the portion of recognized paired kinetochores and angles between sister-chromatids concerning the equatorial plate. I grouped the *interphase* cells with more than 40 % of recognized paired kinetochores into *phase G2* and the cells with less than 20 % into *phase G1*. Some *interphase* cells had an unusually large number of above-average long kinetochores, and several big unfolded kinetochores bigger than 500 nm called *gigantic* kinetochores. I assumed that the unfolded appearance is a consequence of chromatin unfolding due to the replication. I grouped the cells which had 15 % of kinetochores longer than 370 nm and at least two *gigantic* kinetochores into the *S phase*. Kinetochores of the cells with between 20% and 40 % of paired kinetochores and without gigantic, I analyzed only as *interphase* kinetochores.

The catching of kinetochores by the spindle apparatus microtubules in mitosis starts immediately after the degradation of the nuclear envelope and causes the orthogonal orientation of chromosomes concerning to the equatorial plane. It precedes the alignment of chromosomes in the equatorial plane, and I used it for the recognition of mitotic cells. I considered as *mitotic* cells those cells with the standard deviation of angles between the axes which connect the centers of sister-kinetochores lower than 25°, and *interphase* cells with the standard deviation of angles over 70°. I manually measured the angles between the axes which connect sister-chromatids in program ImageJ during the measurement of distances between sister-kinetochores. To recognize the progress of mitosis, in *mitotic* cells, I measured the distance between sister-kinetochores. In every mitotic cell, I measured the portion of kinetochore pairs located on the estimated division plane (**Figure 9**). The estimated division plane is an axis that intersects the highest possible number of lengths between sister-chromatids.

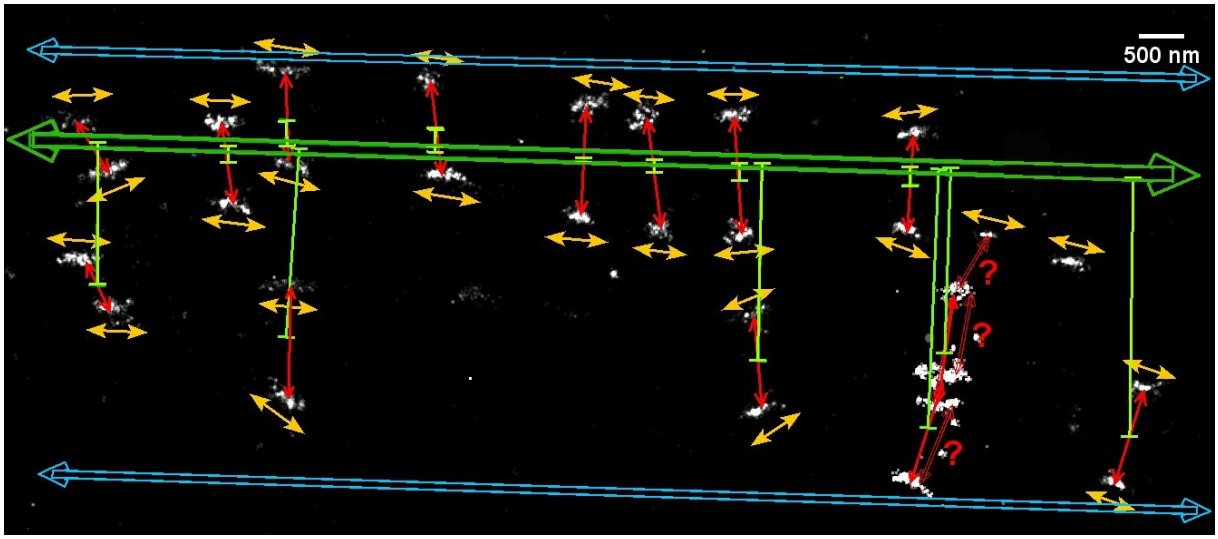

Figure 9. Graphic presentation of the measurement of the number of sister kinetochore pairs in the division plane and the measurement of the width of the kinetochore space. Division plane (outlined green arrow) is estimated to intersect a maximal number of lengths between sister kinetochores (red arrow). The distance of the sister kinetochore pair from the division plane (green bar) is measured from the middle of the length connecting two sister kinetochores. Width of the kinetochore space (filled blue arrow) is measured perpendicular to the division plane as the sum of the distance of two kinetochores most distant from the division plane.

Nocodazole depolymerizes microtubules so the chromosomes cannot align in the equatorial plate. For this reason, I arranged the nocodazole-treated cells per the portion of recognized sister kinetochores in the group *G1 phase* and the group *G2 phase and mitosis*. I grouped the *interphase* cells with more than 40 % of recognized paired kinetochores into *phase G2 and mitosis*, and the cells with less than 20 % into *phase G1*. Nocodazole changes the architecture of the kinetochore (**Figure 32**, **Figure 33**), so I didn't group the treated cells into the S phase according to the number of irregular kinetochores, average length, and number of gigantic kinetochores. Kinetochores of nocodazole treated cells with between 20% and 40 % of paired kinetochores I analyzed only as nocodazole treated kinetochores.

Identification of sister kinetochores

I considered sister-kinetochores in *interphase* cells by requiring kinetochore to be separated between 500 and 1000 nm, which in the vicinity of 1000 nm did not have a third kinetochore (**Figure 10A**). In *mitotic* cells, the chromosomes are aligned in the equatorial plate. Sister-kinetochore-couples have mutually parallel lengths between two kinetochores of the sister pair. Mitotic kinetochores are elongated, and the direction of the sister kinetochore elongation is mutually parallel and more or less parallel to the division plane. For this reason, I considered sister kinetochores in mitotic cells kinetochores, which were between 500 and 1500 nm apart and whose direction of elongation was parallel (**Figure 10B**). I measured the distance between sister-kinetochores between their centers (**Figure 11**).

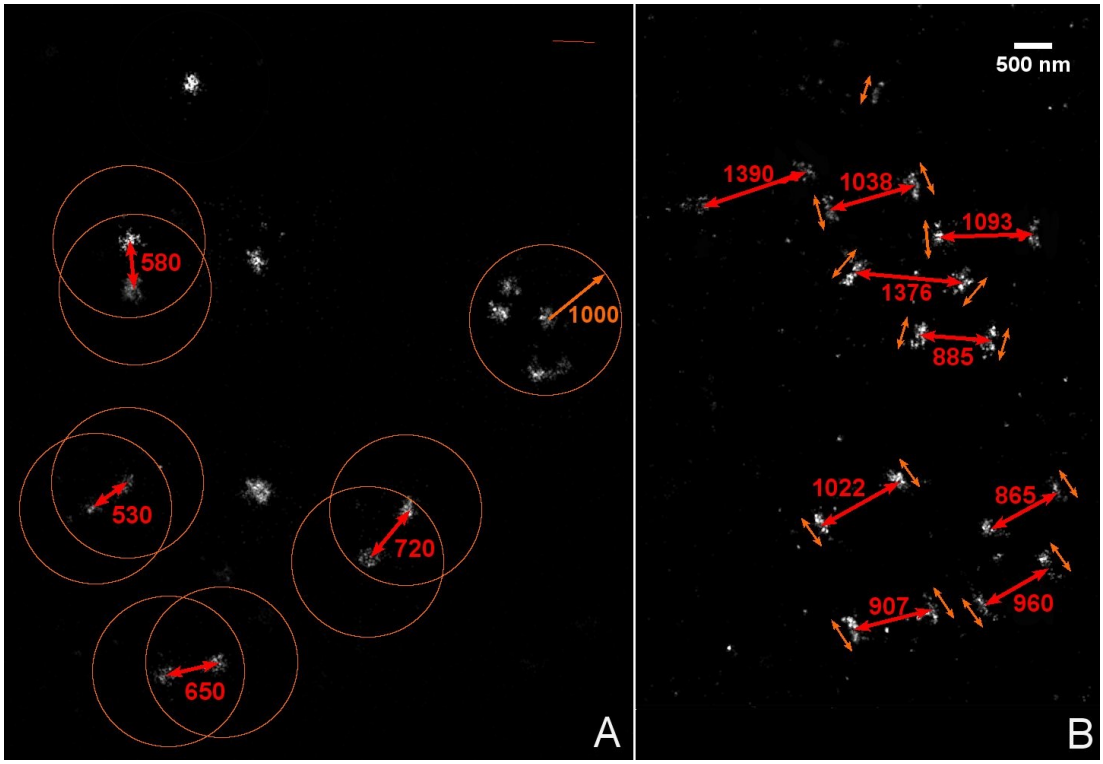

Figure 10. Determination of sister kinetochores A) In the interphase cells, sister-kinetochores are separated between 500 and 1000 nm (double red arrows). If kinetochores in the vicinity of 1000 nm (orange circles) have two or more kinetochores, sister-kinetochore pairs are not identified. **B) In mitotic cells,** sister-kinetochore pairs orient around the division plane. They can be recognized by parallel orientation (orange double head arrows), and they are 800 to 1400 nm apart (double red arrows).

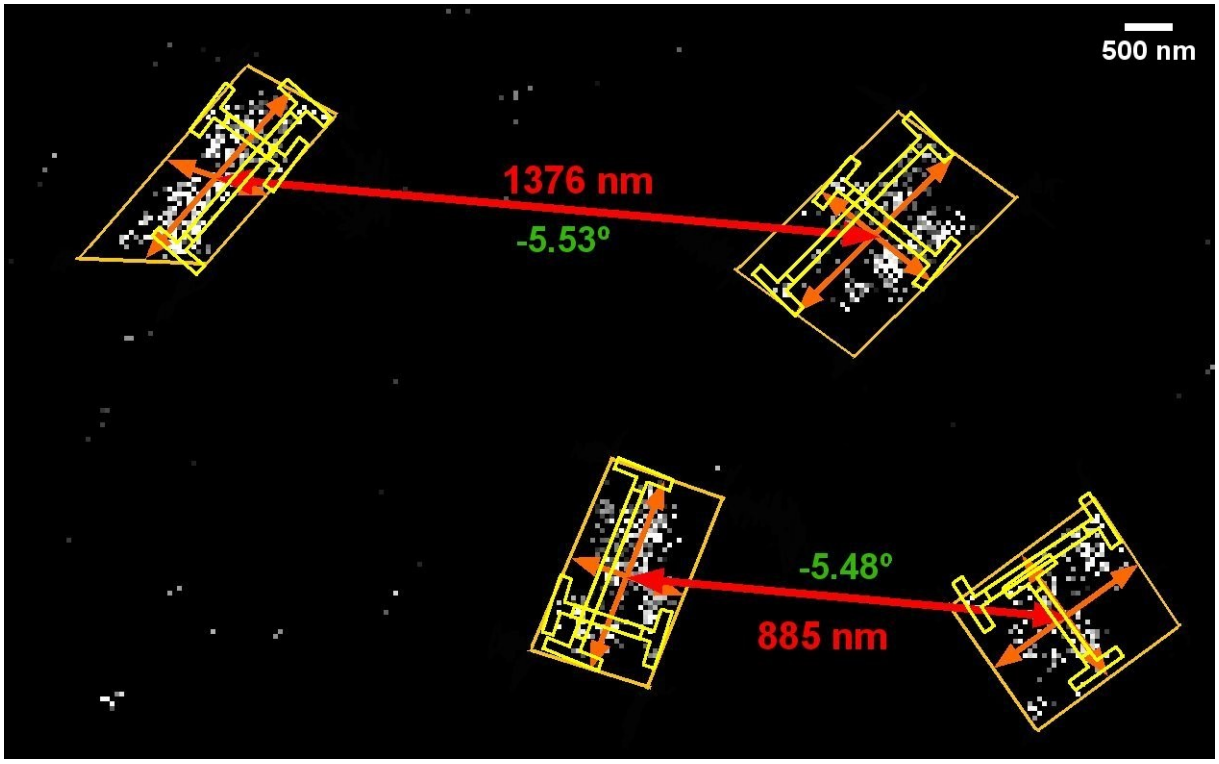

Figure 11. Measurement of kinetochore dimensions, distances between sister kinetochores and their angle. Distance between sister-kinetochores (red) is measured from their center together with the angle (green). Around each kinetochore, a rectangle is drawn (yellow). The center is at the intersection of lengths connecting the middle of opposite sides of a rectangle (orange arrows). Kinetochore width and length (yellow outlined bars) are measured parallel with the closest side of the drawn rectangle. Kinetochore width is measured on the widest part of the kinetochore, and length is measured on the longest part.

Stability of the microscope

The drifting of the sample and the microscope during *d*STORM imaging must be significantly smaller than the distance one wants to resolve. This sample drift on *d*STORM reconstructions results in an elongation of all structures in the same direction. I checked for movement during imaging on the third self-build microscope with the stable nosepiece stage (IX2-NPS Olympus) by imaging of fluorescent bead for two hours and defined the movement of the sample during the measurement as the difference between the horizontal and vertical diameter of the balls on *d*STORM reconstructions. Ideally, drift should be expressed as a vector of the position of the bead on the first image and the last image. Unfortunately, 100 nm beads I imaged were dim, and I could not achieve images with bright PSF to precisely determine their center of localization and to express it as a vector. Localisations of beads looked like a spherical cloud with a diameter of 100 nm and I decided to measure the difference in their horizontal and vertical diameter to determine the possible movement of the sample during imaging. The diameter of the same beads was also measured at angles 45° and -45° and substracted to detect possible diagonal drift. (**Table 14**).

Table 14. Measurement of the sample movement during imaging. The difference of the diameters of fluorescent beads measured horizontally and vertically (0°and 90°) and at angles -45° and 45°. The difference was measured after 5 minutes, 20 minutes, and 2 hours of imaging.

time	0° and 90°	45° and -45°
5 min	0.906294	0.894353
20 min	2.665	2.38
2 h	3.76	5.23

Results

Testing measurements

Preliminary testing

To specifically label the kinetochore chromatin for *d*STORM imaging, I tested the kinetochore specificity of sixteen different antibodies and found nine antibodies that specifically label kinetochores (Supplementary data **Table 26**, **Figure 44**).

Blinking properties of the fluorophores and the photochemical conditions of blinking reaction

Within this doctoral research, the photochemical and photo-physical properties of various commercially available fluorophores were tested. The research was conducted by Kathrin Klees under the mentorship of Professor Rainer Heintzmann, Ph.D., and my co-supervision. This research was published in the form of a master's thesis entitled "Investigation of fluorophore switching performance for multicolor *d*STORM imaging" and defended at the Friedrich Schiller University in Jena. In the research, the switching performances of fluorophores Alexa 488, Atto 532, Atto 550, and Cy3 were investigated. The temporal relationship between dark and bright states, the portion of irreversibly bleached fluorophores, and the number of detected photons per on-state were measured. The properties of switching performances of fluorophores were tested in media with different concentration of reducing agents which influence the mentioned switching performances. In the third self-build TIRF/HILO microscope for *d*STORM, described in the Materials and methods, the fluorophores Alexa 488 and Cy3 had longer dark states in the tested conditions. Alexa 488 and Cy3 produced more photons during bright states than Atto 532 and Atto 550, which makes the former more suitable for application in *d*STORM. The merchaptoetilamine in neutral conditions proved to be a better reducing agent than cysteamine (also called) merhcaptoethanol.

Testing the resolving power on artificially designed samples of DNA origami

To precisely determine the resolving power of the *d*STORM measurement test samples of DNA origami with anticipated dimensions of 50 × 100 nm were designed. Three molecules of fluorophore Alexa Fluor 488 were placed on a DNA origami rectangle to be arranged into a triangle with an anticipated length of sides 30, 70 and, 110 nm (chapter Material and methods **Figure 7**). The DNA origami samples were deposited on the plastic surface for AFM, and on a glass coverslip for *d*STORM. DNA origami rectangles were prepared and imaged on the atomic force microscope (AFM) by Andreas Kopielski at the Leibniz Institute of Photonic Technology in Jena (**Figure 12A** and **12B**). An optical microscope cannot image non-fluorescent parts of the DNA origami, so I defined the actual shape and dimensions of the DNA origami disposed on the glass coverslip on their AFM images. According to their measured dimensions (**Table 15**), I estimated the expected distance of the fluorophore on *d*STORM images (**Table 16**). DNA has a bigger affinity to bind glass than an uncharged plastic surface like AFM mica surface, which might affect the DNA origami dimension. This change

might be different along the length and different along the width of the DNA origami. I assumed that eventual widening or shrinking along each dimension is uniform only along the measured dimension.

DNA origami structures placed on the glass coverslip (**Figure 12B**) were not as regular as those placed on the mica surface for AFM **Figure 12**), but the rectangular shape was recognizable in around half of the DNA origami structures on the glass coverslip

Table 15). The origamis on the coverslip were 6 nm shorter and 10 nm narrower than those one placed on the surface for AFM. *D*STORM reconstructions of the DNA origami structures showed two closer fluorophores of the DNA origami. Their anticipated distance calculated based on dimensions measured with AFM corresponded to the average distance between two closer fluorophores on *d*STORM reconstructions (**Table 16**). The arrangement of three fluorophores from the DNA origami was noticed only six times on the surface of 320 μm^2, so the DNA origami rectangles under *d*STORM reconstructions were analyzed only based on the two closer fluorophores. The density of recognized DNA origami rectangles under *d*STORM reconstructions was about twice as smaller than the density of DNA origami rectangles on AFM images, which indicates that approximately every other DNA origami is recognized by *d*STORM. Besides fluorophores bound on DNA origami rectangles, samples of DNA origami rectangles disposed on glass coverslip also contained unspecifically bound fluorophores.

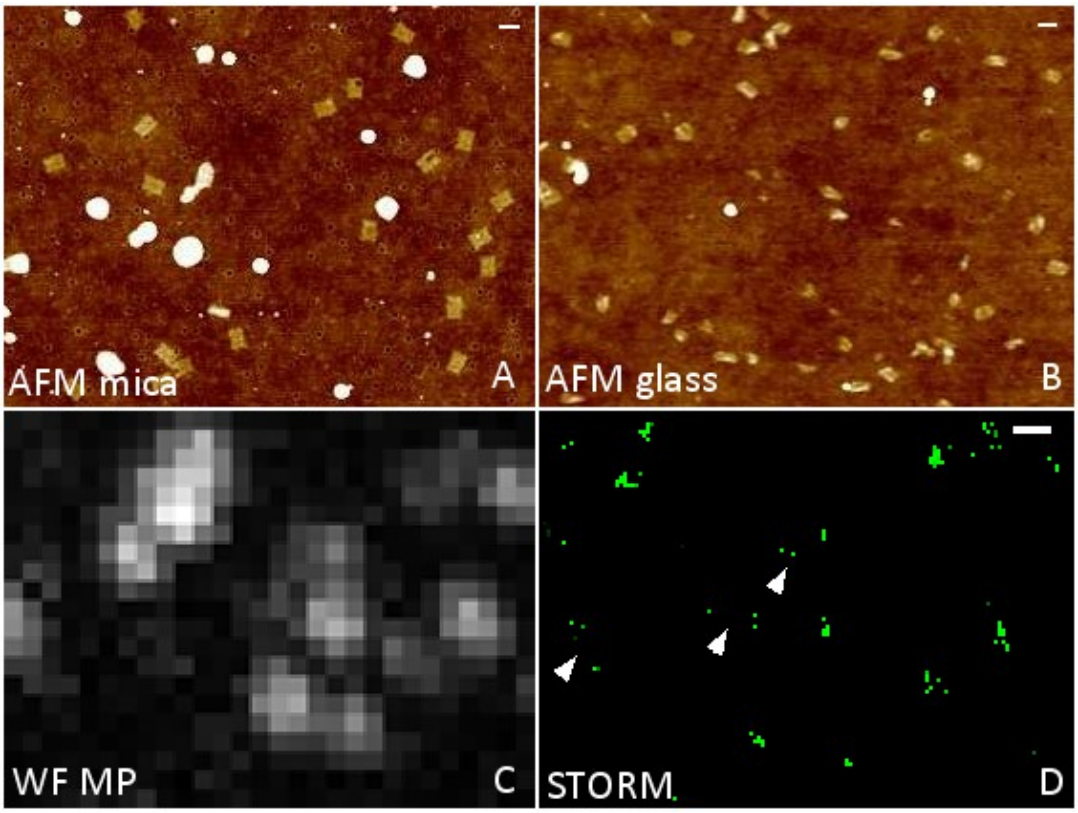

Figure 12. Microscopic images of the DNA origami structure. A) Atomic force microscopy of the DNA origami deposited on mice surface. **B)** Atomic force microscopy of the DNA origami rectangles deposited on the glass coverslip. **C) The** maximum intensity projection of the blinking of the DNA origami rectangles disposed on the glass coverslip. Images are captured on the third TIRF/HILO *d*STORM microscope. **D)** *D*STORM reconstruction of the blinking of DNA origami rectangles reconstructed from the blinking of molecules projected in image C. Arrows point to the fluorophores recognized as parts of DNA origami structures. Scale bars 100 nm.

To determine the resolution power of the *d*STORM reconstruction, I measured the distance between multiple localizations of the same fluorophore on *d*STORM images of the DNA origami rectangles (**Figure 13**). The measured distance between multiple localizations of the same fluorophore was between 15.56 and 2.1 nm. In the measurement of the distances between two localizations of the same fluorophore and the distances between two close fluorophores value of the 15.56 nm is taken as a limit for the determination whether two localizations belong to the same or two close fluorophores because this was the value of the standard deviation of measured distances between all fluorophores closer than 50 nm.

DNA origami rectangles placed on a glass surface were mildly distorted, and the perfect reproducibility of shapes as published in the works of Tinnefeld was not achieved. Even though improving the techniques of placing DNA origami rectangles on a glass coverslip would produce a better ruler for measurement of precision of localization and resolution of *d*STORM microscope, this would surpass the subject and the aim of this doctoral research.

Table 15. Comparison of dimensions of the DNA origami rectangles placed on the mica surface and placed on the glass coverslip. Properties of DNA origami rectangles are measured on atomic force microscopic images of the DNA origami rectangles deposited on the mica surface (mica) and deposited on a glass coverslip (coverslip). The table shows the average length of DNA origami rectangles, a standard deviation of length (st. dev. of length), average width, a standard deviation of width (st. dev of width), average width and length ratio of individual origamis (Width/ length), the ratio of DNA origami rectangles that looked similar like rectangles (recognizable rectangles), the ratio of DNA origami rectangles with a regular rectangular shape (regular rectangles), the ratio of DNA origami structures that looked like distorted rectangles (distorted rectangles), the ratio of DNA origami rectangles with irregular shape (irregular), and the number of measured origamis.

DNA origami dimensions	mica	coverslip
Average length	90 nm	84 nm
St. dev. of length	5 nm	12 nm
Average width	65 nm	54 nm
St. dev. of width	3 nm	8 nm
Width/length aspect	0.6	0.7
Recognizable rectangles	100 %	51 %
Regular rectangles	97 %	18 %
Distorted rectangles	3 %	33 %
Irregular	0	49 %
No. of measured	36	26

Table 16. Comparison of anticipated and measured distances of fluorophores on the DNA origami structures. The table shows distances for two molecules of Alexa Fluor 488 placed to be separated 30 nm (fluorophore distance). Distances are anticipated for DNA origami rectangles imaged with AFM microscope on the mica surface (AFM-mica) and imaged on the glass coverslip (AFM-coverslip). The distance of fluorophores is anticipated based on DNA origami width and length measured on AFM images. Distances of two fluorophores (fluorophore distance) are measured on *d*STORM images of DNA origami rectangles disposed on the glass coverslip (*d*STORM-coverslip). The table also shows the standard deviation of the fluorophore distance (fluorophore distance st.dev.) for those fluorophores, the number of measured DNA origami rectangles (No of measurements), and the calculated density of the measured DNA origami rectangles on the imaged surface per square micrometer of the surface (density/ μm^2).

	AFM – mica (anticipated)	**AFM – coverslip** (anticipated)	***D*STORM – coverslip** (measured)
Fluorophore distance	30 nm	28 nm	28 nm
Fluorophore distance, st. dev.	1.6 nm	4.2nm	8.2 nm
No. of measurements	36	26	480
Density / μm^2	6 / μm^2	2.8 / μm^2	1.5/ μm^2

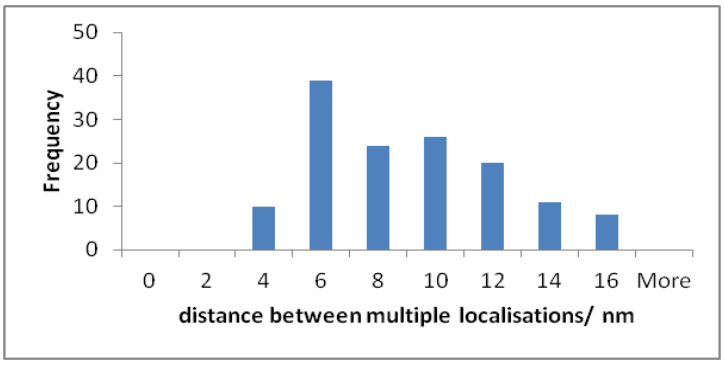

Figure 13. Histogram of distances between multiple localizations of the same fluorophore on DNA origami

Resolving power of *d*STORM on the test samples of microtubules and actin fibers

Simultaneous blinking of close molecules causes typical artifacts of localization microscopy. They appear like a blur in an area of a thread crossing (Henriques 2009). To examine the capability of *d*STORM imaging and the faithfulness of reconstruction, I imaged and reconstructed the images of microtubules labeled with the dyes Cy3 and Alexa 488 using the first self-build *d*STORM microscope. The obtained reconstructions faithfully showed the crossings of microtubules with the same sharpness as the rest of the structure (**Figure 14** D, E, and F). The smallest distinguishable structures in microtubule samples on those images were around 70 nm wide (**Figure 14 E**).

To test the resolving power of the third *d*STORM beyond the limit determined by the size and density of labeling with immunoglobulin antibodies, I imaged and reconstructed actin fibers labeled with phalloidin attached to Alexa Fluor 647. Phalloidine Alexa Fluor 647 is around one nanometre long. The obtained *d*STORM reconstructions faithfully showed the arrangement of actin filaments in high-resolution (**Figure 15**).

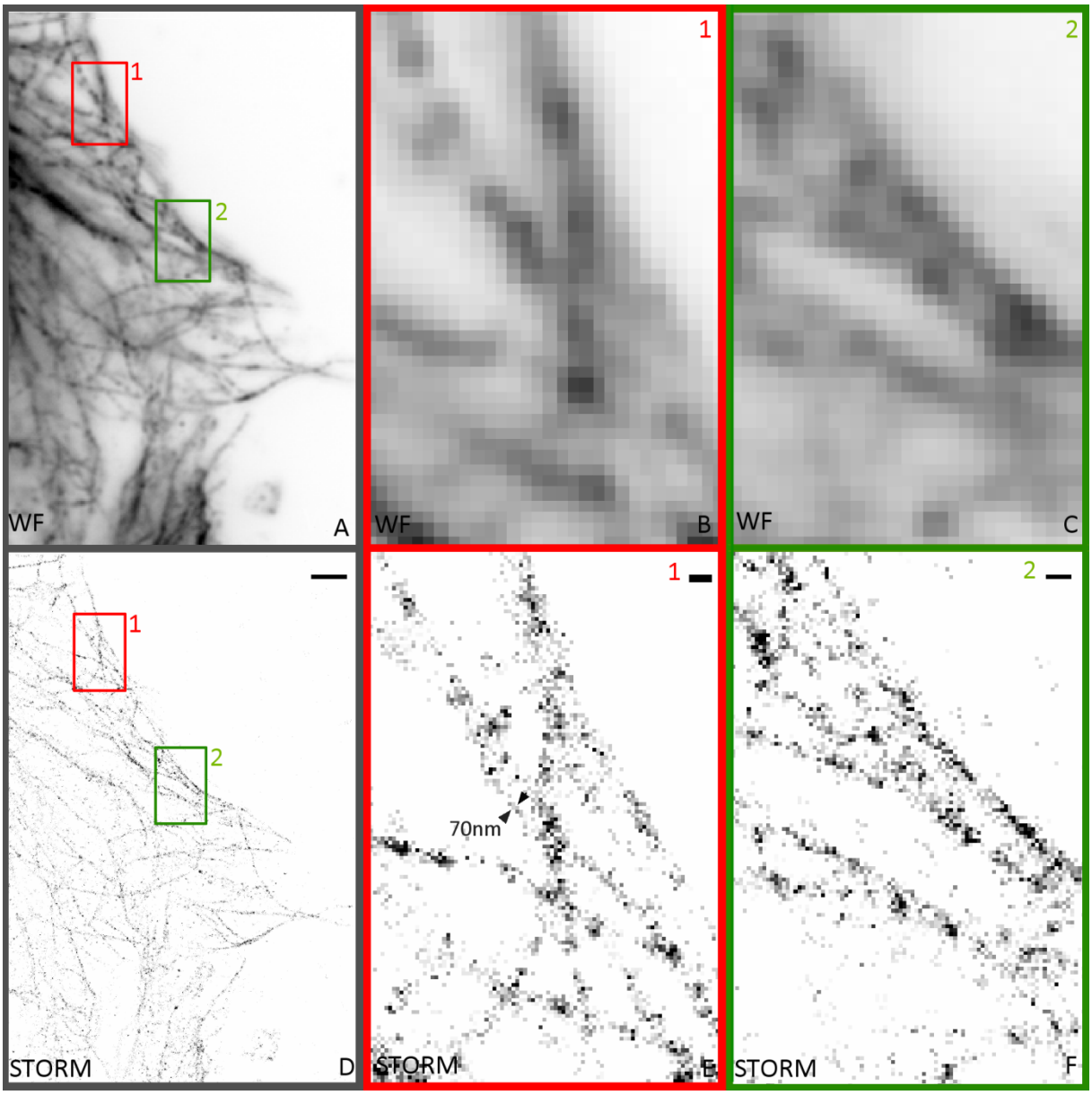

Figure 14. *D*STORM reconstruction of test samples of microtubules. A) A wide-field image of microtubules labelled with primary antibodies and secondary antibodies dyed with Cy3. This image is taken before the imaging of blinking for *d*STORM. **B)** A magnified detail from image A labeled with red frame 1. **C)** A magnified detail from image A labeled with green frame 2. **D)** *D*STORM reconstruction of the same cell depicted in image A. Scale bar 2µm. E) *D*STORM reconstruction of a detail from the red frame 1. The detail between arrows is 70 nm wide. Scale bar 200 nm. **F**) *D*STORM reconstruction of a detail from the green frame 2. Scale bar 200 nm.

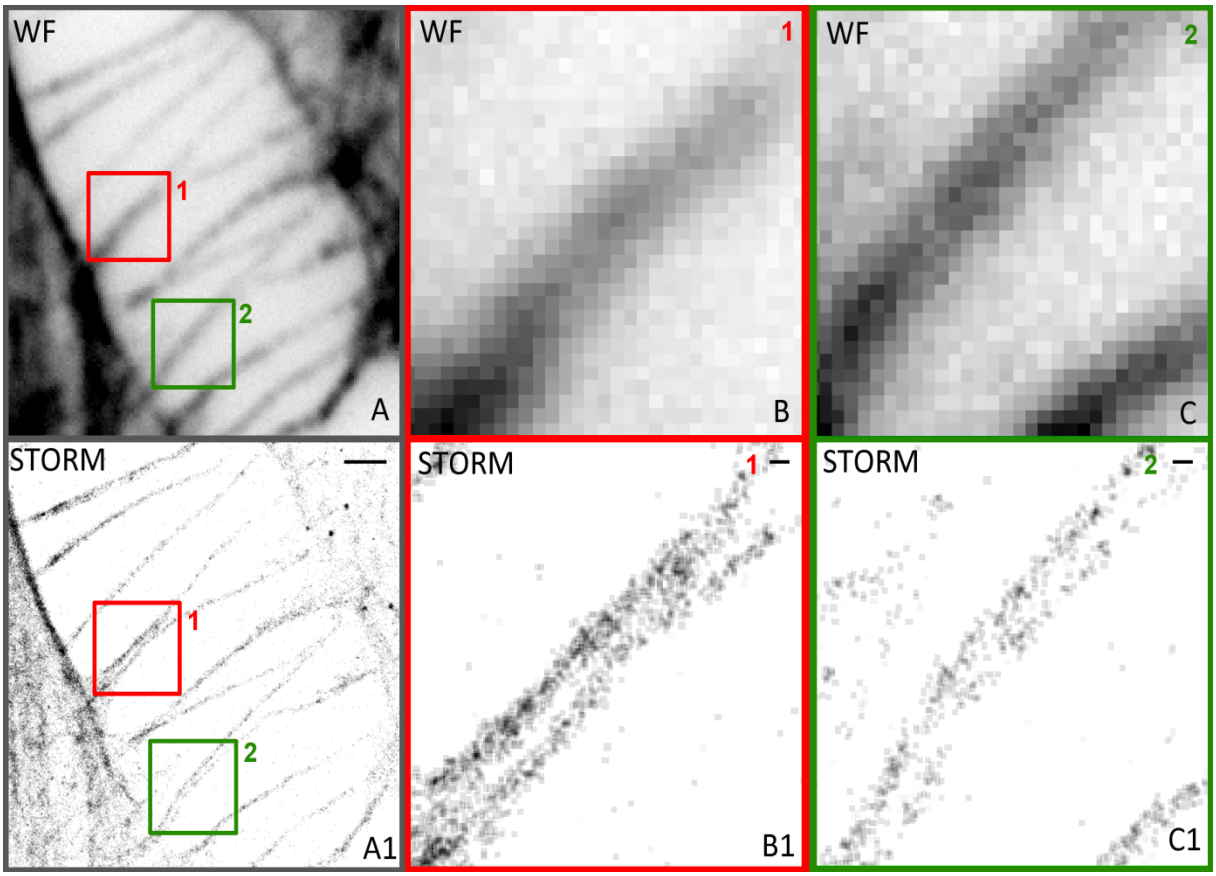

Figure 15. A) A wide-field image of actin filaments labeled with phalloidin Alexa-Fluor-647. **B)** Magnified detail from image A in the red frame 1 .**C)** Magnified detail from image A in the green frame 2. **A1)** *D*STORM reconstruction of the actin filaments from image A. Scale bar 1µm. **B1)** *D*STORM reconstruction of the actin filaments in the red frame 1. Scale bar 100 nm. **C1)** *D*STORM reconstruction of actin filaments in the green frame 2. Scale bar 100 nm.

Analysis of the dimensions and the structure of the kinetochore chromatin

With the application of *d*STORM, I obtained images of the periphery centromere chromatin assembled with CENP-A at the basis of the kinetochore (called kinetochore chromatin) on which it was possible to distinguish its size, shape, and its inner architecture (**Figure 16**, **Figure 17**). By labeling the kinetochore chromatin with fluorescent primary antibodies against CENP-A, I imaged the blinking and reconstructed 97 cells. 58 reconstructed images had more than 70 % kinetochores with distinguishable details in the structure, and I used them to analyze the shape and dimensions of the kinetochore chromatin. There were 1191 kinetochores in total on them, out of which 1093 kinetochores had distinguishable details in the structure. I measured their shape, length, width, and width and distance of their inner structures. Kinetochores which contained blinking longer than 150 ms or were out of focus I characterized as poorly reconstructed. This is because of prolonged blinking and the position outside of the focus cause overlapping of PSFs of individual blinking molecules and imprecise localization.

The kinetochore chromatin labeled with CENP-A is mostly arranged as parallel and vertical chromatin threads that form a compact structure (**Figure 16 D, E, F, Figure 17**, **Figure 18**, **Figure 20**). The resolved structure of the centromere chromatin is not strictly regular, and it is possible to distinguish different forms, mostly rectangles (**Figure 17**). I arranged the resolved kinetochores into groups according to their recognizable shape and inner architecture for further analysis. 82 % of kinetochores were compact, and it was possible to distinguish parallel and vertical threads in their interior (**Figure 17**, **Figure 18**). From now on I called them *compact kinetochores* with parallel threads in their interior. 9.4% of analyzed kinetochores were compact, and it was possible to distinguish details inside of them, but their inner structure was unclear, from now on called *compact kinetochores with undefined inner structure* (**Figure 20**). 82 % of compact kinetochore with parallel threads in their interior was rectangular (**Figure 17**), and 0.7% of them had a triangular shape (**Figure 18**). 5% of kinetochores were of irregular outer shape and consisted of loosely organized threads, from now on called *irregular loose kinetochores* (**Table 27**, **Figure 19**).

The kinetochore chromatin assembly occupied with CENP-A was between 145nm and 648 nm long, 302 nm on average. The kinetochores had a width between 78nm and 357 nm, on average 193 nm. The thicknesses of 1354 threads inside of the kinetochore chromatin were measured. The threads within the kinetochores were between 12 nm and 110 nm thick (**Figure 21**). On some *d*STORM reconstructions of kinetochores, very thin threads of chromatin, thick between 10 and 20 nm, could be recognized (**Figure 23**). In the arrangement of kinetochore chromatin, I measured the distance between the centers of the width of neighboring threads. They were mutually distant between 20 nm and 110 nm, 56 nm on average (**Figure 22**).

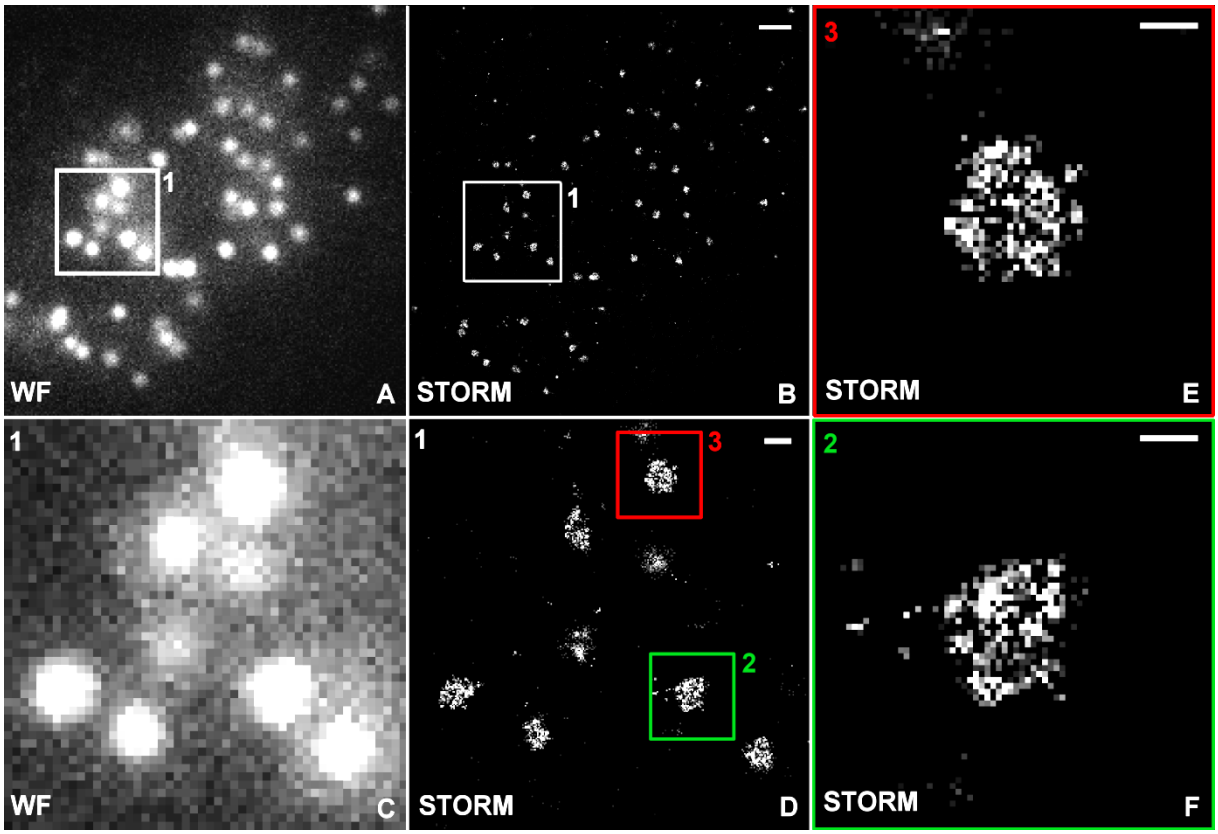

Figure 16. *D*STORM reconstruction of the *interphase* kinetochore chromatin. A) A wide-field image of a nucleus of an *interphase* Hep2 cell with kinetochore chromatin labeled with immunoglobulin antibodies against CENP-A dyed with Alexa-647 **B)** *dSTORM* reconstruction of the cell depicted in A. Scale bar 1µm. **C)** Magnified detail from the white frame 1 from image A, wide-field (WF). **D)** Magnified detail from the white frame 1 from image B, *d*STORM reconstruction. Scale bar 200 nm. **E)** Magnified detail from the red frame 3 from image D, *d*STORM reconstruction. Scale bar 100nm. **F)** Magnified detail from the green frame 2 from image D, *D*STORM reconstruction. Scale bar 100nm.

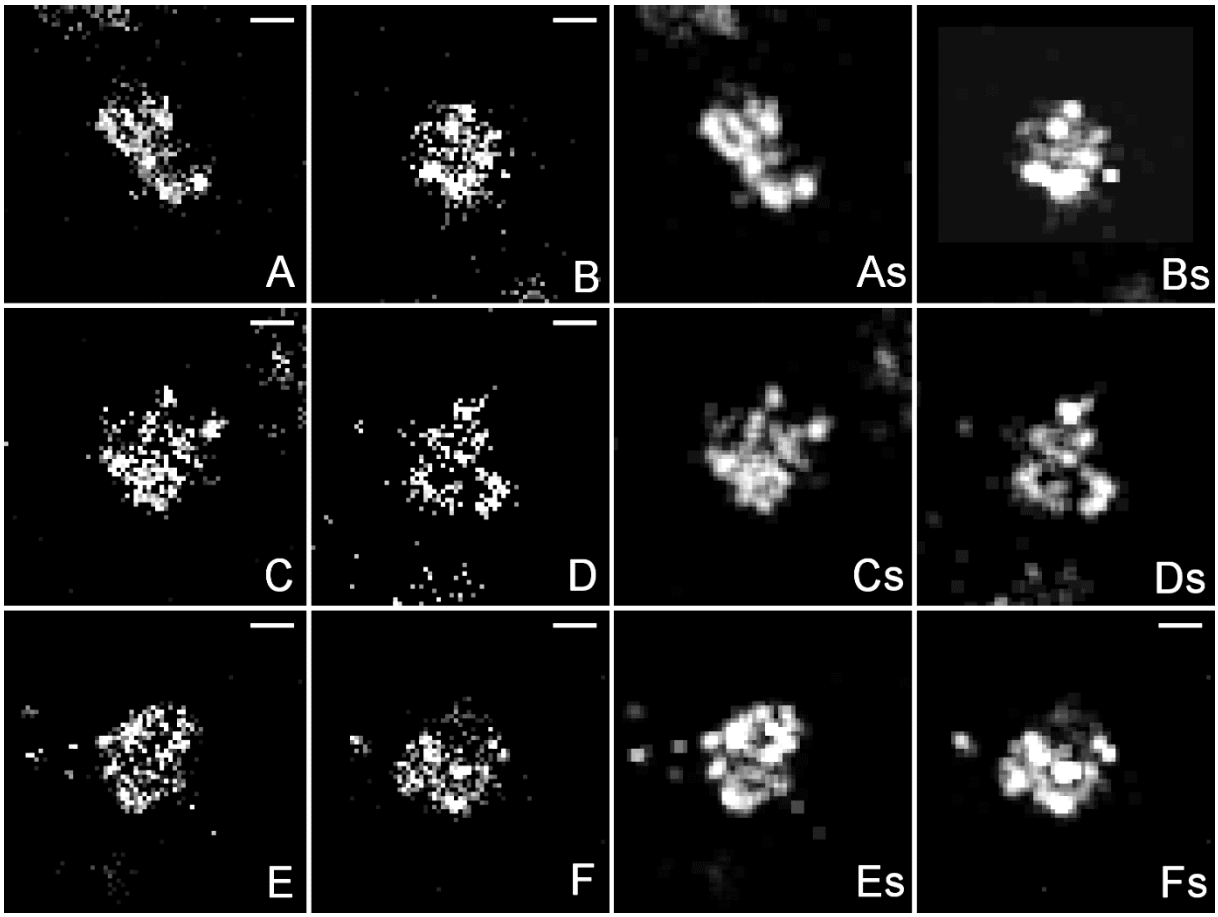

Figure 17. A - F) *D*STORM reconstructions of compact kinetochores with a rectangular shape and composed of parallel and orthogonal lines recognizable in their interior. Scale bar 100 nm. Kinetochore chromatin was labeled with immunoglobulin antibodies against CENP-A dyed with Alexa-647. **As-Fs)** Images A-D processed with a smooth filter. Each pixel is replaced with the average of its 3 × 3 neighborhood.

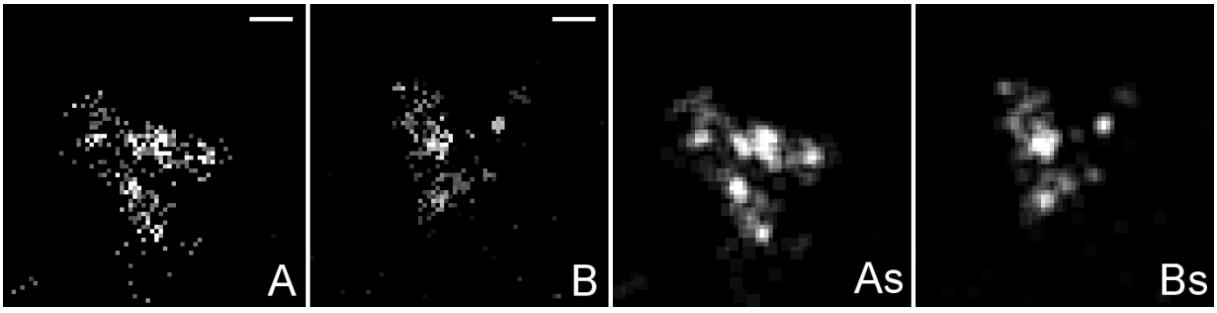

Figure 18. A -B) *DSTORM* reconstructions of the compact kinetochores with a triangular shape and composed of the parallel and orthogonal lines recognized in their interior. Scale bar 100 nm. **As - Bs)** Images A-B are processed with a smooth filter. Each pixel is replaced with the average of its 3 × 3 neighborhood.

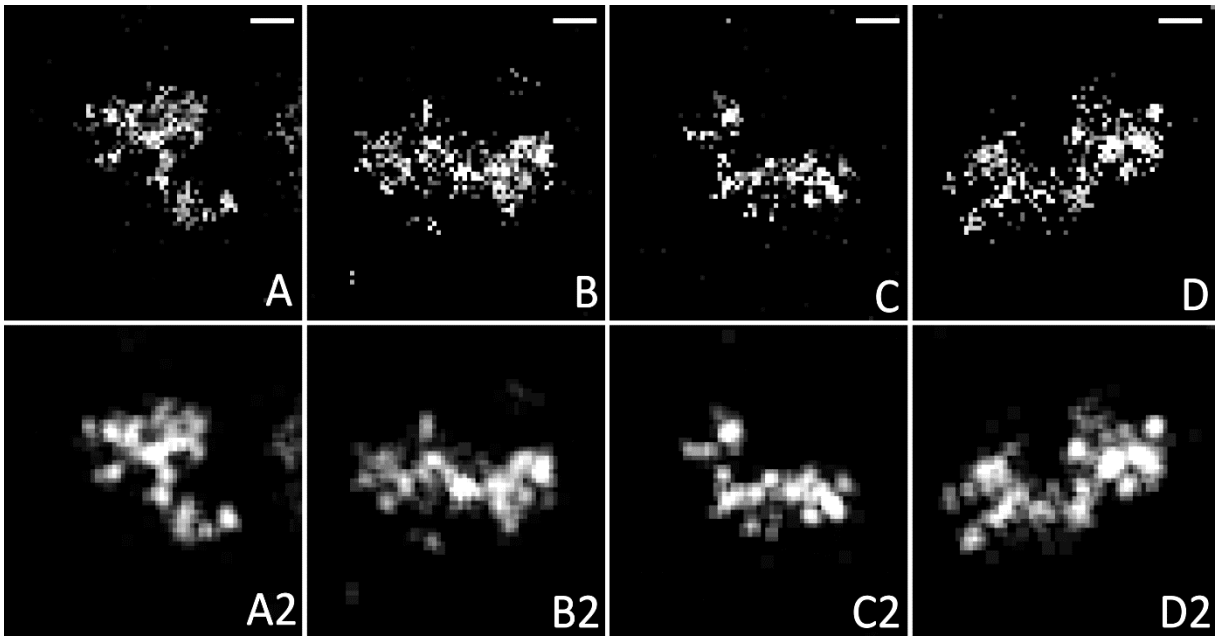

Figure 19. A -D) *D*STORM reconstructions of the kinetochores with irregular outer shape and composed of loose lines (they are called *irregular loose kinetochores* in the text). Scale bars 100 nm. **A2 – D2)** Images A-D are processed with a smooth filter. Each pixel is replaced with the average of its 3 × 3 neighborhood.

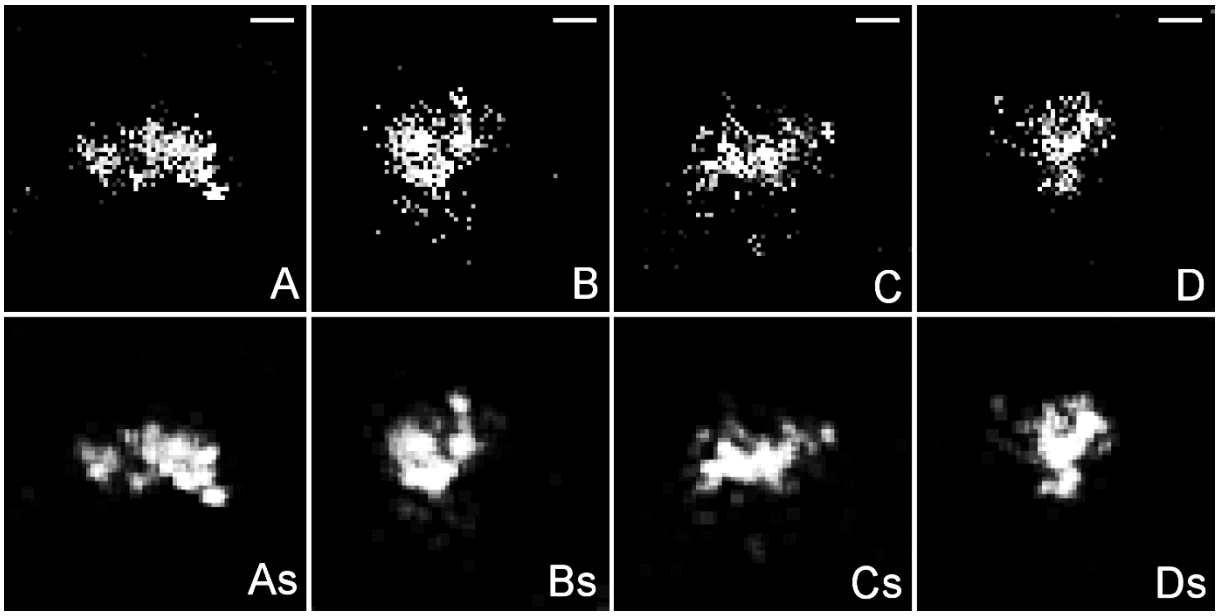

Figure 20. A - D) *D*STORM reconstructions of the compact kinetochores with undefined inner structure. Scale bar 100 nm. **As – Ds)** Image A-D are processed with a smooth filter. Each pixel is replaced with the average of its 3 × 3 neighborhood.

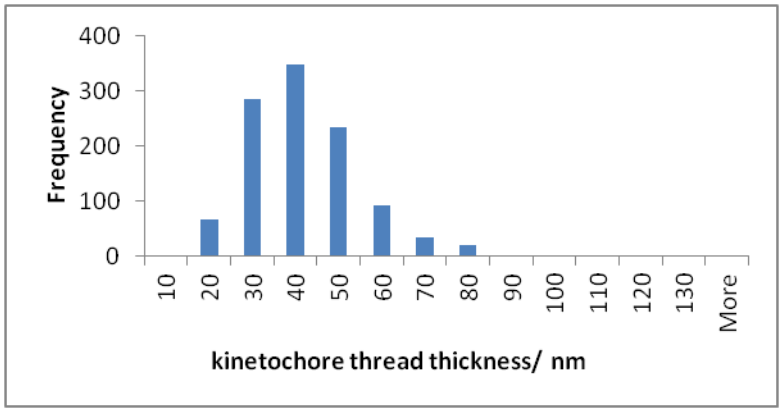

Figure 21. The thickness of the kinetochore threads. The graph shows the distribution of the thickness of threads forming the arrangement of the kinetochore chromatin labeled with CENP-A. The distribution is normal, with a peak of distribution at thicknesses of approximately around 40 nm.

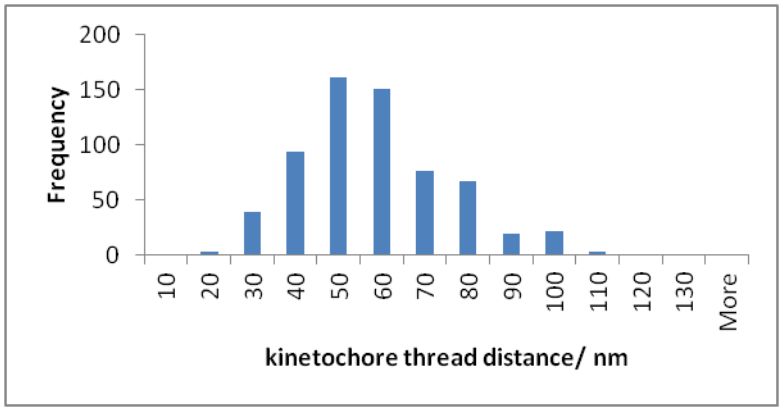

Figure 22. Kinetochore threads distance. The graph shows the distribution of the distance between threads forming the kinetochore chromatin labeled with CENP-A. The portion of threads thicker than 60 nm and thicker than 80 nm gradually decreases. The most of measured distances of threads are around the average value of 56 nm, but the representation histogram does not have a normal distribution despite the high number of measured distances of the kinetochore threads.

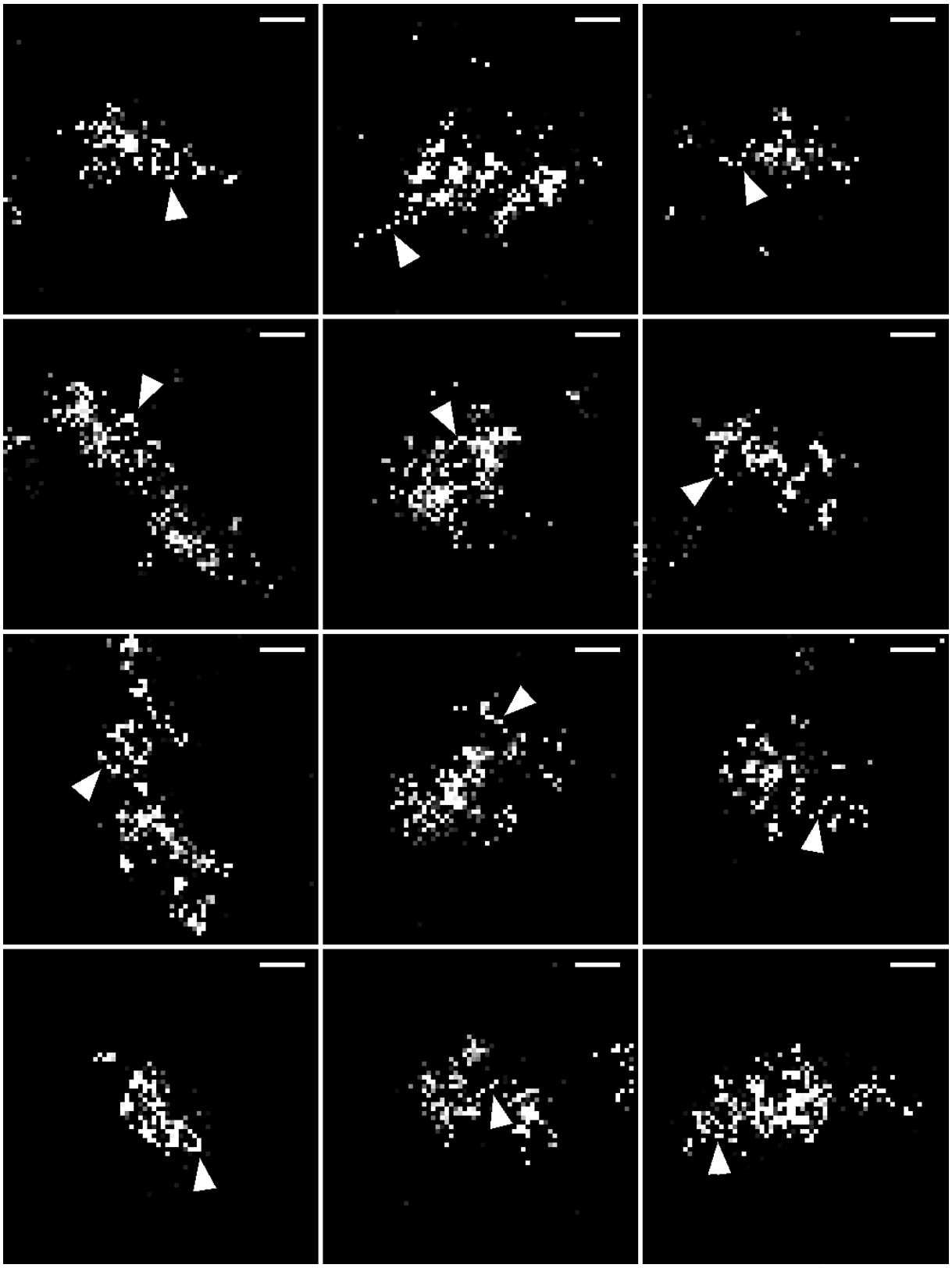

Figure 23. *D*STORM reconstructions of kinetochores with very thin threads. Arrows point to the kinetochore structures between 10 and 20 nm thick. The size of one pixel is 10 nm. Scale bar 100 nm.

The changes in the kinetochore chromatin during the cell cycle

To see whether kinetochore chromatin assembled with CENP-A rearranges during the cell cycle, I arranged the reconstructed cells according to their phases in the cell cycle. I recognized phases of the cell cycle per the arrangement of the kinetochores on wide-field images and the *d*STORM reconstructions. The beginning of prometaphase and the hooking of the kinetochore by microtubules can be recognized from the alignment of sister kinetochores to be orthogonal on the division plane. I measured the standard deviation of angles between widths which connect sister kinetochores. 20 cells had the standard deviation of angles of the widths who connect sister kinetochores under 24 degrees, and I considered them mitotic. 24 cells had the standard deviation of angles over 45 degrees, and I considered them interphase. No cell had the standard deviation of angles between axes that connect the centers of sister kinetochores between 24 and 45 degrees. I arranged interphase cells in phases according to the portion of recognized paired kinetochores in the total number of kinetochores on *d*STORM and wide-field micrographs. I grouped the cells with more than 40 % of paired kinetochores into the G2 phase

The shape of the arrangement of kinetochore chromatin was similar in interphase and mitotic cells (**Table 27**, Supplementary data), but the *mitotic* kinetochores were more elongated in the direction of the equatorial division plane (**Figure 24**, **Figure 25**).

To examine the dimensions of *interphase* kinetochores concerning the direction of chromosomes, I separately measured them on paired kinetochores in cells in the G2 phase (**Table 17**, **Figure 26**, **Figure 27**). I measured the length of the kinetochore chromatin in regards to the length between sister kinetochores. I defined their width as the side of kinetochore chromatin rectangle parallel or under a smaller angle in regards to the length between sister-kinetochores. The mitotic kinetochores were then on average 111 nm longer, i.e., 48,8% longer than interphase kinetochores and 61 nm i.e., 26% narrower than interphase kinetochores (**Table 17**). Since measured values of the kinetochore width and length and the thickness of the kinetochore fibers (**Figures 26, 27, and 30**) have a normal distribution, I compared the change of those properties during the cell cycle by using T-test. The change of width and length between kinetochores in the *G2* phase and *mitotic* kinetochores was statistically significant (Two-tailed T- test P = $1.55e^{-18}$ (kinetochore length *G2-mitosis*), P = $3.77e^{-17}$ (kinetochore width *G2-mitosis*).

T-test, or students test, tests if the means of the two sets of data are significantly different from each other. It tests if the two groups of measurements come from a different sample. It establishes the null hypothesis that the means of the two samples are equal. T-test calculates P-values from the mean difference of the group, the standard deviation of each group, and the number of measurements of each group. If calculated P-values are small, the null hypothesis is qualified to be rejected, and it indicates that the data difference between two sets of measurements is real and not by chance. Calculated P-values are compared with calculated P values of test samples, where two groups of samples have the same mean and the difference between them is only a coincidence. In biology, if the P-value is smaller than 0.05, the null hypothesis is rejected, the difference between samples is not a coincidence, and the difference between the means of two samples is considered significant.

The shape of the arrangement of the kinetochore chromatin was similar in interphase and mitotic cells, but the arrangement in mitotic cells was narrower and longer than the arrangement in interphase cells (**Figure 26**, **Figure 27**).

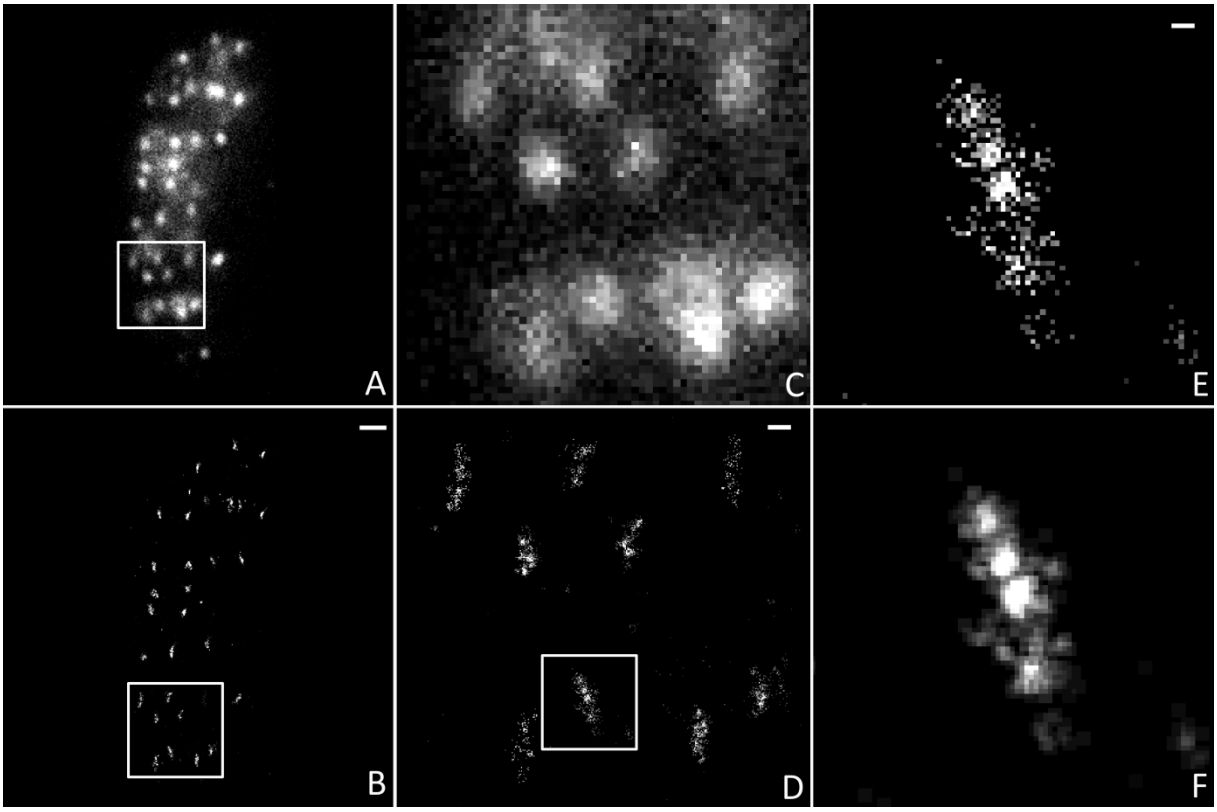

Figure 24. Kinetochore chromatin during mitosis. A) Wide-field microscopic image of the kinetochore chromatin labeled with immunoglobulin antibodies stained with Alexa-Fluor 647 in mitotic Hep2 cell. The image is captured on a stable TIRF/HILO *d*STORM microscope. **B)** *D*STORM reconstruction of the same cell. Scale bar 1 μm. **C)** Magnified detail from the frame in Image A, wide-field. **D)** Magnified detail from the frame in image B, *d*STORM. Scale bar 200 nm. **E)** Magnified kinetochore from the frame in image D, *d*STORM. Scale bar 100 nm. **F)** Image E processed with a smooth filter. Each pixel is replaced with the average of its 3 × 3 neighborhood.

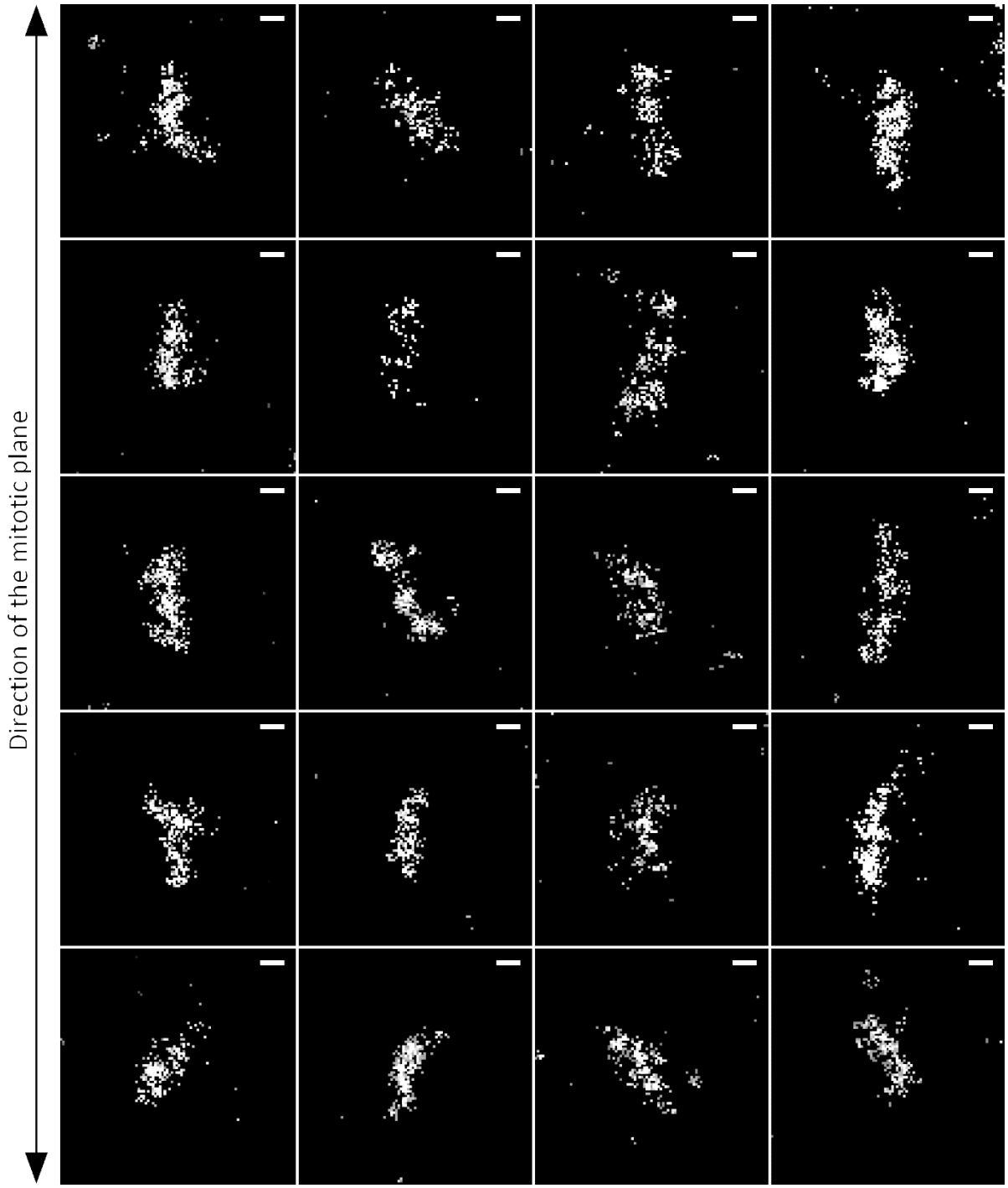

Figure 25. Kinetochore chromatin during mitosis. This figure shows merged images of the individual kinetochores in mitosis. Images of individual kinetochores were rotated so that the line of alignment of kinetochores in their cell was kept vertical in the merged image. Mitotic kinetochores are mostly elongated in the direction of the line of the kinetochore alignment. Scale bars 100 nm.

Table 17. Outer dimensions of kinetochore chromatin assembled with CENP-A. This table shows the average length of kinetochores (average kinetochore length), the average width of kinetochores (average kinetochore width), and the average of the ratio between width and length (average kinetochore width/length ratio) in mitotic cells, in all interphase cells, and the cells in the G2 phase. In G2 and mitotic kinetochores, the width is defined as concerning the axis between sister kinetochores. * Standard error of the mean.

Kinetochore dimensions	mitosis	interphase	G2
Average kinetochore length	339 nm +/- 4 nm *	271 nm +/- 2.6 nm *	227 nm +/- 5 nm *
Average kinetochore width	174 nm +/- 2 nm *	209 nm +/- 1 nm *	234 nm +/- 3 nm *
Average kinetochore width/length ratio	0.5	0.8	1
Number of cells	20	24	12
Number of analyzed kinetochores	358	574	247

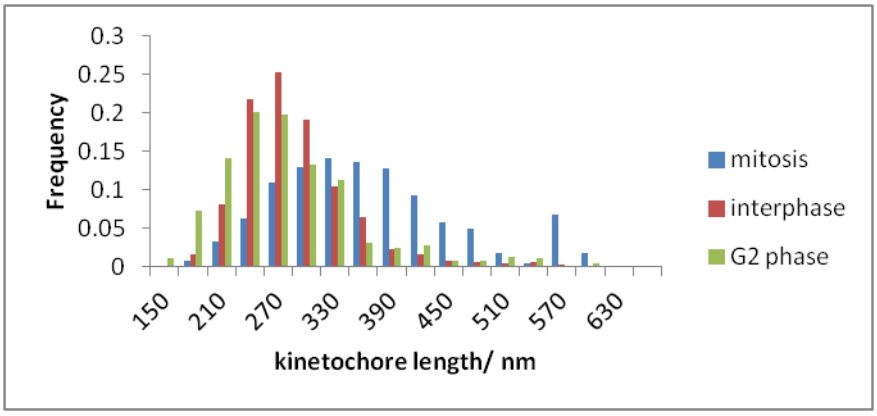

Figure 26. Kinetochore length during the cell cycle. This graph shows the distribution of length of the kinetochore chromatin assembly occupied by CENP-A in mitosis, in interphase, and the G2 phase. The length of the kinetochore chromatin was measured on the *d*STORM reconstructions.

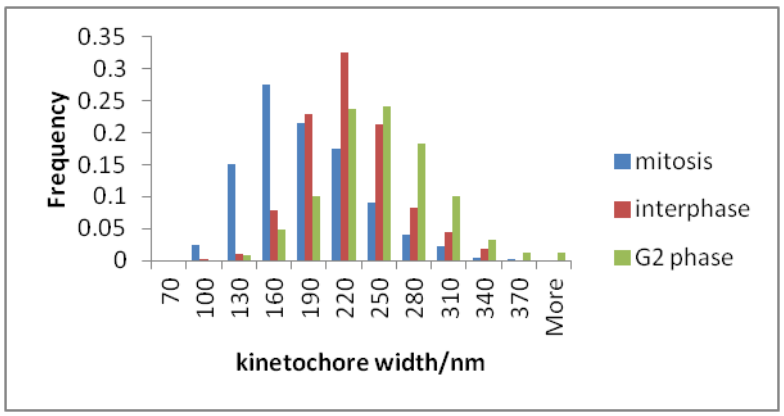

Figure 27. Kinetochore width during the cell cycle. This graph shows the distribution of width of the kinetochore chromatin assembly occupied by CENP-A in mitosis, in interphase, and the G2 phase. The width of the kinetochore chromatin is measured on *d*STORM reconstructions. The distribution is normal, but the maximum of the distribution of the width of kinetochore chromatin in mitosis is shifted toward lower values. In the G2 and the mitotic kinetochores, the width was defined concerning the axis between sister-kinetochores.

Properties of the kinetochore chromatin in mitosis

Outer dimensions of the kinetochore chromatin in mitosis

To examine whether the elongation and the narrowing of the kinetochore chromatin in mitosis correlate with the pulling of the kinetochores by the microtubules of the spindle apparatus, I compared the average cell ratio of the width and the length of the kinetochore chromatin, labeled with CENP-A, with the average cell distance between sister-chromatids (**Figure 28**). In mitotic cells average cell ratio of kinetochore width and length decreased with the average distance between sister-kinetochores until they were around 1150 nm distant. With further increase of the average distance of sister kinetochores of mitotic cells, the average value of kinetochore width and length increased. Among interphase cells, there was no correlation between the average ratio of width and length of the kinetochore chromatin and between the distance between sister kinetochores (**Figure 28**).

To estimate if the progress of mitosis is connected with changes of kinetochore dimensions, and with the distancing of sister kinetochores, for every mitotic cell, I measured the magnitude of four indicators. As indicators of the progress of mitosis, I measured the standard deviation of angles of lengths between sister kinetochores, the maximal ratio of kinetochores whose length between sister kinetochores intersects a line parallel to the division plane, width of the space with kinetochores orthogonal to the division plane, and the average distance of the middle of the length between sister kinetochores from the division plane (**Figure 9**). The distribution of cells with measured values of every indicator of metaphase I displayed graphically (Supplementary data, **Figure 45-Figure 48**). Measured values represented with the number of cells two or more times smaller than the measured value represented with the biggest number of cells, I considered as limit values. (Supplementary data: **Figure 45** - **Figure 48**). To the cells with limit values typical for late mitosis, I assigned a point. To the cells with limit values typical for the early stages of mitosis, I assigned a negative point. For every cell, I added the points assigned for all three indicators of the progress of mitosis (**Table 28**, Supplementary data).

I compared the sum of points of the three indicators of the progress of mitosis with the kinetochore chromatin width and length ratio and with the distance between sister kinetochores in Figure 29. In *Early prometaphase* cells with sister kinetochores separated between 880 and 1020 nm, the kinetochore width and length ratio were between around 0.7 and 0.5. In *Late prometaphase* cells with sister-kinetochores separated between 1020 and 1150 nm, the kinetochore with and length ratio was between around 0.45 and 0.5. Only cells with kinetochores separated by 1150 nm or more have positive values of metaphase indicators. Most of the *metaphase* cells with sister-kinetochores separated 1150 nm or more, have the ratio of kinetochore width and length bigger than 0.5. Unlike the average cell ratio of kinetochore width and length, the ratio of width and length of individual kinetochores did not change regularly with the distance of sister kinetochores.

Two cells at the beginning of prometaphase deviated in terms of the change of kinetochore width and length ratio concerning the distancing of the sister kinetochores (**Figure 29, Figure 49**). They did not have kinetochores aligned in the division plane. They were recognized as mitotic according to the standard deviation of angles of lengths connecting sister kinetochores (**Table 28**).

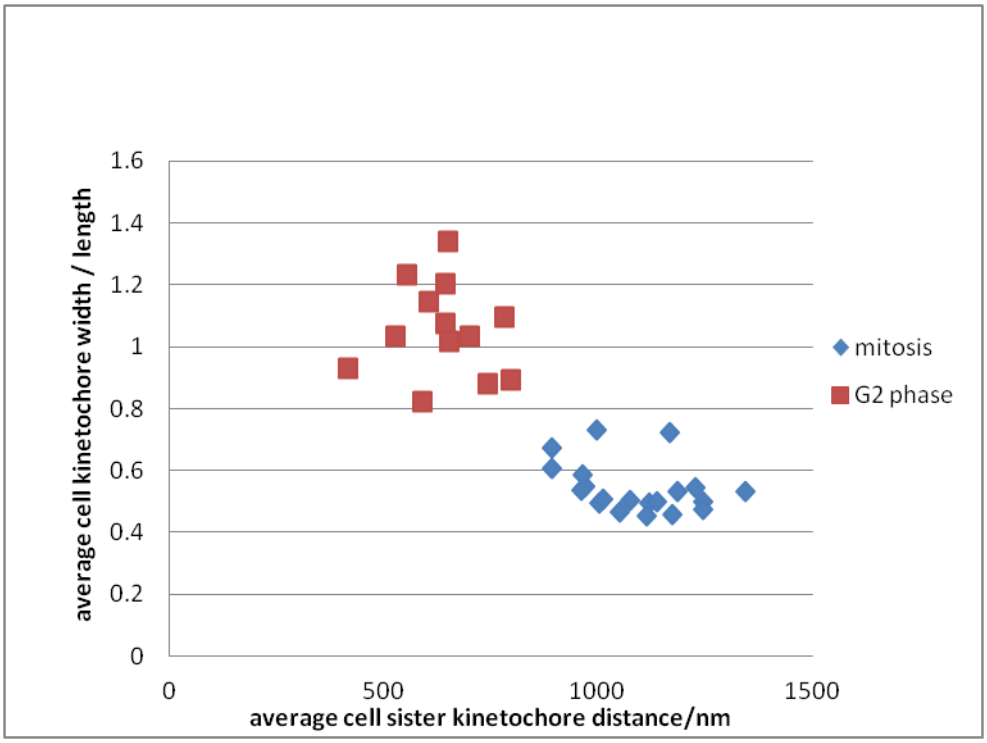

Figure 28. Change of the kinetochore dimensions with respect to the stretching of centromeres. The graph shows the relationship between the ratio of kinetochore width and length (average cell kinetochore width/length) and distances between sister-kinetochores (average cell sister kinetochore distance) in the interphase G2 cells (G2 phase) and the mitotic cells (mitosis). The average of the ratios of kinetochore widths and lengths was calculated for each cell. This value was compared to the average distance between sister kinetochores. Every point represents one cell. The identification of sister-kinetochores is depicted **in Figure 10**.

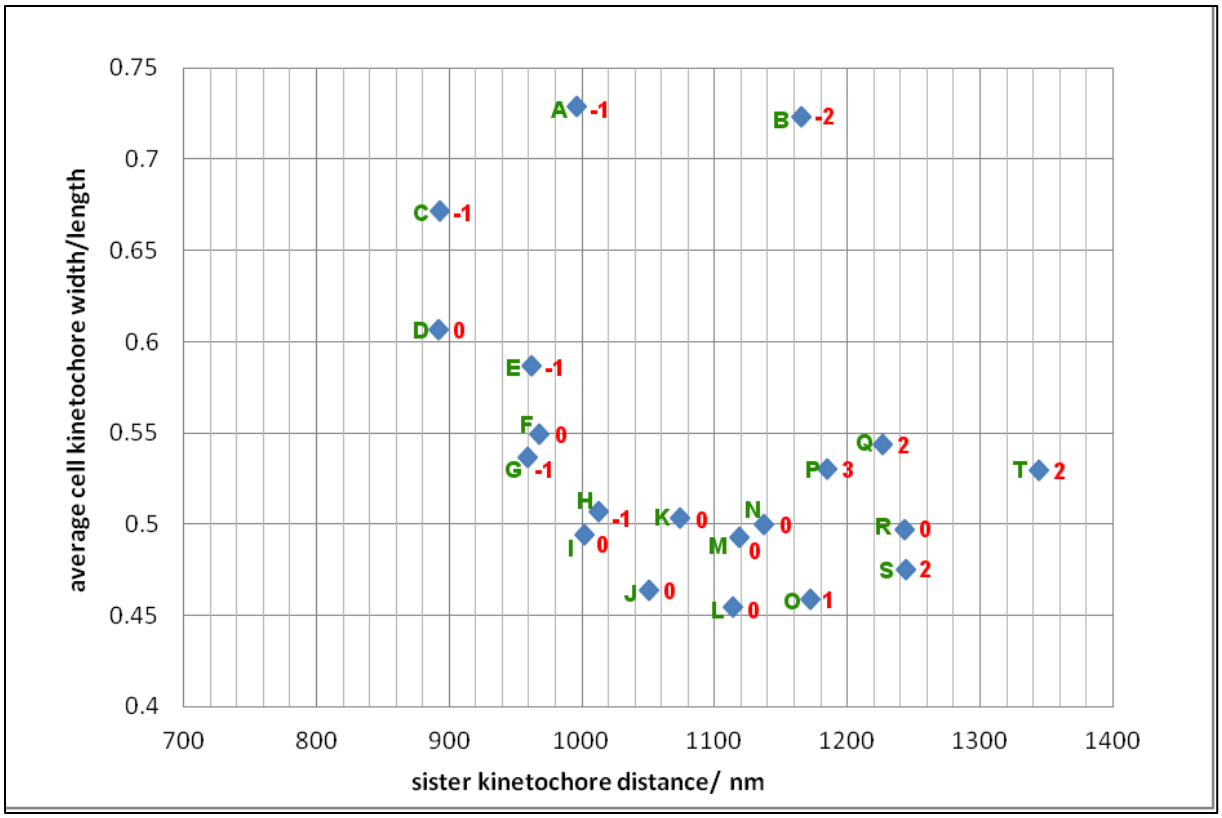

Figure 29. Change of the kinetochore dimensions with the progress of mitosis. The graph shows the change in the average ratio of the kinetochore width and length (average cell kinetochore width/length) with the average cell distance between sister kinetochores (sister kinetochore distance). Every dot represents the average values of one cell. Near the values that represent the values of kinetochore dimensions, are values of the sum of the attributed values of metaphase indicators (from **Table 28**) (red). A small average interkinetochore distance and the big kinetochore width and length ratio are characteristic for cells that have the sum of the metaphase indicators negative. Big interkinetochore distances (sister kinetochore distance) are characteristic for cells that have the sum of the metaphase indicators positive. Most of the cells are found at a sum of the metaphase indicators around zero. Their average kinetochore with and length ratio is smaller than the width and length ratio in cells with the positive sum of the metaphase indicators. Letters A-T mark individual cells whose values of the progress of mitosis are shown in **Table 28**.

The dimension of the structures inside of the mitotic kinetochore chromatin

To follow the changes in the inner structure of the kinetochore during mitosis, I measured the thickness of threads within the arrangement of the kinetochore chromatin and the distances between the centers of neighboring kinetochore threads. I compared the average thickness and the distance of kinetochore threads in *prometaphase* and *metaphase* cells and discovered subtle changes of the inner dimension of the kinetochore during mitosis (**Table 18**). The threads inside of Kinetochores in *prophase* cells were on average 3.2 nm thicker than the threads inside of kinetochores in the cells in the *G2 phase*. The difference in the thickness of the threads inside of the *G2 phase* kinetochores and the threads inside of the *prometaphase* kinetochores was significant (two-tail t-test P =0.006965 (kinetochore thread thickness G2-prometaphase)). Threads inside of the kinetochores in the *metaphase* cells were on average 2.7 nm thinner than the threads inside of the kinetochores in the *prometaphase* cells (**Table 18**), which was also statistically significant (t-test

P = 0.012005 (kinetochore thread thickness prometaphase-metaphase). The difference in the thickness of chromatin threads inside of the kinetochores in the *G2 phase* and the thickness of chromatin threads inside of the kinetochores in the *metaphase* cells was not statistically significant (two-tail t-test P=0.800994 (kinetochore thread thickness G2-metaphase). The distribution of width of kinetochore threads of *G2 phase* cells was more alike the distribution of the width of *metaphase* kinetochore threads than the distribution of the width of prophase kinetochore threads (**Figure 30**).

The average distance between the centers of neighboring kinetochore chromatin threads of *prometaphase* cells was 5.3 nm larger than the distances between the centers of the kinetochore chromatin threads of the kinetochores in the *G2 phase* (**Table 18**). The average distance between the centers of metaphase kinetochore threads was 4.8 nm smaller than the distance of *prometaphase* kinetochore treads. Since the distance between kinetochore threads in the G2 phase and mitosis did not have a normal distribution, I did not test if the samples were different statistically

Table 18. Comparison of the thickness of the lines inside kinetochores and the distance between neighbor kinetochore chromatin lines during transit through mitosis. The table shows the average thickness of lines inside the kinetochore (average thickness of kinetochore lines) and its average distance (average between centers of kinetochore lines) in nanometres in the G2 phase, prometaphase, and the metaphase. Statistically insignificantly different values in the same column are shown in the same color. * Standard error of the mean.

	Average thickness of kinetochore lines	Average distance between centers of kinetochore lines	Number of measured kinetochore lines
G2 phase	37 nm +/- 0.8 nm *	54 nm +/-2 nm *	245
prometaphase	41 nm +/- 0.8 nm *	59 nm +/-1 nm *	280
metaphase	38 nm +/-0.8 nm *	55 nm +/-2 nm *	287

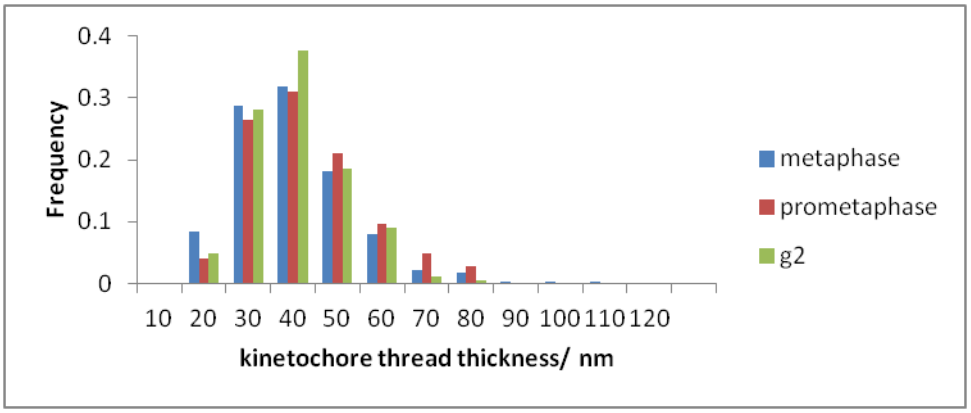

Figure 30. Thickness of kinetochore threads in mitosis. This graph shows the distribution of thickness of threads inside of a kinetochore chromatin assembly in *metaphase*, *prometaphase,* and *G2 phase* (g2). Distribution of the thickness of the kinetochore threads in prometaphase and metaphase are normal and inclined towards values lower than the average with a peak around 40 nm. *Metaphase* cells are defined as cells that have an average distance between sister-kinetochores bigger above 1140 nm. *Prometaphase* cells are defined as cells that have an average sister-kinetochore distance below 1140 nm.

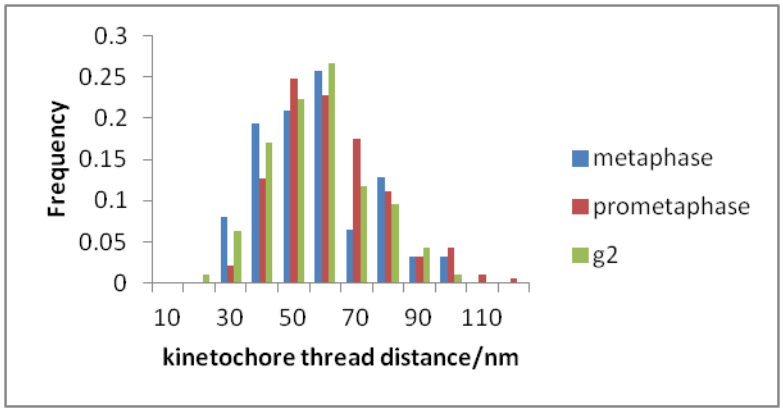

Figure 31. Distances between kinetochore threads in mitosis. This graph shows the distribution of the distances between neighboring threads inside of the kinetochore chromatin assembly in *metaphase*, *prometaphase,* and *G2 phase* (g2). *Metaphase* cells are defined as cells that have an average distance between sister-kinetochores above 1140 nm. *Prometaphase* cells are defined as cells that have an average sister-kinetochore distance below 1140 nm.

Properties of the kinetochore chromatin assembly in interphase

I grouped the interphase cells into the G1 phase or the G2 phase according to the portion of recognized paired kinetochores in the total number of kinetochores on the *dSTORM* and the wide field micrographs. In 12 *interphase* cells, I recognized more than 40 % of paired kinetochores, and I grouped them in the *G2 phase*. In 5 interphase cells, I recognized less than 20 % paired kinetochores, and I grouped them into the *G1 phase*. In 7 cells, I recognized between 20% and 40 % paired kinetochores, and I measured and analyzed their dimensions as interphase cells.

Four *interphase* cells had a large portion of kinetochores, which were longer than 370 nm, several double kinetochores, and several atypical gigantic kinetochores longer than 500 nm (**Figure 32**, **Table 19**). The double kinetochores looked like two typical kinetochores attached. The gigantic kinetochores had the elements of the usual kinetochore architecture. Inside of the gigantic kinetochores, I recognized parallel threads in their parts, but the threads were mostly uncoiled and broadly arranged (**Figure 32**). In the rest of the interphase cells, I found only four double kinetochores, each in another cell. I found the gigantic kinetochores only in the cells with double kinetochores and an increased portion of kinetochores longer than 370 nm. I assumed that the elongation of kinetochores and uncoiled gigantic kinetochores were a consequence of chromatin unfolding due to the DNA replication. Based on the *d*STORM images I grouped the cells which had 15 % of kinetochores longer than 370 nm and at least two gigantic or at least three double kinetochores into the *S phase*.

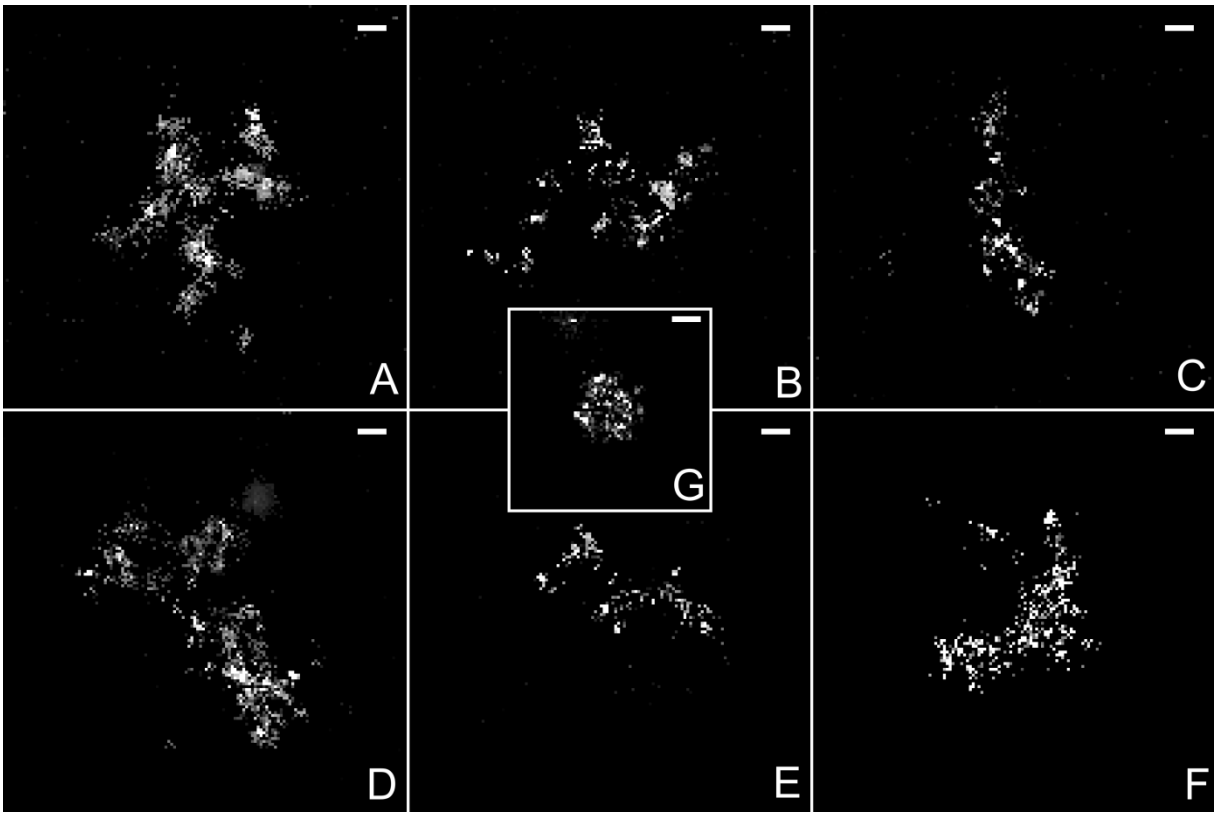

Figure 32. Gigantic kinetochores (A-F) in comparison to a typical *interphase* kinetochore **(G)**. Scale Bar 100 nm.

Table 19. Comparison of the characteristics typical for cells grouped into the *S phase* with a proportion of the same characteristics in cells in the G1 and G2 phases. The table shows the portion of the kinetochores longer than 370 nm (>370 nm) in the total number of properly reconstructed kinetochores (good kinetochores), the number of gigantic unfolded kinetochores longer than 500 nm (gigantic), and the number of the double kinetochores (double) in four cells grouped in the *S phase* (21.1. d2, 21.1. i, 22.1. x, 30.5. j). The mentioned characteristics were compared in the *S* (all S), the *G1* (all G1), and *the G2 phase* (all G2).

cell	>370nm	gigantic	double	good kinetochores
21.1. d2	28%	4	7	35
21.1. i	13%	1	4	37
22.1. x	15%	1	6	33
30.5. j	31%	2	2	35
All S	27.1%	6	19	118
All G1	2.5%	0	2	94
All G2	9.2%	0	2	245

Outer dimensions of the interphase kinetochore chromatin

The assembly of the kinetochore chromatin in the *G1 phase* was the most compact, and in the *S phase* was the widest concerning the sub-phases of the interphase (**Table 20**). The kinetochores in the *S phase* were, on average 17 nm wider than the kinetochores in the G1 phase and 9 nm wider than those in the G2 phase. The difference in the width between the kinetochore chromatin assembly in the G1 and the S phase was significant (Two-tail t-test P (kinetochore width G1-S) =0.01916. The difference in the width between the kinetochore chromatin assembly in the G2 phase and the S phase was significant as well (P (kinetochore width G2-S) = 0.035094). The assembly of the kinetochore chromatin in the G1 and the G2 phase did not significantly differ in width. (Two-tail t-test P (kinetochore width G1-G2) =0.552201) The lengths of kinetochores in the phases G1, S, and G2 did not significantly differ. The distribution of the width and the length of the kinetochore chromatin occupied with CENP-A are normal in the G1, S, and G2 phases (**Figure 33**, **Figure 34**).

Table 20. The average outer dimension of the kinetochore chromatin assembly in the G1, G2, and S. The table shows the average width (kinetochore width) and length (kinetochore length) of the kinetochore chromatin assembly occupied with CENP-A in nanometres in phases G1, S, and G2. * Standard error of the mean.

Phase	Kinetochore width	Kinetochore length	Number of measured kinetochores
G1	206 nm +/- 4 nm *	276 nm +/- 8 nm *	94
S	223 nm +/- 5 nm *	285 nm +/- 6 nm *	118
G2	214 nm +/- 3 nm *	281 nm +/- 3 nm*	245

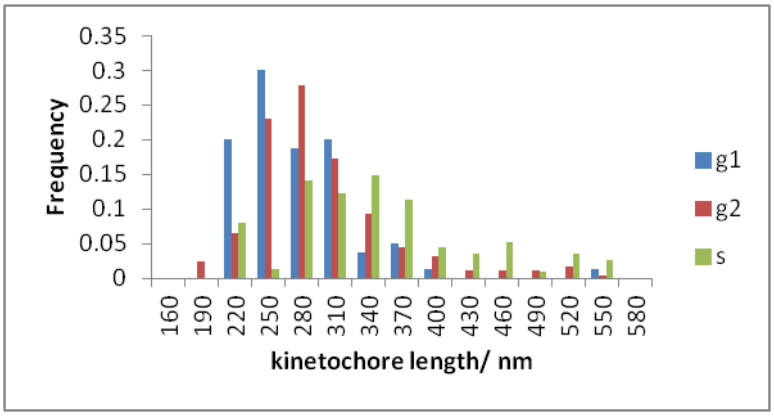

Figure 33. Distribution of the length of the kinetochore chromatin assembly in *G1*, *S*, and *G2 phases.*

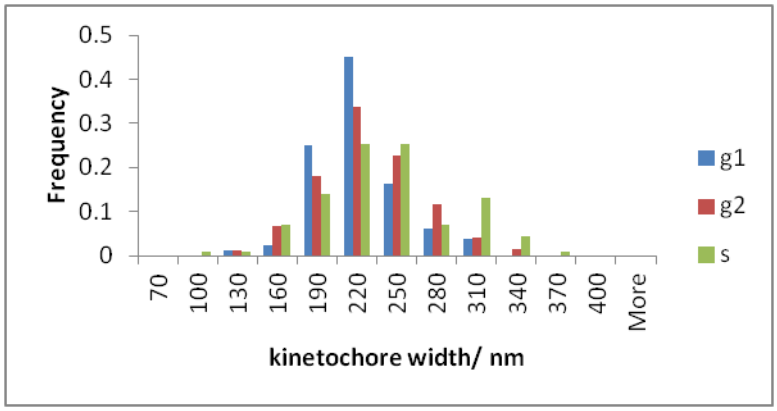

Figure 34. Distribution of the width of the kinetochore chromatin assembly in *G1*, *S*, and *G2 phases*. The distributions roughly coincide with the peak around the average width of about 220 nm. The distribution of the width of the kinetochores in the *S phase* has a less pronounced peak than the distributions of width in the phases G1 and G2; it is somewhere around the average width of 220 and 250 nm (**Table 17**).

Dimensions of the structures forming the kinetochore chromatin in interphase

During the transit of the cell through the interphase, the inner structure of the most of the kinetochores remains similar with recognizable parallel and orthogonal lines in the interior, even in the gigantic and loose kinetochores in the S phase (**Figure 16**, **Figure 17**, **Figure 18**, **Figure 19**, and **Figure 32**). There is no significant difference in the representation of different forms of the kinetochore between phases G1 and G2 (**Table 21**). The cells in the S phase, besides a bigger portion of gigantic and double kinetochores, have 4.4% more of irregular loose kinetochores with parallel and vertical threads than the cells in the *G2 phase*, and 15.3% more of the double kinetochores (**Table 21**).

Table 21. Representation of the different forms of the kinetochore chromatin assembly in G1, S, and G2 phases. The table shows the portion of compact rectangular kinetochores with parallel and/or vertical threads (compact rectangles with lines), irregular loose kinetochores with parallel and vertical threads inside (irregular loose), compact triangular kinetochores with parallel and/or vertical threads (compact triangles with lines), rectangular kinetochores with undefined inner architecture (rectangular without lines), Gigantic kinetochores, and the double kinetochores in cells in the G1 phase, in the S phase, the G2 phase, and in the cells of an undefined phase of interphase.

Form of the kinetochore	G1	S	G2	Undefined
Compact rectangles with lines	86.0 %	60 %	88.1 %	93.2 %
Irregular loose	1.0 %	7.6 %	3.2 %	1.0 %
Compact triangles with lines	1.0 %	0 %	0.8 %	0.6 %
Compact without lines	12.7 %	11.0 %	9.5%	7.9 %
Gigantic	0 %	5.0 %	0 %	0%
double	0 %	16.1 %	0.8 %	0%

The kinetochores in phases *G1, S,* and *G2* consisted of kinetochore threads of a thickness between 15nm and 80 nm (**Figure 35**). The average thickness of kinetochore threads in the *G1 phase* was around 44.9 nm. The average thickness in the *S phase* statistically significantly decreased by 7.5 nm, (**Table 22**) (Two tail t-test P =3.26e^{-6} (kinetochore threads thickness G1-S). The kinetochore chromatin fibers in *G2 phase* were just as thick as those in *S phase* and their difference was statistically insignificant (Two-tail T- test P) =0.730582 (kinetochore threads thickness G1-G2), but the difference in the thickness between kinetochore threads in phases *G1 and G2* was statistically significant (Two-tail T- test P=1.11e^{-05} (kinetochore threads thickness G1-G2)). On *d*STORM reconstructions of cells in phases *S,* and *G2* it was possible to find threads thinner than 20 nm (**Figure 23**). In cells in the *S phase* there were 12 % threads thinner than 20 nm and in the *G2 phase* 4% of threads thinner than 20 nm. In the kinetochores in the cells in the *G1 phase,* I did not find kinetochore fibers thinner than 20 nm (**Figure 35**).

The kinetochore threads in phases *G1*, *S,* and *G2* were 15 nm to 95 nm apart from each other (**Figure 36**). The average distance of kinetochore threads in the *G1 phase* of 55.4 nm is by 6.4 nm bigger than the average distance of kinetochore threads in the *S phase* **(Table 22)**. The *d*STORM reconstructions of cells in the *S phase and G2 phase* contained the fibers whose centers were less than 20 apart from each other (**Figure 36**). Since the values of the distance between kinetochore threads in the G1 phase, the S phase, and the G2 phase did not have a normal distribution (**Figure 36**), I did not compare the difference between distances of kinetochore threads statistically.

Table 22. Average thickness and the distance of kinetochore threads in different sub-stages of the interphase The table shows the average thickness of threads inside the kinetochore in nanometres (Kinetochore thread width/nm) in *G1, S, and G2 phases*, their standard deviations (SD kinetochore thread width) and the average distance between centers of kinetochore threads in nanometres (Kinetochore thread distance/nm) and its standard deviation (SD kinetochore thread distance. * Standard error of the mean.

Phase	Kinetochore thread width	SD kinetochore thread width	Kinetochore thread distance	SD kinetochore thread distance	Number of measured kinetochore lines
G1	45nm +/-1.2 nm *	12 nm	55 nm +/- 1.6 nm *	12 nm	89
S	37 nm +/- 8 nm *	11 nm	49 +/- 1.7 nm *	17 nm	174
G2	37 nm +/- 8 nm *	11 nm	54 nm +/- 2 nm *	16 nm	166

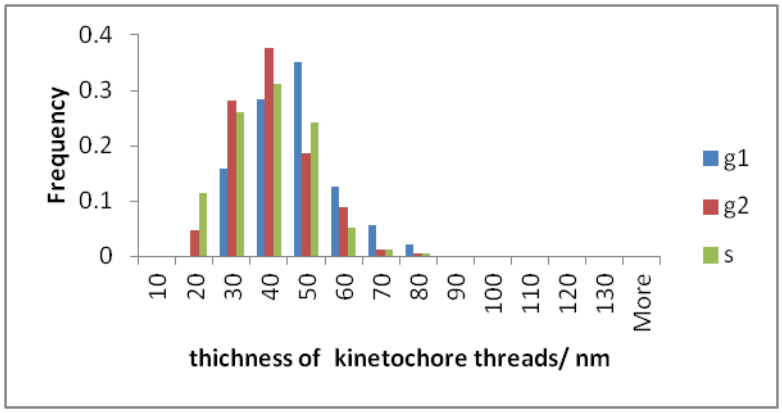

Figure 35. The thickness of the kinetochore threads in the interphase. This graph shows the distribution of the thickness of kinetochore threads in phases G1, S, and G2. The thickness of threads was measured on *d*STORM reconstructions. In the *S* and *G2 phases,* fibers thinner than 20 nm were found. The portion of fibers between 20 and 30 nm thick was higher in phases *G2* and *S* than in G1. The distributions of the thickness of threads in phases G2 and S are similar to the thickness in the G1 phase.

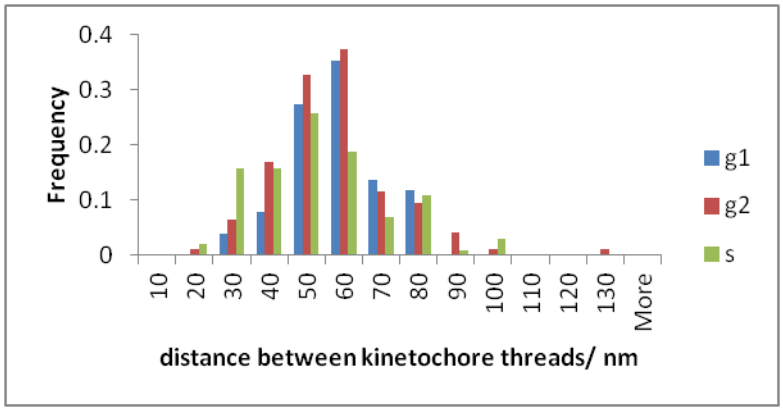

Figure 36. Distance between threads inside of the kinetochore chromatin in the interphase. This graph shows the distances between the centers of neighboring threads inside the kinetochore, measured on *d*STORM reconstruction. Distances in phases *G1* and *G2* are similar to those between kinetochore threads in the *S phase*.

The influence of nocodazole on the kinetochore chromatin

The mitotic toxin nocodazole changes the architecture of kinetochores and increases the frequency of merotelic attachments (Hoffmann et al. 2001, Ladrach and Lafontaine 1986.). For this reason, I examined the influence of nocodazole on the dimensions, shape, and inner structure of the kinetochore chromatin. I made *d*STORM reconstructions of 8 cells treated with nocodazole with a total of 254 validly reconstructed kinetochores.

Compared to the untreated kinetochore, the kinetochore chromatin treated with nocodazole appeared elongated, disorganized, and of more irregular outer shape (**Figure 37**, **Figure 38**)). It was, on average 37 % longer and 41% wider than in the untreated kinetochore chromatin (**Table 23**, **Figure 39**, and **Figure 40**). The difference in the kinetochore width of untreated and treated cells is statistically significant, P =2.61e^{-58} (kinetochore width nocodazole-untreated)). The length of kinetochores in cells treated with nocodazole did not have a normal distribution. For this, I did not statistically test the difference in kinetochore length. The cells treated with nocodazole also had 15 times more kinetochores longer than 370 nm (**Table 23**).

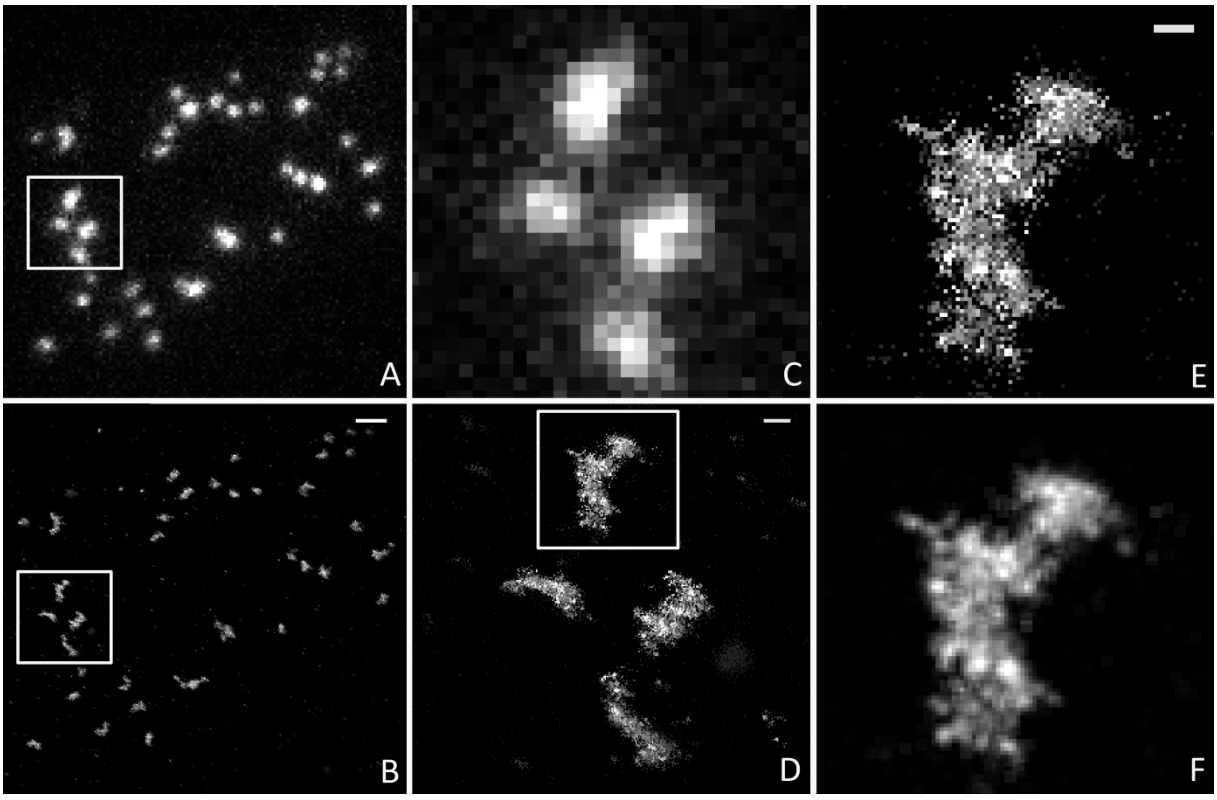

Figure 37. Nocodazole influence on the kinetochore chromatin. A) A wide-field image of kinetochore chromatin of a Hep-2 cell treated with nocodazole. Kinetochore chromatin labeled with primary antibody against CENP-A stained with Alexa-fluor-647. **B)** *D*STORM reconstruction of the same cell. Scale bar 1μm. **C)** Magnified detail from the frame in image A, wide-field. **D)** Magnified detail from the frame in image B, *D*STORM. Scale bar 200 nm. **E)** Magnified detail from the frame in image D, *d*STORM. Scale bar 100 nm **F)** Image E processed with smooth filter, *d*STORM.

Table 23. Comparison of the dimensions of the kinetochore chromatin assembled with CENP-A of cells treated with nocodazole and the kinetochores of untreated cells. The table compares the average kinetochore length, width, average thickness and the distance between kinetochore threads (average kinetochore thread thickness, average kinetochore thread distance), and portion of the kinetochores longer than 370 nm (% kinetochores longer than 370 nm) between cells treated with nocodazole (nocodazole) and cells without nocodazole treatment (untreated). * Standard error of the mean.

Kinetochore dimensions	untreated	nocodazole
Average kinetochore length	301 nm +/- 3 nm nm *	413 nm +/- 7 nm *
Average kinetochore width	193 nm +/- 1.6 nm *	276 nm +/- 4 nm *
% of kinetochores longer than 370 nm	5.4%	60.8%
Average kinetochore thread thickness	39.53 nm +/- 0.4 nm *	37.65 nm +/- 0.6 nm *
Average kinetochore thread distance	56.1 nm +/- 0.8 nm *	52.50 nm +/- 1.3 nm *
Irregular kinetochores	1%	13.1%
Number of analysed kinetochores	894	254

Along with the changes of outer dimensions and the appearance, the treatment with nocodazole caused changes in the inner structure of kinetochores. The threads inside the treated kinetochores were, on average, 1.88 nm thinner and 3.6 nm closer (**Table 23, Figure 41, and Figure 42**). The small difference in the thickness and distance between treated and untreated kinetochores was statistically significant (Two-tail t-test P = 0.010472 (kinetochore fiber width nocodazole-untreated).

The treatment with nocodazole in the concentration of 1µg/ml, which I used in the described experiments, caused depolymerization of microtubules and the inability of chromosome alignment at the equatorial plate. Because of this, it was impossible to recognize mitosis according to the alignment of kinetochores in the division plane. For this reason, I grouped the cells treated with nocodazole into two groups only according to the number of paired kinetochores. One group comprised the cells in the *G1 phase* and the other in the *G2 phase or mitosis*.

I examined whether the influence of nocodazole on cells in mitosis is stronger than the influence of nocodazole on interphase cells. For this, I compared the width of treated kinetochores, the length of treated kinetochores, and the thickness and the distance of treated kinetochore threads between the kinetochores in cells treated with nocodazole in *G1 phase* and between kinetochores of treated cells in the *G2 phase and mitosis*. Kinetochore chromatin in the *G2 phase and mitosis* was, on average, 31 nm wider and 44 nm longer than the kinetochore chromatin in the treated cells in the G1 (**Table 24**). Kinetochore chromatin threads of treated kinetochores in the *G1 phase* were 5.52 nm more apart than the threads of treated kinetochores in the *G2 phase or mitosis*. The difference in the width and length of kinetochores between treated cells in the *G1 phase* and the *G2 phase and mitosis* was statistically significant (Two-tailed t-test P =0.014012 (kinetochore width *G1-G2 and mitosis*), P =0.004566 (kinetochore length *G1-G2 and mitosis*). The difference in the thickness between kinetochore threads between the treated cells in the *G1 phase* and the treated cells in the *G2 phase and mitosis* was statistically insignificant.

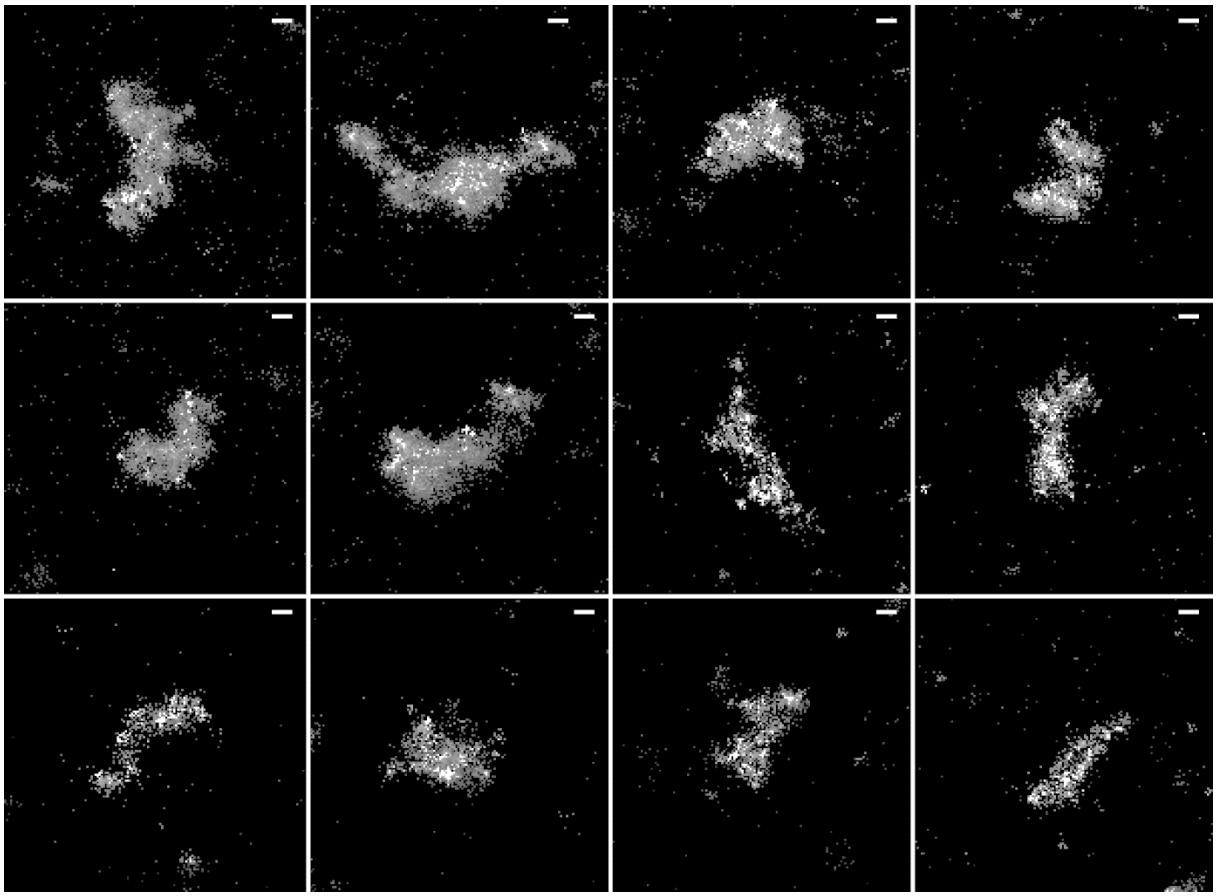

Figure 38. Nocodazole influence on kinetochore chromatin. This figure shows individual kinetochores treated with nocodazole. Scale bars 100 nm.

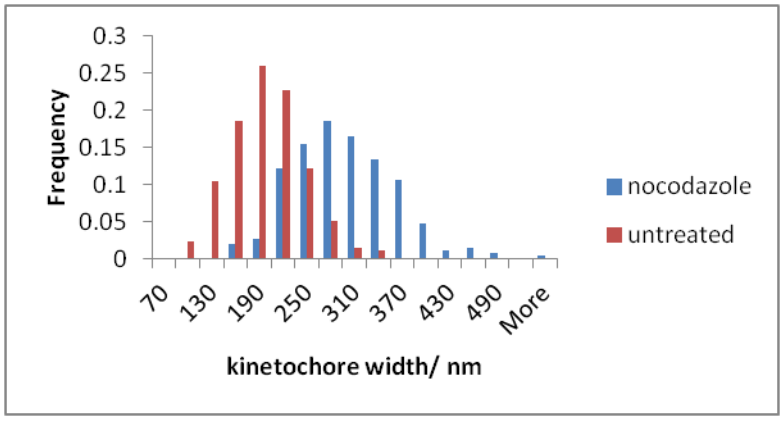

Figure 39. Influence of nocodazole on the width of kinetochores. This graph shows the distribution of the chromatin width of the kinetochores of Hep2 cells treated with nocodazole (nocodazole), and the width of kinetochores without nocodazole treatment (untreated). The width of the kinetochore chromatin is measured on the *d*STORM reconstructions of the kinetochore chromatin labeled with an antibody against CENP-A stained with Alexa Fluor 647.

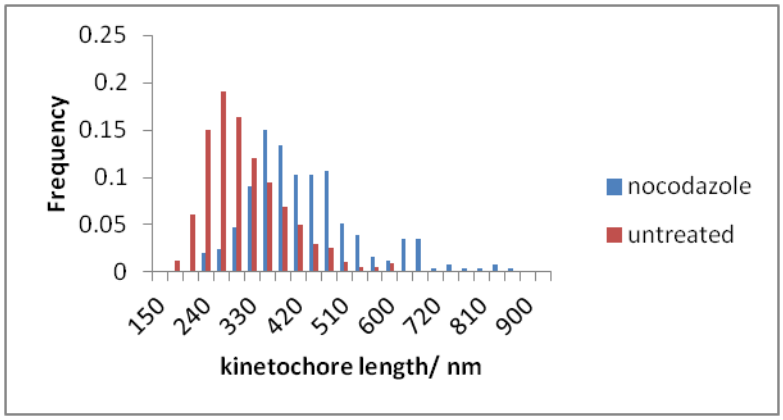

Figure 40. Influence of nocodazole on the length of kinetochores. This graph shows the distribution of length of the kinetochore chromatin assembly of the kinetochores of Hep2 cells treated with nocodazole (nocodazole), and the length of kinetochores without nocodazole treatment (untreated). The length of the kinetochore chromatin is measured on the *d*STORM reconstructions of the kinetochore chromatin labeled with an antibody against CENP-A stained with Alexa Fluor 647.

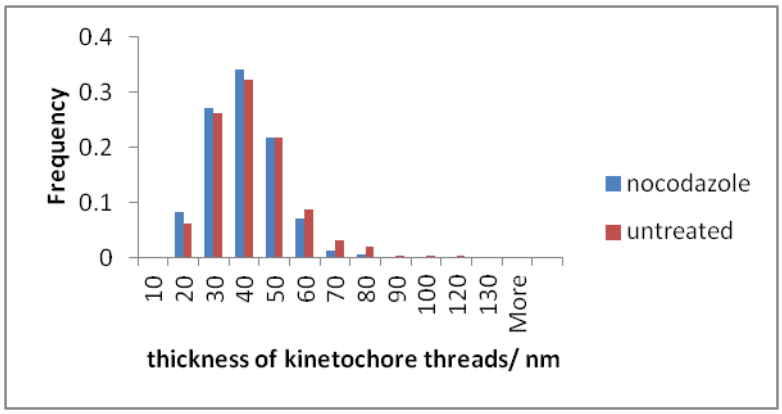

Figure 41. Influence of nocodazole on the thickness of kinetochore threads. This graph shows the distribution of thickness of the kinetochore threads inside of kinetochores assemblies of cells treated with nocodazole (nocodazole), and the thickness o kinetochore threads inside of the kinetochore chromatin assemblies of the kinetochores untreated with nocodazole (untreated). The thickness of the kinetochore fibers is measured on the *d*STORM reconstructions of the kinetochore chromatin labeled with an antibody against CENP-A stained with Alexa Fluor 647.

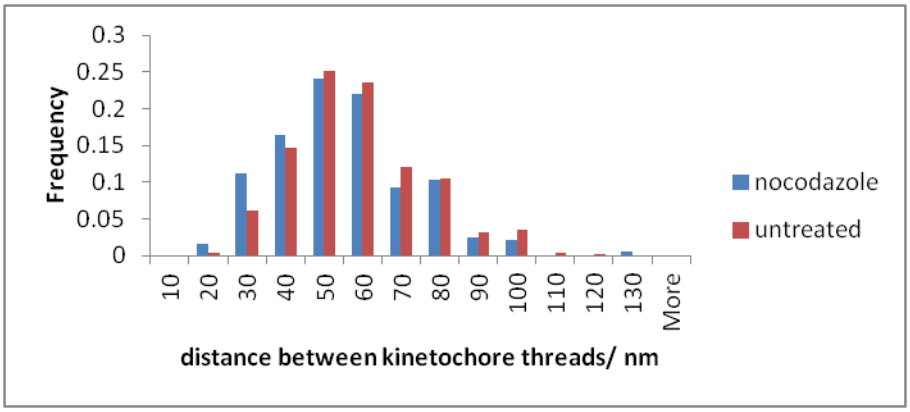

Figure 42. Influence of nocodazole on the distance between kinetochore threads. The graph shows the distribution of distances between kinetochore threads inside of kinetochores assemblies of cells treated with nocodazole (nocodazole), and the distances between kinetochore threads of kinetochores untreated with nocodazole (untreated). Distances between kinetochore threads don't have the normal distribution. The distances are measured on the *d*STORM reconstructions of the kinetochore chromatin labeled with an antibody against CENP-A dyed with Alexa-Fluor-647.

Table 24. Average dimensions of the kinetochore chromatin of the cells treated with nocodazole in the *G1 phase* (G1) and *G2 phase and mitosis* (G2 and mitosis). This table compares the average width of the kinetochore chromatin assembly (kinetochore width), the average length of the kinetochore chromatin assembly (kinetochore length), the average thickness of the threads inside of the kinetochore chromatin (kinetochore thread thickness), and the average distance between the centers of the threads inside of the kinetochore chromatin assembly (kinetochore thread distance). * Standard error of the mean.

	G1	G2 and mitosis
Kinetochore width	269 nm +/- 6 nm *	290 nm +/- 6 nm *
Kinetochore length	398 nm +/- 10 nm *	442 nm +/- 11 nm *
Kinetochore thread thickness	47 nm +/- 1 nm *	45 nm +/- 1 nm *
Kinetochore thread distance	64 +/- 2 nm *	59 nm+/- 1,8 nm *
Number of analysed kinetochores	88	142

Discussion

Determining the resolving power of *d*STORM on the test samples

By analyzing the distance of two fluorophores on the DNA origamis approximately 30 nm apart, I determined the resolving power of the *d*STORM microscope. Analyzing the distances of localization of closely positioned fluorophores on the DNA origami with the *d*STORM, I found a distance of 28 nm, which corresponds to the distances I estimated from the AFM images of DNA origami rectangles (**Table 16**). The density of pairs of fluorophores, mutually distanced on *d*STORM reconstructions between 15 and 30 nm, was half of the density of recognizable rectangles in AFM images of origamis laid on glass and approximately every second DNA origami was identified with *d*STORM (**Table 16**). By recognizing individual molecules of fluorophores on DNA origami, I showed that *d*STORM can distinguish individual molecules 30 nm apart or less, which was the target resolving power estimated to be necessary for distinguishing biological samples and the kinetochore chromatin.

Even though I used Alexa 647 for imaging kinetochore chromatin, for imaging DNA origami rectangles, I used Alexa 488 because it blinks in media of chemical composition appropriate for the disposition of DNA nanostructures. When laying the DNA origami on the glass, it was necessary to use a buffer that does not disturb the structure of DNA origami rectangles. The sulfur compounds necessary for the blinking of fluorophore Alexa 647 change the structure of the DNA. As Alexa 488 shines dimmer than Alexa Fluor 647, the resolution confirmed on the DNA origami rectangles with Alexa Fluor 488 could be improved if fluorophores with brighter blinking were used.

The DNA origami rectangles laid on the glass coverslip for the optical microscope were more irregular than DNA origami rectangles laid on the plastic surface for AFM (**Figure 12**). Thus, only every other origami on the coverslip looked like a rectangle. For this reason, in my hands, they were not the perfect test sample, which could precisely determine the resolving power of *d*STORM microscopy. However, the defined resolution of 30 nm is not far from the theoretical highest resolving power, which can be achieved on biological samples labeled with immunoglobulin antibodies for now. The maximal resolution power achievable in immunofluorescently labeled biological samples is around 15 nm because of the size of an immunoglobulin antibody of around 7 nm and the necessity to label the sample two times denser than the desired resolution power (Nyquist 1928, Shannon 1949). Proven resolution power is in agreement with the resolving power achieved with *d*STORM by other researchers (Russ et al. 2006, Heinemann et al. 2008.)

I used the biological test samples of microtubules and actin filaments to examine the faithfulness of the *d*STORM reconstruction because they have a known thread structure. With *d*STORM reconstructions, I obtained their faithful images (**Figure 14**, **Figure 15**) without the typical artifacts of blurring the intersection of lines, which is caused by imprecise localization because of the overlapping of PSF of individual molecules (Henriques et al. 2009).

The structure of the kinetochore chromatin assembly

The resolving power I achieved with *d*STORM in the samples of kinetochore chromatin labeled with antibodies against CENP-A was sufficient to discover the dimensions, shape, and inner architecture of the peripheral centromere chromatin on kinetochore base assembled with CENP-A, hereinafter the kinetochore chromatin (**Figure 16-Figure 20**). The kinetochore chromatin assembly had most often a rectangular shape, and in the interphase, it was, on average, 227 nm long and 234 nm wide. The kinetochore length in mitosis was, on average, 338 nm, and the width was 173 nm (**Table 17**). The width of the kinetochore rectangle was measured at the side approximately parallel to the length between sister-kinetochores. Kinetochore dimensions on the *d*STORM reconstructions correspond to the dimensions of metaphase kinetochores obtained by immunoelectron microscopy (length 235 nm, width 125nm, and thickness 150 nm (Marshall et al. 2009). The measured dimensions of the kinetochore assembly in interphase also correspond to the dimensions of the kinetochore rosette of the diameter of 250 nm, measured with high-resolution light microscopy (Andronov et al. 2019). In the research of Andronow, similar images of kinetochores like in this work could be recognized, but the internal structure of the kinetochore chromatin assembly nor its change during the cell cycle was not investigated in that research.

The average dimensions of the paired kinetochore in the *G2 phase* were different from the dimension of the *mitotic* kinetochore (**Table 17**), even though they were equally oriented concerning the Z-axis of the image space as *mitotic* kinetochore pairs. Therefore, the difference in kinetochore dimensions is not caused by their orientation, but with the change in the arrangement of kinetochore chromatin.

The outer and inner dimensions of kinetochores obtained by *d*STORM in this research corresponded to the length and width of the kinetochore chromatin determined on immunoelectron micrographs (Marshall et al. 2009). However, with *d*STORM, I distinguished the shape of arrangement of kinetochore chromatin assembled with native quantities of CENP-A and their inner structure at a resolving power of less than 30 nm. The enhancement of the resolution in kinetochore chromatin samples in comparison with the immunoelectron microscopy I achieved by dense labeling of CENP-A by using fluorescent primary antibodies against CENP-A. The enhancement of the resolving power in the comparison with the previous localization microscopy of kinetochore chromatin (Ribero et al. 2009, Gunkel doctoral thesis 2010) and the *d*STORM research of the kinetochores of other researchers (Wynne and Funabiki 2016) was in my opinion achieved by the use of the brighter fluorophores, with a better time separation of the images of the individual molecules, with increased contrast by the use of HILO illumination and with an increased stability of the microscope during the measurement.

The arrangement of the kinetochore chromatin assembly mostly consisted of parallel and vertical lines, which I called kinetochore threads. Based on the *d*STORM microscope resolving power, I found their average thickness is 39 nm, and the distance between the centers is 56 nm (**Figure 22**). 25 of 1340 measured kinetochore threads looked thinner than 20 nm, and 250 of 1340 kinetochore threads appeared thick between 20 and 30 nm (**Figure 21**).

If we consider the precision of localization, the size of immunoglobulin antibodies of around 7 nm, and the pixel-size of 10 nm in the *d*STORM reconstructions, the 10 nm chromatin fibers on *d*STORM images should be thick around 25 nm. The local resolution depends on the local background and the brightness of the individual bright states during the blinking of fluorophores. Background fluorescence and local chemical conditions that determine the brightness of blinking can vary in the field of view. The determined resolving power of the *d*STORM microscope of 30 nm is not enough to precisely measure the thickness of chromatin lines nor to prove the presence of structures thinner than 30 nm. Still, the presence of structures thick around 30 nm, or thinner, on *d*STORM images imply that the kinetochore chromatin is composed of the basic chromatin thread thick around 10 nm, composed of DNA wrapped around histones like beads on a string. The connection of such thin fibbers into thicker structures would explain the normal distribution of thickness of the kinetochore lines.

25 kinetochore fibers were reconstructed as thinner than 20 nm. The thickness of the kinetochore threads is normally distributed without peaks every 30 nm (**Figure 21**) that would have been expected if the kinetochores were have been build from the basic unit of kinetochore fiber of thickness above 30 nm. On *d*STORM reconstructions, structures could look thinner because of the coincidental distribution of imaged fluorophores on them in a line, precisely one behind each other, but this event would be less probable the thicker the kinetochore fiber is.

The measured distance between kinetochore fibers between 20 and 110 nm with the peak of the distribution at 40 to 50 nm, (**Figure 22**), corresponds to the distances between the lines on immunoelectron images of the kinetochore. On them, on nine kinetochores, the measured distances between the centers of kinetochore fibers were between 25 and 33 nm (**Figure 1**)(Marshall et al. 2009). To observe two chromatin structures separated from its centers less than 30 nm on acquired *d*STORM reconstruction, they have to be at least 5 nm thinner because of the pixel size of the reconstructed image. Therefore, it is unlikely that the arrangement of the kinetochore chromatin is composed of supercoiled chromatin structures like DNA solenoids thick 30 nm or more, as Finch and Klug 1976 proposed based on electron micrographs of unfolded chromatin (Finch and Klug 1976). The Absence of 30 nm chromatin fibers in kinetochore chromatin also corresponds with more recent cryoelectron tomography of metaphase chromosomes (Eltsov et al. 2008). 30 nm solenoids observed by Finch and Klug might be results of chromatin preparation for imaging. 30 nm thick structures observed by Finch and Klug might also come from the parallel merge of two or three 10-nanometre chromatin fibers, as found in this thesis. Considering the portion of kinetochore chromatin assembled with CENP-A in the total chromatin, the 30-nanometre chromatin structures on electron micrographs of Finch and Klug probably did not come from the kinetochore chromatin. Therefore, electron micrographs of chromatin structures and *d*STORM reconstructions of the kinetochore chromatin assembled with CENP-A probably represent a different part of the chromosome. 30 nm solenoids may exist on some part of some chromosomes, or they could be present in only some species, but taking into account this research, and the newest cryoelectron tomography, most of the chromosome is organized from the basic unit of 10 nm chromatin fiber into a structure that is not very regular. Nevertheless, by applying and perfecting the *d*STORM for chromatin samples, I discovered a new chromatin structure of size 10 to 100 nm.

The resolution of around 30 nm achieved in this work is not enough to precisely determine the size of the resolved kinetochore threads. Nevertheless, according to the dimension of the kinetochore threads resolved with *d*STORM in this work, the observed kinetochore chromatin assembly is assembled from the basic chromatin fiber composed from DNA, histones, and other attached proteins. Based on my *d*STORM images of kinetochore chromatin, I suggest the "shoelaces" model of chromatin (**Figure 43**). In this model, the 10-nm chromatin thread would stretch to the end of the kinetochore chromatin arrangement and then turn around and go back like the thread of the shoelaces. Such 10-nm chromatin threads are cross-linked into a thicker structure. The arrangement of kinetochore threads might, but would not have to, go to the depth of the chromosome forming threads like laces parallel or vertically to the first layer. The two layers might be similarly connected as the 10-nm threads and mutually connected. Such an arrangement would enable approximately similar outer dimensions of the kinetochore chromatin on centromeres, despite the big difference in the size of the periphery centromere chromatin assembled with CENP-A among the kinetochores of different chromosomes.

The interphase kinetochore chromatin is resistant to uncoiling almost as the mitotic kinetochore chromatin; nevertheless, it allows the transcription of normal eukaryotic active genes (Chan et al. 2011). Its resistance to uncoiling is in agreement with the suggested model of the kinetochore chromatin like shoelaces and against the coiling of the kinetochore chromatin into a rigid super-coiled 30-nm fiber. The genes in the 30-nanometre fiber, formed by the coiling of the 10-nm chromatin fiber, would be hardy accessible for transcription in their compact coiled form.

Analysis of the kinetochore chromatin assembly dimensions through the cell cycle

The structure of the kinetochore chromatin assembled with CENP-A passed through the cell cycle without big perturbations, and kinetochore chromatin assemblies in all phases of the cell cycle were mostly compact, with typical parallel and vertical threads in its interior. Kinetochores of the different outer shapes were present in a similar portion in all phases of the cell cycle (**Table 21**, **Table 27**). Kinetochore width and length changed during the cell cycle, and the thickness and distances between the centers of kinetochore threads inside of the kinetochore chromatin assemblies changed subtly.

The G1 phase

The kinetochores were the most compact in the G1 phase when they were, on average, 206 nm wide and 276 nm long (**Table 20**) and consisted of threads that were, on average, 44,9 nm thick and 55,4 nm distant from the centers (**Table 22**). The kinetochores in the G1 phase were, on average, the widest, the shortest, and had the thickest threads in comparison with the kinetochores in other phases of the cell cycle (**Table 25**). Cells in the G1 phase of the cell cycle contained more *compact kinetochores with an undefined inner structure* than the S phase and the G2 phase of the cell cycle (**Table 21**).

Kinetochore chromatin in the G1 phase contains twice the amounts of CENP-A compared to other phases of the cell cycle because CENP-A is then incorporated in the chromatin. The biochemical process of CENP-A incorporation might have influenced and changed the thickness of kinetochore threads. Larger amounts of CENP-A on the kinetochore threads in the G1 phase also might cause them to appear thicker on the *d*STORM images than the threads with smaller amounts of CENP-A in other phases of the cells cycle appeared. This is because CENP-A was the only labeled and visible molecule in the microscope. Nevertheless, a relatively bigger width of the kinetochore threads in the G1 phase was not exclusively the consequence of denser labeling and better visibility. The kinetochore threads in prometaphase, when there is no change in the amounts of CENP-A, were also significantly thicker than the threads in the G2 phase (**Table 18**). To get a better insight into the changes of inner and outer dimensions of the peripheral centromere chromatin on the basis of the kinetochore, occupied with CENP-A, during the cell cycle, I presented them in **Table 25**.

Rosette-like structures of the kinetochore chromatin in the G1 phase of the cell cycle, recently imaged with high-resolution light microscopy (Andronow et al. 2019) would correspond to the irregular loose kinetochores described in this work (**Figure 19**).

Table 25. Inner and outer dimensions of the kinetochore chromatin throughout the cell cycle. The table shows the width of the arrangement of the kinetochore chromatin occupied with CENP-A, labeled with fluorescent primary antibodies against CENP-A. (kinetochore width), its length (kinetochore length) in the phases G1, S, and G2, prometaphase, and metaphase, as well as the average thickness of threads inside the kinetochore arrangement (width of kinetochore threads) and the distances between the centers of threads inside the kinetochore chromatin arrangement (Distance between kinetochore threads). The measurements in the same column, amongst which there is no statistically significant difference are shown in the same color.

Phaseof the cell cycle	Kinetochore width	Kinetochore lenght	Distance between kinetochore threads	Width of kinetochore threads
G1	206 nm +/- 4 nm	276 nm +/- 8 nm	55 nm +/- 1.6 nm	44 nm +/- 1.2 nm
S	223 nm +/- 5 nm	285 nm +/- 6 nm	49 nm +/- 1.7 nm	37 nm +/- 0.8 nm
G2	214 nm +/- 3 nm	281 nm +/- 3 nm	55 nm +/- 1.8 nm	37 nm +/- 0.8 nm
prometaphase	177 nm +/- 3 nm	340 nm +/- 5 nm	59 nm +/- 1.4 nm	40 nm +/- 0.8 nm
metaphase	164 nm +/- 4 nm	339 nm +/- 7 nm	57 nm +/- 1.6 nm	38 nm +/- 0.8 nm

The S phase

Cells in the S phase had more unfolded kinetochores of irregular shape than the cells in other phases of the cell cycle (**Table 21**). The kinetochores in the S phase significantly differed from the kinetochores in the G1 and G2 phases in their average width and in average thickness of the kinetochore threads inside of the kinetochore chromatin assembly (**Table 25**, **Table 20**, and

Table 22). The kinetochores in the S phase were significantly wider, on average 17 nm wider than kinetochores in the G1 phase, but the difference in length between kinetochores in G1, S, and G2 phases was statistically insignificant. The change of the width might be caused by the loosening of

the kinetochore chromatin due to the replication. The widening of the arrangement of the kinetochore chromatin due to transcription looks like a widening of shoelaces when the structure becomes looser and loses firmness (**Figure 43**). The threads inside of kinetochores in the S phase were, on average, 7.5 nm thinner than the threads in kinetochores in the G1 phase (**Table 25**). 26% of the measured kinetochore threads in the S phase were thinner than 30 nm, which was a 10%-increase concerning the portion of threads of the same width in the G1 phase (**Figure 35**). In cells that were in the S phase, it was possible to notice threads thinner than 20 nm. 12% of kinetochore threads in the S phase were thinner than 20 nm (**Figure 35**).

The distance from the centers of threads of kinetochores in the S phase was, on average, 6.4 nm smaller than the distance between centers of threads in the G1 phase (**Table 22**, **Table 25**). The measured change of the distance between the centers of kinetochore threads was probably not the consequence of the distancing of kinetochore threads but the thinning of kinetochore threads. Thinning of structures on *d*STORM images would cause distancing between their centers if they stayed equally spaced from their edges. According to the measured change of thickness and the distance, kinetochore threads in the S phase are thinner but equally spaced from their edges like kinetochore threads in the G1 phase. I chose to measure the distance between the centers of threads because it was difficult to define the edge of the thread on reconstructed images objectively.

The cells in the S phase had gigantic kinetochores with loose inner structure and very thin threads in their interior (**Figure 32**). The thinning of kinetochore threads, the widening of the kinetochore chromatin, and the presence of gigantic loose kinetochores in the cells in the S phase indicate the loosening of the arrangement of kinetochore chromatin. As it was noticed only in the S phase, it is probably a consequence of DNA replication. Although kinetochores in the S phase had a looser structure than the kinetochores in other phases of the cell cycle, they kept their basic structure with recognizable parallel and vertical lines.

The preservation of the basic structure and the widening of the kinetochore in the replication process agree with the suggested “shoelace” model (**Figure 43**). According to this model, the kinetochore chromatin consists of 10-nm chromatin threads crosslinked together to form structures of various thicknesses. Such a structure might easily loosen and release the 10-nm chromatin fiber to allow the replication and transcription. On the other side, the thick and super-coiled kinetochore fiber would hardly go through the replication process without major uncoiling, and its uncoiling would increase the dimensions of the kinetochore so much that the change would be visible with an ordinary optical microscope. The same uncoiling and a big change of the dimensions would have to happen to incorporate newly synthesized CENP-A in the G1 phase, but it was never noticed (Andronov et al 2019). Such significant changes during the replication of kinetochore chromatin have not previously been published. Based on 932 kinetochores imaged in this work, kinetochore chromatin is not coiled into thicker fibers that uncoil during DNA replication of the kinetochore chromatin.

The G2 phase

With the transit of a cell from phase S into phase G2, the outer dimensions of the kinetochore returned to those in phase G1**.** The kinetochores in the G2 phase were narrower than the kinetochores in the S, and they had similar outer dimensions like the kinetochores in the G1 phase (**Figure 33**, **Figure 34**, **Table 20**, and **Table 25**). Compaction of the kinetochore chromatin to its original dimensions after the replication might cause this.

In contrary to the outer width of the kinetochore chromatin arrangement, which was similar in the G1 and the G2 phase, the thickness of the chromatin threads in the G2 phase was similar to the thickness of threads in the S phase and smaller than the thickness of the kinetochore threads in G1 phase (**Figure 35**, **Table 22**, **Table 25**). The similarity of the average thickness of kinetochore threads, and the number of very thin threads in S phase and G2 phase, indicate that the inner structure of the kinetochore chromatin threads in the scale between 10 and 200 nm in the S phase changes and stays in the same state in the G2 phase. This change in the thickness of the kinetochore chromatin thread might be caused by replication. It could also be a consequence of some other inner biochemical change on the kinetochore chromatin that happens in the S phase and persists till the next G1 phase.

The change of the kinetochore chromatin fiber thickness in the S phase that persists through the G2 phase is in agreement with the measurement of FRET distances in kinetochore chromatin. It also corresponds with the atomic force microscopy (AFM) of the kinetochore chromatin assembled with CENP-A. FRET measurements of distances between C-terminal and N-terminal end of CENP-A show that kinetochore chromatin assembled with CENP-A rearranges in the S phase and stays arranged like in the S phase also in the G2 phase (Bui et al. 2012). AFM measurements show that the CENP-A nucleosome is bigger in the G1 chromatin and becomes smaller in the S phase, and stays in the same dimensions as in the S phase in the G2 phase and mitosis (Bui et al. 2012).

A different amount of CENP-A on the kinetochore chromatin in the G1 phase might have influenced the kinetochore chromatin to look wider on *d*STORM reconstructions, but the kinetochore chromatin threads might be physically thicker because of the different amount of CENP-A. The difference in the thickness of kinetochore threads in *d*STORM images of the kinetochore chromatin was probably not exclusively caused by the decrease of the quantity of CENP-A in the chromatin fiber, the thickness of kinetochore threads again statistically significant increases in prometaphase without incorporation of new CENP-A. The biggest measured thickness of the kinetochore threads assembled with CENP-A in the G1 phase, therefore, represents a physical difference in the thickness of the kinetochore fibers, rather than an effect of the labeling on the *d*STORM image reconstruction.

Mitosis

Prometaphase

With the transit of cells into prophase, the average width of the chromatin threads is increased by 3.2 nm, and the distance of kinetochore threads by 5.3 nm in comparison to cells in the G2 phase (**Table 18**). The increase of width might be caused by the increased cross-linking or by the change of conformation of the kinetochore chromatin threads. With the entry into mitosis, the outer dimensions of the kinetochore chromatin assembly (kinetochores in further text) significantly changed. Kinetochores became more extended and narrower compared to those in the G2 phase (**Table 17**, **Figure 26**, **Figure 27**). In mitosis, the average cell ratio of the kinetochore width and length decreased with the average distance between sister-kinetochores (**Figure 28**). Kinetochores in *late prometaphase* have the lowest ratio of width and length (**Figure 29).** The coincidence of the kinetochore width and length ratio decrease with the increase of the distance between sister-kinetochores indicates that a kinetochore chromatin change under the influence of the spindle apparatus microtubule forces. While the chromatin of the inner centromere widens, the kinetochore chromatin becomes narrower. The narrowing and elongation of the kinetochore chromatin with the distancing of the sister kinetochores clearly show that the kinetochore chromatin in mitosis behaves differently than the inner centromere chromatin. The kinetochore chromatin in mitosis works as a different physical unit from the inner centromere chromatin.

Pulling forces of the spindle apparatus microtubules on kinetochores, while moving towards the cell pole, cause them to narrow between the inner kinetochore regions of the kinetochore chromatin, with CENP-C and the outer kinetochore protein Cdc20 (Dumont et al. 2013). The enhanced resolution of kinetochore chromatin images achieved with *d*STORM indicates that the shrinking of *prometaphase* kinetochores under the influence of the spindle apparatus microtubule forces happened in the region of the kinetochore chromatin occupied by CENP-A. Since CENP-C is mostly attached to the region of CENP-A (Suzuki 2014), the narrowing of the kinetochore chromatin assembled with CENP-A, found in this work, would also cause the decrease of the distance between the centers of localization of CENP-C and CDC 20 like found by Dumont et al. 2012.

The ratio of width and length of individual kinetochores did not change regularly with the distance between sister-kinetochores like average cell width and length ratio. That might be due to natural variations in the dimensions of individual kinetochores. Irregular changes in the width and length ratio of individual kinetochores with the distance of the sister kinetochores might be caused by the quick change of their width due to the pulling by microtubules during oscillations. Microtubule forces during oscillations of chromosomes in the equatorial plate are changeable due to the dynamics of kinetochore microtubules (Dumont et al. 2012).

Two cells significantly deviated from the synchronized change of the average ratio of width and length with the distance between sister-kinetochores (**Figure 28**, **Figure 29**). Those cells had the highest variance of angles between length connecting sister-kinetochores, and they were in very early prometaphase (**Figure 49**, **Table 28**). The disproportional ratio of width and length of their kinetochores with the distance between sister-kinetochores might be caused by the incomplete condensation of the inner centromere, making it more susceptible to stretching. The research of

causes of the different stretching of the inner centromere chromatin in early prometaphase surpasses the aim and scope of this thesis.

Metaphase

The outer dimensions and the width of the threads or lines inside of the kinetochore chromatin in *metaphase* looked like the kinetochores in *metaphase* returned to previous dimensions (**Table 18**). The width of threads significantly decreased in *metaphase* in regards to *prometaphase* and was similar to the width of threads in the *G2 phase*. (**Table 18**).

The ratio of width and length of the kinetochore chromatin in *metaphase* cells, which have sister-kinetochores further apart from 1140 nm, increased with the distance of sister-kinetochores (**Figure 28**, **Figure 29**). The observed widening of the metaphase kinetochore chromatin compared to the *late prometaphase* kinetochore chromatin is in agreement with microscopic measurements of the width of kinetochore chromatin areas with optical and electron microscopes. Suzuki found by optical microscopy a mild widening of the area of the CENP-A in metaphase in comparison to late prometaphase (Suzuki et al. 2014).

The change of the dimensions of the structure of kinetochore chromatin that I measured at the entry into prophase and the return to old dimensions in metaphase (**Table 18**) indicate that they were reversible and might have been caused by the pulling forces during oscillations of chromosomes in the equatorial plate. The relative widening of the *metaphase* kinetochore chromatin compared to the *late prometaphase* kinetochore chromatin also might have been caused by the forces of the spindle apparatus microtubules, which might be different in the metaphase. By relative widening and by thinning of their internal chromatin threads to the thickness of chromatin threads of *G2* kinetochores, metaphase chromatin might return to previous dimensions. The return to previous dimensions in metaphase might have been caused by the balancing of forces when oscillations in late metaphase stop.

The simultaneous return of kinetochore outer dimension to previous dimensions and the return of the inner dimensions of kinetochore chromatin threads to pre-mitotic values are in favor of force balancing as the leading cause of the change of the kinetochore chromatin dimensions. The measured reversible change of the outer dimensions and inner structure of kinetochore chromatin under the influence of force means that the change of kinetochore chromatin dimensions could function as a sensory mechanism for the detection of kinetochore alignment at the equatorial plate. The ability of the kinetochore chromatin to detect the correct alignment of kinetochores with its change of dimensions under the influence of force, observed in this work, might be connected to signalization for the onset of anaphase at the kinetochore. It shows that the kinetochore chromatin is able to detect and to respond to forces of the spindle apparatus.

The return of *metaphase* kinetochores to previous dimensions due to the abatement and balancing of forces in the metaphase simultaneously with stretching of the inner centromere seems contradictory because then the forces of the inner centromere would have to be opposite to the forces at the kinetochore chromatin. The opposed direction of forces that work on inner centromere chromatin and kinetochore chromatin can be explained with the recently discovered overlapping

microtubules that link sister k-fibers and balance the forces on bi-oriented kinetochores (Kajtez et al. 2015). Molecular motors on overlapping microtubules might create a force that stretches the inner centromere but simultaneously pushes the kinetochores towards kinetochore microtubules fibers. In this way, overlapping microtubules might balance the pulling forces created on kinetochores.

The balance and dynamics of forces which develop in the spindle apparatus by the actions of motor machinery is a very complex problem and an unresolved biological question under intense research (Dumont and Mitchinson 2009). By analyzing dimensions of numerous kinetochores in many cells in different substages of mitosis, I discovered a change of the outer dimensions of the kinetochore chromatin and the change in its inner structure that happens under the influence of microtubule forces in mitosis. Tracking of changes in the dimensions and the inner structure of kinetochore chromatin during the progress of mitosis might help in explaining the direction, dynamics, and scales of forces with which kinetochore microtubules affect kinetochores. The discovered reversible changes of the kinetochore chromatin under the influence of forces indicate that kinetochore chromatin might be the sensory mechanism for the detection of forces and the regulation of the cell cycle.

The influence of nocodazole on the kinetochore chromatin

Nocodazole changed the length, width, and the inner organization of the kinetochore chromatin assembly (**Table 23**, **Figure 37**, **Figure 38**). The kinetochores treated with nocodazole in concentration, which causes depolymerization of the microtubules were 40% wider and longer than the untreated kinetochores (**Table 23**) The treated kinetochores appeared elongated and disorganized and had a larger portion of the irregularly shaped kinetochores, then the untreated cells (**Figure 37, Figure 38**). Due to the depolymerization of microtubules in the treated cells, it was not possible to define the phase of the cell cycle per kinetochore alignment at the equatorial plate. Nevertheless, the increase of dimensions of treated kinetochores surpassed the changes in the dimensions of kinetochores between the interphase and mitosis of untreated cells (**Table 23**, **Table 17**). Therefore, the increased dimensions of treated kinetochores could not have been caused by an increased portion of mitotic cells.

The untreated kinetochore chromatin assembled with CENP-A in the immunoelectron micrographs stretches along 2/3 of length and 1/3 of the height of the centromere constriction (Marshall et al. 2009). The 40%-increase of the length of kinetochores under the influence of nocodazole might cause the extension of the kinetochore chromatin outside the centromere constriction. Such expansion areas of the kinetochore chromatin outside of the centromere constriction could allow the construction of whole kinetochore protein complex and linking of chromosomes to microtubules outside the centromere constriction. Expansion of kinetochores outside of the centromere constriction could facilitate the binding of microtubules coming from the unmatched spindle pole and merotelic binding of kinetochores to spindle apparatus. It is already known that small concentrations of nocodazole cause increased merotelic attachment where a single kinetochore binds to microtubules coming from both poles of the mitotic spindle (Ladrach et LaFontaine 1986). Thus, the construction of a compact kinetochore within centromere constriction could be one of the ways by which cells regulate proper kinetochore binding to the mitotic spindle. Then the role of the

folding of the kinetochore chromatin in a specific way into an assembly of specific dimensions would be the regulation of the size and the position of the full kinetochore complex in the centromere constriction. Besides this, compaction of the kinetochore chromatin by assembling its inner structures into a specific arrangement might be the physical mechanism of the creation of the centromere constriction itself. Nocodazole might also cause the disappearance of a centromere constriction by disturbing the specific assembly of the kinetochore chromatin.

The kinetochore chromatin assembly treated with nocodazole had the thinner chromatin threads or lines inside the kinetochore for an average of 1.88 nm. The chromatin threads inside the kinetochores treated with nocodazole were 3.6 nm closer than the threads inside the untreated kinetochores (**Table 23**). The difference in the distance between kinetochore threads of treated and untreated kinetochores was two times smaller than the difference of their thickness (**Table 23**). The decrease in the thickness of the chromatin threads of nocodazole treated kinetochores could influence the measurement of the distance between their centers. Although the change in the average thickness of the kinetochore chromatin threads treated with nocodazole was small, it was statistically highly significant. This clearly showed that nocodazole changed the interior arrangement of kinetochore chromatin threads. Nocodazole might cause small thinning of kinetochore chromatin threads by disturbing the incorporation of chromatin proteins into the kinetochore chromatin and attachment for DNA. Nocodazole might also disturb the interconnection of the basic DNA fiber into the thicker structure.

Nocodazole increased external dimensions, disrupted the internal organization of the kinetochore chromatin assembly, and changed the dimensions of chromatin threads inside of the kinetochore. The internal organization of kinetochore chromatin intro parallel and orthogonal threads and consequently a compact rectangular assembly is, therefore, probably a result of the internal building plan of the kinetochore chromatin. The internal building plan of kinetochore chromatin might be determined by the composition of basic kinetochore chromatin fibers and incorporation of the DNA binding proteins, which can crosslink basic chromatin threads. CENP-C probably crosslinks chromatin strands. CENP-C has several domains that can bind DNA (multiple DNA binding domains), it can create homodimers, and it could participate in the cross-inking of chromatin (Kato et al. 2013). By reducing the amount of CENP-C, the kinetochores lose compactness and increase the sensitivity for unfolding (Ribero et al., 2010). Kinetochores with reduced amounts of CENP-C are more elastic than kinetochores with native amounts of CENP-C. They also stably bind incorrectly bound microtubules and have the reduced capability of correction of incorrectly bound microtubules (Suzuki 2014). Effects of CENP-C inhibition are, like nocodazole, connected with merotelic attachment, or the attachment of a single kinetochore to the microtubules coming from both poles of the division spindle. Additionally, inhibition of protein Pcs1 and Mde4 in yeast that might work as a clamp for cross-linking of chromatin also increases merotely (Rabitsch et al 2003, see in Gregan et al. 2011).

Taken into account the effects of nocodazole on the plan of building of kinetochore chromatin, demonstrated in this work, and previously discovered effects of nocodazole on kinetochore dimensions and merotelic attachment of kinetochores, I hypothesize that the external dimensions of kinetochores and the function of kinetochore chromatin are a result of its internal building plan.

Together with the discovered role of the kinetochore building plan, discoveries about the role of CENP-C imply that CENP-C is one of the main organizers of the kinetochore chromatin building plan.

Kinetochore chromatin of cells in the G2 phase and mitosis was more sensitive to the change of the dimensions, caused by nocodazole than the kinetochores of cells in the G1 phase (**Table 24**). Nocodazole prevented the narrowing of kinetochores in mitosis. Untreated mitotic kinetochores were, on average, 33 nm narrower and 62 nm longer than untreated interphase kinetochores. Untreated kinetochores in the G2 phase and mitosis did not significantly differ from the kinetochores in the G1 phase in their width and length. In contrary to untreated kinetochores, kinetochores treated with nocodazole, which were in the G2 phase and mitosis together, were, on average, 21 nm wider than kinetochores treated with nocodazole which were in the G1 phase (**Table 24**). Widening of nocodazole treated kinetochores that were in the G2 phase and mitosis could not be attributed to pulling with microtubules but only to biochemical changes. Microtubules were depolymerized with nocodazole. The measured effect of nocodazole on kinetochores in mitosis and the G2 phase might come from the stronger effect of nocodazole on mitotic kinetochores. CENP-C is stably bound on interphase kinetochores but is mobile and exchanging fast on kinetochores during mitosis (Hemmerich et al. 2008). The stronger effect of nocodazole on mitotic kinetochores could, therefore, also be explained with the hypothesis that nocodazole changes kinetochore chromatin by disturbing the incorporation of CENP-C.

Changes of kinetochore influenced by nocodazole can also be well explained by the shoelace model proposed in this work (**Figure 43**). According to the model, the basic, about 10 nm thick chromatin fiber, is assembled like a shoelace and cross-linked with CENP-C in thicker lines. The disturbance of the transverse connection of basic DNA kinetochore fibers disturbs compaction and the kinetochore ability to sense and correct association with the microtubules coming from inadequate spindle pole. Kinetochore outer dimensions may vary depending on the frequency of transverse-connection proteins along the basic fiber. Their frequency determines the width of the kinetochore chromatin assembly. Lowering the frequency of transverse connection proteins, like CENP-C, kinetochore chromatin would be torn, less compact, wider, and generally stretched and looked similar to the kinetochore chromatin treated with nocodazole. Transverse connections on the basic fiber of DNA should be at least as frequent as the narrowest untreated kinetochore, i.e., 78 nm. I assume that the transverse kinetochore chromatin fiber comes to every 60 nm since after 60 nm, most of the lines inside of the kinetochore chromatin assembly were reconnected differently or split into two separate lines.

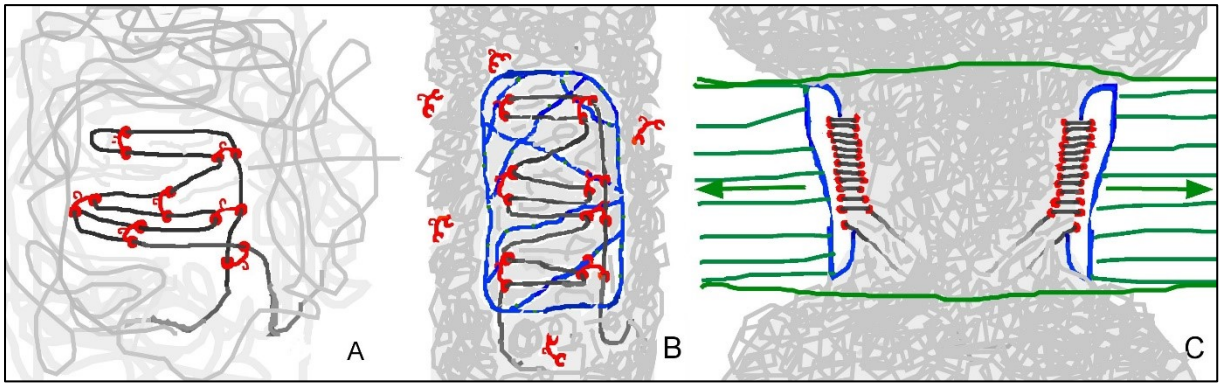

Figure 43. Graphical depiction of the Shoelace model. A) Kinetochore chromatin in interphase (dark grey curved lines) is approximately similar in width and length and interconnected with proteins that interconnect centromere chromatin by binding to CENP-A or DNA, possibly CENP-C (red hooks). Kinetochore chromatin occupied with Cenp-A is assembled in relatively parallel and orthogonal lines. **B) Front view on the kinetochore chromatin on a mitotic chromosome**. Outer kinetochore proteins (blue) are bound to the kinetochore chromatin. Mitotic kinetochore chromatin elongates, and its width is limited with the distance of the kinetochore chromatin interconnecting proteins on the chromatin fiber (red hooks). **C) Side view on the kinetochore chromatin in mitosis.** It shrinks due to the force of kinetochore microtubules (green) like dimensions of the shoelaces on the shoes when pulled. The pulled part of the shoelace becomes reconnected with newly bound chromatin interconnecting proteins (red holes). The end of the kinetochore chromatin (shoelace) is connected and held with the rest of centromere chromatin (light grey) and elongates when pulled or pushed by the kinetochore microtubules (green) attached to the outer kinetochore (bottom of the shoe, blue). The direction of forces on the kinetochore is depicted with green arrows.

A model of kinetochore chromatin with a similar basic plan, the so-called boustrophedon, was already proposed. The boustrophedon model is imagined based on the sensitivity of the chromatin kinetochore to unfolding and based on the position of kinetochore chromatin proteins along the unfolded chromatin fibers (Ribero et al. 2010).

Unlike the boustrophedon model, the shoelace model is created based on the *d*STORM reconstructions of kinetochores in the cell with the resolution power of 20 nm or more. Besides the building plan of kinetochore chromatin, the shoelace model describes the change of the kinetochore chromatin through the cell cycle, for example, the process of the DNA replication, and how kinetochore chromatin reacts to the forces of the mitotic spindle. The shoelace model also describes the importance of the specific kinetochore chromatin building plan for the function of kinetochores. Besides this, the description of kinetochore chromatin to be like shoelace is easy to imagine and remember, unlike the seldom-used word boustrophedon.

The practical applicability of the *d*STORM for imaging of chromatin

In this work, I have optimized the *d*STORM method for high-resolution imaging of centromere chromatin. Except writing of the localization software, the device drivers, and the preparation of the DNA origami rectangles, I obtained mostly independently all the steps in the application of the method; I identified specific antibodies against kinetochore chromatin proteins and stained one with

fluorescent dyes, optimized the labeling procedure to minimize unspecific fluorescence, build the stable TIRF/HILO microscope with appropriate sampling, adjusted and imaged the blinking of individual fluorophores in the sample, processed the movies of individual molecule blinking images with the localization software and measured the dimension of structures inside of the high-resolution images. With the achieved resolution, I discerned the plan of building of kinetochore chromatin assembly in the order of magnitude between 10 and 100 nm.

High-resolution in the samples of kinetochore chromatin was achieved with bright blinking of fluorophores, good spatial-temporal separation of the fluorescence of individual molecules, and good contrast. Good contrast was achieved with specific sample labeling, with a reduction of autofluorescence of the sample and with the illumination of the sample with the inclined light sheet. Improving the resolution compared to immunoelectron microscopy was achieved by dense labeling of the sample with fluorescent primary antibodies, which are about three times smaller than the labeling complex used in immunoelectron microscopy. The large field of view of *d*STORM TIRF/HILO microscopy in comparison to electron microscopy enabled simultaneous imaging of all kinetochores of one cell nucleus, which were in focus. This enabled the generation of high-resolution images of more than nine hundred kinetochores, which is hundred times more than the number of kinetochores recorded with kinetochore Immunoelectron dissection (Marshal et al. 2009), and ten times more than the number of kinetochores recorded with two-dimensional kinetochore chromatin immunoelectron microscopy (Suzuki et al. 2012). The reconstruction of such a large number of kinetochores enabled a good statistical analysis of kinetochores and their comparison between different stages of the cell cycle. Imaging of kinetochores in one cell also enabled the distribution of cells according to the sub-stages of the cell cycle without the use of mitotic toxins that might disturb chromatin structure. It also enabled comparison of the measured kinetochore properties with the other properties typical for the progress of mitosis, like sister-kinetochore distance and the stage of the alignment of chromosomes at the equatorial plate.

In this work, kinetochore chromatin was resolved with *d*STORM with similar resolving power like in the recently published study of Andronov (Andronov et al 2019). On images of Andronov, kinetochores of similar structure with parallel and orthogonal lines, as discussed in this work could be found, but their structure was not anlyzed or discussed in that work. Assembly of the kinetochore chromatin occupied with CENP-A in a specific structure composed of parallel and orthogonal lines is to my knowledge first time presented and discussed in this work.

In this work, kinetochore chromatin was resolved with *d*STORM with similar resolving power like in a recently published study of Andronov (Andronov et al 2019). On images of Andronov, kinetochores of similar structure with parallel and orthogonal lines, as discussed in this work could be found, but their structure was not analyzed or discussed in that work. Assembly of the kinetochore chromatin occupied with CENP-A in a specific structure composed of parallel and orthogonal lines is to my knowledge the first time presented and discussed in this work.

With *d*STORM, I found statistically significant changes in the thickness of inner kinetochore structures of only about 2 nm (**Table 17**, **Table 22**, **Table 23**, **Table 25**). This indicated that *d*STORM resolution, together with statistical analysis, approaches the resolution of FRET. Statistical analysis of values

measured on *d*STORMimages clearly showed the changeability of the kinetochore chromatin during the cell cycle in the scale of magnitude of 2nm to 300 nm. Moreover, the discovered changes of structures inside of the kinetochore chromatin during the cell cycle are in agreement with the FRET and AFM measurements of the kinetochore chromatin (Bui et al. 2012). For this reason, the combination of *dSTORM* and FRET measurement could be used to get a complete physical and biochemical model of kinetochore assembly during the cell cycle.

High-resolution in *d*STORM is achieved by manipulation of individual molecule fluorescence by adjusting the excitation light intensity, chemical composition of the media for immersion of the sample during the measurement, and by adjusting the density of the labeling fluorescent molecules inside of the imaged sample. *D*STORM is a light-microscopic method and was already applied in living cells (Klein et al 2010). Nevertheless, good resolution of compact samples demands a twenty-minute recording time for the separation of the blinking of close molecules. Such long recording is incompatible with living cells for their movement and sensitivity on a strong excitation light. For this reason, the application of the *d*STORM with 20 nm resolution in compact structures, from the side of biological research applicability, looks more like improved electron microscopy than light microscopy of living cells.

Investigation of force in cells often requires imaging of moving of cellular parts in living cells and imaging of perturbation and movement after application of force and its change. This is incompatible with fixed cells imaged at high-resolution *d*STORM. Nevertheless, *d*STORM can image a relatively big field of view and, in a reasonable time, create a large number of resolved structures of many cells in different stages of the cell cycle. Thus, a significant number of structures in all sub-stages of the cell cycle can be resolved and statistically compared to identify subtle changes that happen during mitosis and throughout the cell cycle. Another advantage of the generation of a large number of high-resolution structures in only one image is the possibility to generate enough data to investigate the influence of cytostatica on the chromatin architecture in only one experiment. Such high throughput microscopy methods are very interesting for the pharmaceutical industry.

Application of *d*STORM on samples of chromatin could be expanded with multi-color recording and three-dimensional imaging to obtain a complete picture of building a kinetochore. Two-colour *d*STORM recording of cellular structures is already applied to samples of microtubules and nuclear pores (Löschberger et al. 2012). A further improvement in the resolution of *d*STORM could be achieved by using smaller labeling molecules and brighter fluorophores. Since biotechnology of specific labeling molecules is developing fast and by chemical synthesis fluorophores with improved photophysical properties are created, further improvement of the *d*STORM technique is to be expected. Unfortunately, practical application in the biological samples is in a significant delay with the fast development of the technique.

In my opinion, for the research of kinetochore chromatin, it would be most interesting to investigate the perturbations of the kinetochore chromatin building plan caused by mitotic poisons and with inhibition of different protein-components of kinetochore chromatin. This would give a better insight into the mechanism at work and the function of kinetochore chromatin in general. *D*STORM could be

applied to uncover the building plan and its importance for the function of other chromatin assemblies, like telomeres and other functional parts of chromosomes.

Summary

The kinetochore is a chromatin-protein complex on the chromosome centromere. Kinetochore attach chromosomes to the microtubules of the spindle apparatus, recognize attachment to microtubules and regulate the progress of mitosis. The kinetochore protein complex is built on the periphery centromere chromatin. Due to the limited resolving power of the optical microscope and limitations of electron microscopy, the spatial arrangement of kinetochore protein and chromatin complex is unresolved. In this thesis, the human periphery centromere chromatin assembled with CENP-A (kinetochore chromatin in further text), on which kinetochore complex is built, was imaged by high-resolution optical microscopy called direct Stochastic Optical Reconstruction Microscopy (*d*STORM).

For *d*STORM of the kinetochore chromatin, a stable TIRF/HILO microscope was build, and the immunofluorescence labeling of kinetochore chromatin occupied with CENP-A was optimized. A resolution of 15 nm was achieved with this microscope on test samples of DNA origami and around 20 nm in the samples of the kinetochore chromatin. The achieved resolution was enough to resolve the shape and the building plan of the kinetochore chromatin.

With *d*STORM are properly reconstructed high-resolution images of around nine hundred kinetochores in the different sub-stages of interphase and mitosis. The kinetochore chromatin labeled with CENP-A is mostly arranged as parallel and vertical chromatin threads thick between 30 and 75 nm, which form a compact rectangular structure. Kinetochore chromatin assembly was between 145nm and 648 nm long, 302 nm on average. The kinetochores had a width between 78nm and 357 nm, on average 193 nm The thicknesses of 1354 threads inside of the kinetochore chromatin were measured. The threads within the kinetochores were between 12 nm and 110 nm thick.

Kinetochore assembly width, length, and thickness and the distances between the threads inside of kinetochores at different stages of the cell cycle are measured and compared. The kinetochore chromatin assembly during mitosis was narrower and longer than interphase kinetochore chromatin. Mitotic kinetochore chromatin assembly was on average 173 nm wide and 338 nm long. Interphase kinetochore chromatin was, on average 209 nm wide and 271 long.

Kinetochores were the most compact in the G1 phase; then, they were the shortest, the narrowest among interphase cells, and were composed of thickest threads. They were, on average 207 nm wide, 271 nm long, and their threads were, on average 44 wide. In the S phase loosening and unfolding of the kinetochore chromatin and thinning of threads inside was revealed. Kinetochores in the S phase were, on average 223 nm wide, 285 nm long, and their threads were, on average 37 nm wide. Changes in the thickness of the kinetochore threads were retained after compaction of the assembly in the G2 phase. Kinetochores of the G2 phase were, on average 214 nm wide, 281 nm long and their threads were 37 nm wide. Prometaphase kinetochores were, on average 177 nm wide, 340 nm long and had threads 40 nm wide. After sister-kinetochores in late mitosis separate more than 1140 nm, kinetochores become wider. This indicates that then, the force on kinetochores is pushing from the interior of centromere to the outer kinetochore.

The internal organization of the kinetochore chromatin and outer dimensions kinetochore chromatin are changed under the influence of mitotic poison nocodazole. Kinetochores treated with nocodazole were 40 % wider and longer than the untreated kinetochore, and they were irregular and less compact. Chromatin threads inside of the kinetochore chromatin were, on average, 1.88 nm thinner than the chromatin threads of untreated kinetochores.

According to the exterior dimensions of the kinetochore chromatin assembly, its internal organization, and its change during the cell cycle, a new functional model of kinetochore chromatin arranged like shoelaces is proposed. The shoelace model of kinetochore chromatin explains the plan of arrangement of kinetochore chromatin assembled with CENP-A and its changes during DNA replication and mitosis.

Supplementary data

Table 26. Antibodies that specifically recognize the human centromeres and fixation methods suitable for immunofluorescence labeling of the human kinetochore.

Name	Fixation method	Working concentration
Anti CENP-A (KinjaYoda)	methanol, formaldehyde, glutaraldehyde	1/200 -1/800
Anti CENP-A clone 3-19 (MBL)	methanol, formaldehyde, glutaraldehyde	1/100 -1/400
Anti CENP-B (Kinja Yoda)	methanol, formaldehyde, glutaraldehyde	1/200 -1/800
Anti CENP-C (Kinja Yoda)	methanol, formaldehyde	1/100 -1/400
ACA serum (FSU Uniklinik)	methanol, formaldehyde, glutaraldehyde	1/200 -1/800
CENP-F antibody NB 500-101C (Novus Biologicals)	methanol, formaldehyde, glutaraldehyde	1/400
Anti CENP-Q (Kinja Yoda)	methanol, formaldehyde	1/100 -1/400
Anti CENP-T (Kevin Sullivan)	methanol, formaldehyde, glutaraldehyde	1/100 - 1/200
Anti-CENP-T (ICEN22) (Human) mAb (MBL)	methanol, formaldehyde, glutaraldehyde	1/100 - 1/400

Table 27. Representation of different forms of the kinetochore in mitosis and the interphase The table shows the portion of compact rectangular kinetochores with parallel and vertical threads (Rectangular with lines), compact triangular kinetochores with parallel and vertical threads in the interior (Triangular with lines), irregularly shaped loose kinetochores with lines in the interior (irregular loose), compact kinetochores with undefined interior (compact, undefined interior), gigantic kinetochores (gigantic), double kinetochores (double kth), and the total number of kinetochores in the cells in the G1 phase (G1), in the S phase (S), in the G2 phase (G2), in mitosis (M), and among all cells.

Kinetochore form	G1	S	G2	Inter.	M	All
Rectangular with lines	86.0 %	60.0%	88.1 %	83.0 %	80.7 %	82.0 %
Triangular with lines	1.0 %	0 %	0.8 %	0.8 %	8.4 %	0.7 %
Irregular loose	1.6%	7.6 %	3.2 %	3.8 %	4.4 %	5 %
Compact, undefined interior	12.6 %	11 %	8.1 %	9.3 %	9.5 %	9.4 %
Gigantic	0 %	5.0 %	0 %	0.9 %	0 %	0.5 %
Double kth	0 %	16.1 %	0.8 %	1.2 %	0 %	0.7 %
Analyzed kth	94	118	245	621	427	1093

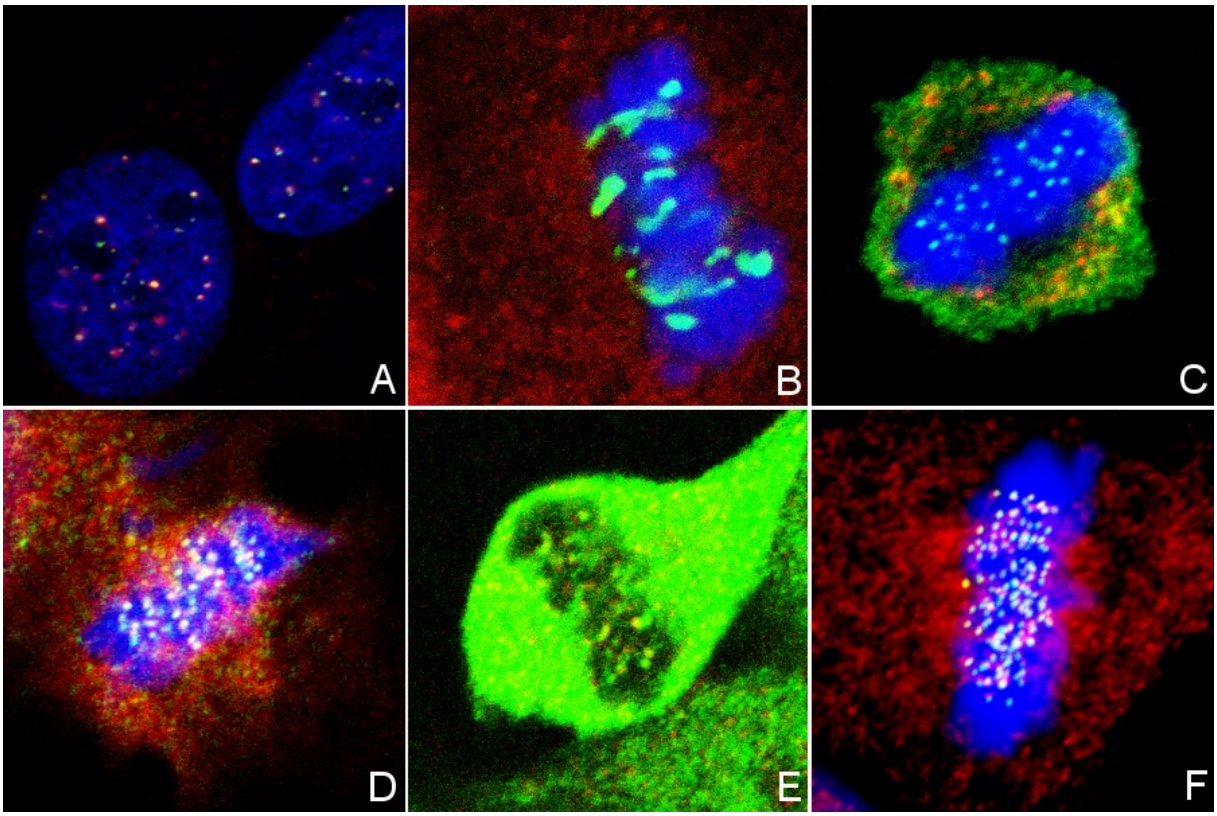

Figure 44. Centromere specificity of the tested anty-centromere antibodies A) Nuclear localization of Anti-CENP-A (from Kinja Yoda) and ACA antibodies from the serum of patients with CREST syndrome. Anty-CENP-A (green) was recognized with secondary antibodies dyed with fluorescent dye Cy2. ACA antibodies were recognized with secondary antibodies dyed with Cy5. Both antibodies were located in paired dots in the nucleus stained with DAPI (blue). Localization in paired dots is typical for centromere localization. **B)** Centromere localization of Anti-CENP-B from Kinja Yoda (turquoise). Any CENP-B antibody on chromosomes stained with DAPI (blue) was recognized with a secondary antibody dyed with a green fluorescent dye Cy2. Red staining in the cytoplasm comes from unspecifically bound secondary antibodies dyed with Cy3. **C)** Centromere localization of Anti CENP-C (turquoise) and cytoplasm localization from of anty CENP-H. CENP-C from Kevin Sullivan was detected on centromeres (turquoise) with a secondary antibody stained with Alexa-Fluor 488. Anty-CENP-H antibody (FL247) was detected in the cytoplasm unspecifically bound (red and yellow). It was detected by using the secondary antibodies stained with Cy-3. **D)** Anti-CENP-Q and Anti-CENP-A colocalization on the centromeres of mitotic chromosomes. Anti CENP-Q primary antibody from Kinja Yoda was detected by using a secondary antibody labeled with a fluorescent dye Alexa-Fluor-488 (white). Anty-CENP-A primary antibody was detected by using a secondary antibody stained with Cy3 (white) Cytoplasmic localization of parts of Anti-CENP-Q (yellow and green), and anty-CENP-A (red and yellow) indicates a loss of specificity due to the transport of antibodies in inappropriate conditions. **E)** Anti-CENP-F and Anty- CENP-I cytoplasmic localization. Anty-CENP-F was recognized in the cytoplasm (green) with a secondary antibody stained with Alexa-Fluor-488. Anty-CENP-I was recognized in the cytoplasm (red) with secondary antibodies stained with Cy3. **F)** Anti-CENP-T and Anti-CENP-A centromere colocalization (white). Anty-CENP-T antibody from Kinja Yoda was detected on chromosomes (blue) by using a secondary antibody stained with Cy3. Anti CENP-A was detected with secondary antibodies stained with Alexa-Fluor-488.

Table 28. Indicators of the progress of mitosis. The table shows the average cell values of the distance between sister kinetochores (sister-kinetochores distance), variance of angles between lengths that connect sister kinetochores in one cell (sister-kth angle st. dev.), ratio of sister-kinetochore pairs in equatorial plane (% kinetochores in equatorial plane), average distance of the midpoint of the length connecting sister kinetochores from division plane (sister-kinetochore distance from the division plane), average kinetochore width to length ratio (kinetochore width/length) and the width of the space with kinetochores perpendicular to the division plane (kinetochore space). Progress of mitosis was evaluated by the score of attributed points. For end values typical for late mitosis (red), positive points were attributed. For end values typical for early mitosis (blue), negative points were attributed. End values are determined according to the distribution of individual indicators of the progress of mitosis (**Figure 40**-**Figure 42**). Points are summed for every cell (score). Cells with positive scores are considered as *metaphase*. Cells with Score 0 are considered as *late prometaphase*. Cells with negative score are considered as *early prometaphase*. Measurement of distance between sister kinetochores (sister-kinetochore distance), angles between lengths that connect sister kinetochores and kinetochore width and length is depicted in figure12. Measurement of sister-kinetochore pairs in the equatorial plane (% kinetochores in equatorial plane), measurement of the average distance of the midpoint of the length connecting sister kinetochores from division plane (sister-kth distance from the division plane), and the measurement of the width of the space with kinetochores is depicted in **Figure 11)**.

cell	sister-kinetochores distance	sister-kth angle st.dev	% kinetochores in equatorial plane	sister-kth distance from the division plane	Kinetochore width/length	Kinetochore space	score
B	1165 nm	23.3°	54%	1438 nm	0.723	5939 nm	-2
I	1002 nm	18.95°	50%	1253 nm	0.494	4350 nm	0
M	1119 nm	8.6°	42%	1061 nm	0.492	3917 nm	0
O	1171 nm	18.92°	62%	718 nm	0.458	4187 nm	1
K	1074 nm	10.43°	54%	804 nm	0.503	3489 nm	0
N	1137 nm	7.32 °	42%	167 nm	0.499	5587 nm	0
F	968 nm	10.71°	50%	669 nm	0.549	3695 nm	0
J	1050 nm	13.43°	50%	822 nm	0.463	4813 nm	0
E	962 nm	17.97°	22%	1268 nm	0.586	4664 nm	-1
R	1243 nm	6.74°	50%	806 nm	0.496	4628 nm	0
L	1113 nm	11.59°	53%	1138 nm	0.454	3760 nm	-0
T	1344 nm	5.00°	83%	541 m	0.529	3026 nm	2
S	1243 nm	11.16°	57%	791 nm	0.474	3224 nm	0
H	1012 nm	11.27°	44%	1599 nm	0.506	4233 nm	-1
Q	1226 nm	12.49°	84%	328 nm	0.543	3183 nm	2
D	903 nm	6.76 °	54%	464 nm	0.606	3385 nm	0
C	893 nm	9.95°	22%	822 nm	0.671	3881 nm	-1
P	1185 nm	6.01°	80%	331 nm	0.529	2906 nm	3
G	959 nm	11.31°	22%	872 nm	0.536	4807 nm	-1
A	995 nm	13.42°	43%	993 nm	0.728	6581 nm	-1

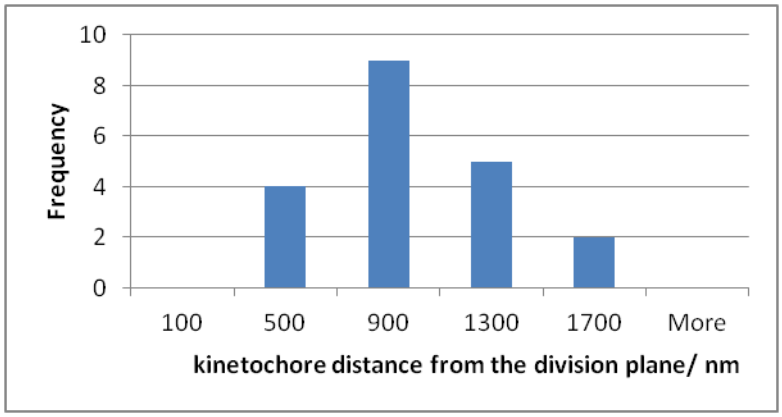

Figure 45. Distribution of mitotic cells with the different average kinetochore distance from the division plane. The division plane is defined as the line which most of the lines between sister kinetochores cross. Kinetochores are labeled with antibodies against CENP-A stained with Alexa-Fluor-647. Average cell sister-kinetochore distances between 500 and 900 nm are represented with the biggest number of 9 cells. Average cell sister kinetochore distances represented with less than five cells (halve the number with the maximal representation, or 9), are considered as end values of indicators of the progress of mitosis. Therefore, average cell sister-kinetochore distance below 500 nm is considered as end value typical for early prometaphase. To those four cells, negative points of mitosis indicators are attributed (table 26). Average cell sister-kinetochore distance above 1300 nm is considered as end value typical for late mitosis or metaphase. To those two cells, positive points of indicators of mitosis are attributed (table 26).

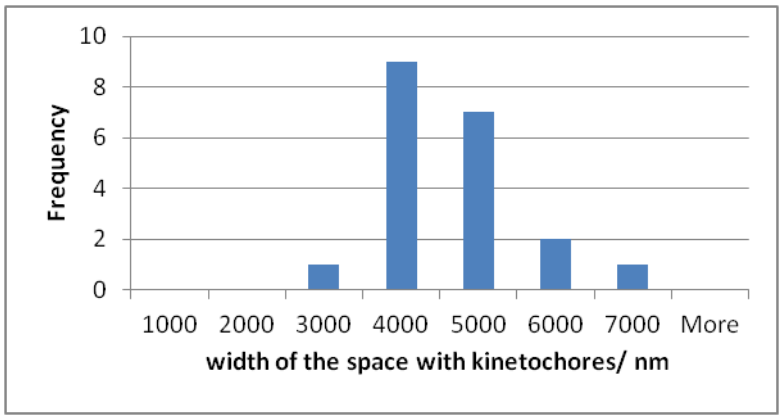

Figure 46. Distribution of mitotic cells with a different width of the kinetochore space. The width is measured perpendicular to the line of kinetochore alignment. Kinetochores are labeled with antibodies against CENP-A stained with Alexa-Fluor-647. Kinetochore space 3000 to 4000 nm wide is represented with the biggest number of 9 cells. Widths of kinetochore space represented with less than five cells (halve the number with the biggest representation) are considered as end values of indicators of the progress of mitosis. Therefore kinetochore space below 3000 nm wide is considered typical for metaphase. To a cell with kinetochore space narrower than 3000 nm, a positive point of mitosis progress is attributed (table 26). Kinetochore space wider than 5000 nm is considered typical for early prometaphase. To those 3 cells, a negative point is attributed (table 26).

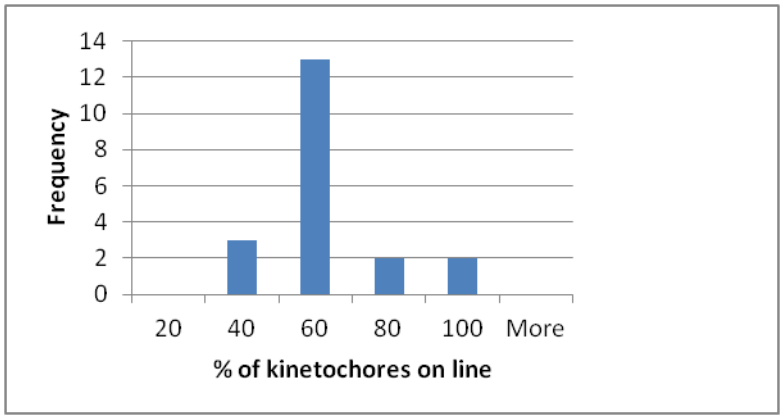

Figure 47. Distribution of mitotic cells with different ratios of sister-kinetochore pairs in the division plane. The division plane is defined as the plane in which most of the lines between sister kinetochores cross. Kinetochores are labeled with antibodies against CENP-A stained with Alexa-Fluor-647. The ratio of sister-kinetochore pairs in the division plane between 40 and 60 % is represented with the biggest number of eleven cells. The ratio of sister-kinetochores pairs in the division plane below 40 %, represented with less than six cells, is considered as end value typical for prophase or early prometaphase. To those three cells, a negative point indicator of the progress of mitosis is attributed. The ratio of sister-kinetochores pairs in the division plane above 60 %, represented four cells, is considered as end value typical for late mitosis, or metaphase. To those four cells, a positive point indicator of the progress of mitosis is attributed.

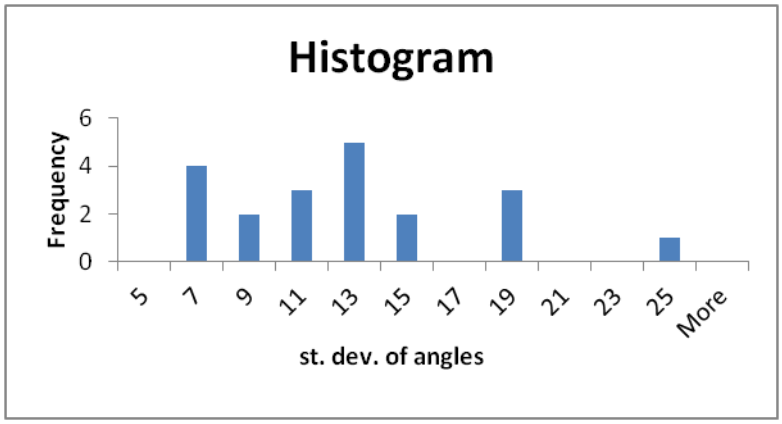

Figure 48. Distribution of mitotic cells with the different standard deviation of angles between lengths between sister-kinetochores (st. dev. of angles). Kinetochores are labeled with antibodies against CENP-A stained with Alexa-Fluor-647.

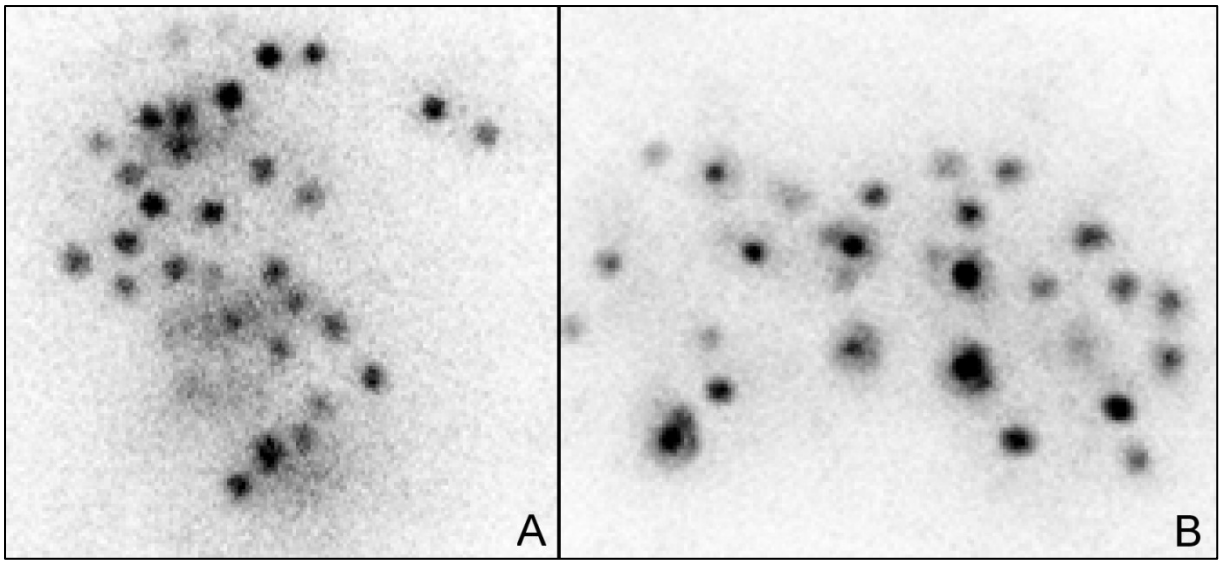

Figure 49. Cells in the very early prometaphase marked as A and B in figure 23 (change of the kinetochore dimensions in regards to the progress of mitosis). **A)** Cell with average cell kinetochore width to length ratio 0.723 and the average cell sister-kinetochore distance 995 nm, marked with A (table 26). **B)** Cell with average cell kinetochore width to length ratio 0.728 and the average cell sister-kinetochore distance 1165 nm marked as B (table 26).

Literature

Allshire RC, Karpen GH. 2008. Epigenetic regulation of centromeric chromatin: old dogs, new tricks? Nat Rev Gen 9:923–937.

Andronov L, Ouararhni K, Stoll, Klaholz BP, Hamiche A. 2019. CENP-A nucleosome clusters form rosette-like structures around HJURP during G1. Nat. Comm. 10: 4436

Amor DJ, Choo KH. 2002. Neocentromeres: role in human disease, evolution, and centromere study. Am. J. Hum. Genet. 71 (4) 695–714.

Betzig E, Patterson GH, Sougrat R, Lindwasser OW, Olenych JS, Bonifacino M, Davidson MW, Lippincott-Schwartz J, Hess HF. 2006. Imaging Intracellular Fluorescent Proteins at Nanometer Resolution. Science 313 (5793):1642–1645.

Bates M, Huang B, Dempsey GT, Zhuang X. 2007. Multicolor superresolution imaging with photo-switchable fluorescent probes. *Science.*317:1749–1753.

Black BE, Foltz DR, Chakravarthy S, Luger K, Woods VL Jr, Cleveland DW. 2004. Structural determinants for generating centromeric chromatin. Nature 430:578-582.

Brinkley BR, Stublefield E. 1966. The fine structure of the Kinetochore of the Mammalian Cells in Vitro. Chromosoma (Berl.) 19: 28-63

Bui M,Dimitriadis EK, Hoischen C, An E, Quenet D, Giebe S, Nita-Lazar A, Diekmann S, Dalal Y. 2012. Cell-Cycle-Dependent Structural Transitions in the Human CENP-A Nucleosome In Vivo. Cell 150: 317–326.

Chan GK, Liu S, Yen TJ. 2005. Kinetochore structure and function Trends in Cell Biol 11(15)

Chan FL, Marshall OJ, Saffery R, Kim BW, Earle E, Choo KHA, Wong LH. 2011. Active transcription and essential role of RNA polymerase II at the centromere during mitosis. PNAS 109 (6): 1979–1984

Cheeseman IM, Desai A. 2008. Molecular architecture of the kinetochore–microtubule interface. Nat Rev Mol Cell Biol 9:33-46.

Cheeseman IM, Hori T, Fukagawa T, Desai A. 2008. KNL1 and the CENP-H/I/K Complex Coordinately Direct Kinetochore Assembly in Vertebrates. Mol Biol Cell 19: 587–594.

Cheeseman IM, Desai A. 2008. Molecular architecture of the kinetochore-microtubule interface. Mol Cell Biol 9 (1)33-48.

Cimini, D. et al.. 2001. Merotelic kinetochore orientation is a major mechanism of aneuploidy in mitotic mammalian tissue cells. J. Cell Biol. 153: 517–527.

Doksani Y, Wu JY, De Lange T, Zhuang X. 2013. Super-Resolution Fluorescence Imaging of Telomeres Reveals TRF2-Dependent T-loop Formation. Cell 155 (2): 345-356

Dong Y, Vanden-Beldt KJ, Meng X, Khodjakov A, McEwen BF. 2007. The outer plate in vertebrate kinetochores is a flexible network with multiple microtubule interactions. Nat Cell Biol 9:516–522.

Dumont S, Salmon ED 2, Mitchison TJ. 2012. Deformations within Moving Kinetochores Reveal Different Sites of Active and Passive Force Generation. Science 337(6092): 355–358.

Dumont S, MitchisonTJ 2009. Force and Length in the Mitotic Spindle. Curr Biol 9: R749–R761.

Eltsov M,MacLeellan KM, Maeshima K, Frangakis AS, Dubochet J 2008. Analysis of crio-electron microscopy images does not support the existence of 30-nm chromatin fibers in mitotic chromosomes in situ. Proc Nat Acad Sci 105(50): 19732-19737

Fei J, Singh D, Zhang Q, Park S, Balasubramanian D, Golding I, Vanderpool CK,Ha T 2015. Determination of *in vivo* target search kinetics of regulatory non-coding RNA. Science 347(6228): 1371-1374.

Finch JT, Klug A 1976. Solenoidal model for superstructure in chromatin Proc Nat Acad Sci USA. 73 (6): 1897-1901)

Foley EA, Kapok TM, 2013.Microtubule attachment and spindle assembly checkpoint signalling at the kinetochore Nat Rev Mol Cell Biol 14(1): 25–37.

Fukagawa T, Earnshaw WC. 2014. The Centromere: Chromatin Foundation for the Kinetochore Machinery. Developmental Cell 30: 496.

Fölling, JM, Bossi H. Bock R, Medda C, Wurm A, Hein B, Eggeling JC, Hell SW. 2008. Fluorescence nanoscopy by groundstate depletion and single-molecule return. Nat. Methods 5:943–945.

Gregan J,Polakova S, Zhang L Tolić-Nørrelykke IM, Cimini D. 2011. Merotelic kinetochore attachment: causes and effects Trends in Cell Biology, 21 (6) 374-381.

Hasson D, Panchenko T, Salimian KJ, Salman MU, Sekulic N, Alonso A, Warburton PE Black BE. 2013. The octamere is the major form of CENP-A nucleosomes at human centromeres. Nat Struct Mol Biol 20(6):687-95.

Heilemann M, Van de Linde S, MukherjeeA, Sauer M. 2009. Hochaufloesende Mikroskopie mit kleinen organischen Farbstoffen, Angew. Chem, 121: 7036 –7041.

Heilemann M, van de Linde S, Schüttpelz M, Kasper R, Seefeldt BA, Mukherjee A, Tinnefeld P, Sauer M. 2008. Subdiffraction-resolution fluorescence imaging with conventional fluorescent probes. Angew Chem Int Ed Engl. *(*47): 6172–6176.

Heintzmann R, Cremer C. 1999. Lateral modulated excitation microscopy: Improvement of resolution by using a diffraction grating. Proc. SPIE. (3568):185–195.

Hell SW. 2007. Far-field optical nanoscopy. Science. (316):1153–1158.

Hellwig D, Hoischen C, Ulbricht T, Diekmann. 2009. Acceptor-photobleaching FRET analysis of core kinetochore and NAC proteins in living human cells. Eur Biophys J 38:781–791.

Hellwig D, Emmert S, Ulbricht T, Doering V, Hoischen C, Martin R, Samora CP, McAinsh AD, Carroll CW, Straight AF, Meraldi, Diekmann S. Dynamics of CENP-N kinetochore binding during the cell cycle. Journal of Cell Science 124: 1–13.

Hellwig D, Münch S, Orthaus C. Hoischen C, Hemmerich P, Diekmann S. 2008. Live-cell imaging reveals sustained centromere binding of CENP-T via CENP-A and CENP-B. J. Biophoton. 1–11

Hemmerich P, Weidtkamp-Peters S, Hoischen C, Schmiedeberg L, Erliandri I, Diekmann S .2008. Dynamics of inner kinetochore assembly and maintenance in living cells. J Cell Biol 180: 1101–1114.

Henriques, R, Lelek, M, Fornasiero EF, Valtorta F, Zimmer C, Mhlanga MM. 2010. QuickPALM: 3D real-time photoactivation nanoscopy image processing in ImageJ. Nature methods 7(5): 339-340.

Hess ST, Giriajan TP, Mason MD. 2006. Ultra-high-resolution imaging by Fluorescence Photoactivation Localization Microscopy. Biophys J 91 (11): 4258–4272.

Hirota T. 2009. Kinetochore stretching inactivates the spindle assembly checkpoint. J Cell Biol 184(3)

Hoffman DB. et al. 2001. Microtubule-dependent changes in assembly of microtubule motor proteins and mitotic spindle checkpoint proteins at PtK1 kinetochores. Mol. Biol. Cell 12: 1995–2009.

Hori T, Amano M, Suzuki A, Backer CB, Welburn J, Dong Y, McEwen BF, Shang YH., Suzuki A, Okawa K. 2008. CCAN makes multiple contacts with centromeric DNA to provide distinct pathways to the outer kinetochore. Cell 135: 1039–1052.

Huang B, Jones A, Brandenburg B, Zhuang X. 2008. Whole-cell 3D STORM reveals interactions between cellular structures with nanometer-scale resolution. Nature methods 5 1047-1052

Joglekar AP, Bouck D, Finley K, Liu X, Wan Y, Berman J, He X, Salmon ED, Bloom KS Molecular architecture of the kinetochore-microtubule attachment site is conserved between point and regional centromeres J. Cell Biol. 181 (4) 587–594.

Jokalainen PT 1967.The Ultrastructure and the Spatial organization of the Metaphase Kinetochore in Mitotic rat cells. J Ultrastruct Res 19: 19-44.

Kajtez J, Solomatina A, Novak M, Polak B, Vukušić K, Ruediger J, Cojoc G, Milas A, Šumanovac Šestak I, Risteski P, Tavano F, Klemm AH, Roscioli E, Welburn J, Cimini D, Glunčić M, Pavin N, Tolić IM. 2016. Overlap microtubules link sister k-fibers and balance the forces on bi-oriented kinetochores. Nature Communication 7:10298-10307.

Klein T, Löschberger A, Proppert S, Wolter S, Van de Linde S, Sauer M. 2010. Live-cell *d*STORM with SNAP-tag fusion proteins. Nature Methods 8: 7-9

Lampson MA, Cheeseman IM. 2011. Sensing centromere tension: Aurora B and the regulation of kinetochore function. Trends Cell Biol. 21(3): 133–140.

Ladrach KS,Fountain JRJr .1986. Malorientation andnabnormal segregation of chromosomes during recovery fromcolcemid and nocodazole. Cell Motil. Cytoskeleton 6: 419–427.

Lidke K, Rieger B, Jovin T, Heintzmann R. 2005. Superresolution by localization of quantum dots using blinking statistics. Opt. Express 13:7052–7062.

Liu D, Vleuge Ml, Backer CB, Hori T Fukagawa T, Cheeseman IM, Lampson MA Regulated targeting of protein phosphatase 1 to the outer kinetochore by KNL1 opposes Aurora B kinase. J Cell Biol 188 (6): 809-820.

Löschberger A,Van de Linde S, DabauvalleMC, Rieger B, Heilemann M, Krohne G, SauerM. 2012. Super-resolution imaging visualizes the eightfold symmetry of gp210 proteins around the nuclear pore complex and resolves the central channel with nanometer resolution. J Cell Sci 125: 570-575.

Löschberger A, Franke C, Krohne G, Van de Linde S, Sauer M. 2014. Correlative super-resolution fluorescence and electron microscopy of the nuclear pore complex with molecular resolution J Cell Sci: 127: 4351-4355

Marshall OJ, Chuen AC, Wong LH, Choo KH. 2008. Neocentromeres: new insights into centromere structure, disease development, and karyotype evolution. Am J Hum Genet 82: 261-282.

Marshall OJ, Marshall OT, Choo A. 2008. Three-dimensional localization of CENP-A suggests a complex higher order structure of centromeric chromatin J Cell Biol 183 (7): 1193-1201.

McClelland SE, Borusu S, Amaro AC, Winter JR, Belwal M, McAinsh AD, Meraldi P. 2007.The CENP-A NAC/CAD kinetochore complex controls chromosome congression and spindle bipolarity. EMBO J 26: 5033-5047.

McEwen BF, Hsieh CE, Mattheyses AL, Rieder CL .1998. A new look at kinetochore structure in vertebrate somatic cells using high-pressure freezing and freeze substitution. Chromosoma 107(6-7): 366-375

McEwen BF, Dong Y. 2010. Contrasting models for kinetochore microtubule attachment in mammalian cells Cell. Mol Life Sci 67:2163–2172.

Mennella V, Keszthelyi B, McDonald KL, Chhun B, Kan B, Rogers GC, Huang B, Agard DA. 2012. Sub-diffraction-resolution fluorescence microscopy reveals a domain of the centrosome critical for pericentriolar material organization. Nat Cell Biol. 14(11): 1159–1168

McEwen BF, Dong Y, VandenBeldt, K. J. 2007. Using electron microscopy to understand functionalmechanisms of chromosome alignment on the mitoticspindle. Methods Cell Biol. 79, 259–293.

McEwen BF, Arena JT, Frank J, Rieder CL. 1993. Structure of the colcemid-treated PtK1 kinetochore outer plate as determined by high voltage electron microscopic tomography. J Cell Biol 120: 301–312.

McEwen BF, Hsieh C-E, Mattheyses AL, Rieder CL. 1998. A new look at kinetochore structure in vertebrate somatic cells using high-pressure freezing and freeze substitution. Chromosoma 107: 366–375.

Musacchio A, Salmon ED. 2010. The spindle-assembly checkpoint in space and time. Nat Rev Mol Cell Biol. 8:379–93.

Nicklas RB, Koch CA. 1969. Chromosome micromanipulation, spindle fiber tension and the reorientation of mal-oriented chromosomes. J Cell Biol 43: 40–50.

Nishino T, Takeuchi K, Gascoigne KE, Suzuki A, Hori T, Oyama T, Morikawa K, Cheeseman IM., Fukagawa T. 2012. CENP-T-W-S-X forms a unique centromericchromatin structure with a histone-like fold. Cell 148: 487–501.

Nishino T, Rago F, Hori T, Tomii K, Cheeseman LM, Fukagawa T. 2013. CENP-T provides a structural platform for outer kinetochore assembly. EMBO J 32(3): 424-436.

Nyquist H. 1928. Certain topics in telegraph transmission theory. IEE Trans 47: 617–644.

Ptacin JL, Lee SV, Garner EC, Toro E, Eckart M, Comolli LR, Moerner W,[2] and Shapiro L.. 2010. A spindle-like apparatus guides bacterial chromosome segregation. Nat Cell Biol. 12 (8) 791-798.

Rabitsch KP et al.. 2003. Kinetochore recruitment of two nucleolar proteins is required for homolog segregation in meiosis I. Dev. Cell 4: 535–548.

Rago F, Gascoigne KE, Cheesman IM. 2015. 2015. Distinct organization and regulation of the outer kinetochore KMN network downstream of CENP-C and CENP-T. Curr Biol 25(5):671-677.

Ribero S, Gatlin JC, Dong Y, Joglekar A, Cameron L, Hudson DF, Farr CJ, McEwen BF, Edward D. Salmon ED, Earnshaw WC, Vagnarelli P 2009. Condensin Regulates the Stiffness of Vertebrate Centromeres. Mol Biol Cell 20: 2371–2380.

Ribero S, Vagnarelli P, Dong, Y, Hori T, McEwen B, Fukagawa T, Flors C, Earnshaw WC. 2010. Super-resolution map of the vertebrate kinetochore. PNAS 107(23): 10484-10489.

Rieder CL, Cole RW, Khodjakov A, Sluder G. 1995. The checkpoint Delaying Anaphase in response to Chromosome Môn orientation is mediated by an Inhibitory signal produced by unattached Kinetochores. J Cell biol 130 number (4): 941-948

Roos UP. 1973. Light and electron microscopy of rat kangaroo cells in mitosis. II. Kinetochore structure and function. Chromosoma 41:195–220.

Rothemund PW. 2006. Folding DNA to create nanoscale shapes and patterns Nature 440: 297-302.

Rust MJ, Bates M, ZhuangX (2006). Sub diffraction-limit imaging by stochastic optical reconstruction microscopy (STORM). Nat Met 3 (20): 793–796.

Saitoh H, Tomkiel J, Cook CA, Ratrie H, Maurer M, Rothfield NF, Earnshaw WC .1992. CENP-C, an autoantigen in scleroderma, is a component of the human inner kinetochore plate, 70(1): 115–125.

Santaguida S, Musacchio A. 2009. The life and miracle of kinetochores. EMBO J 28: 2511–2531.

Schermelleh L, Heintzmann R, Leonhardt H. 2010. A guide to super-resolution fluorescence microscopy J Cell Biol 190(2): 165-175.

Sekulic N, Bassett EA, Rogers D, Black BE. 2010 The structure of (CENP-A–H4)2 reveals physical features that mark centromeres. Nature 467 (7313): 347-351.

Shannon CE. 1949. Communication in the presence of noise. Proc. IRE 37: 10–21.

Silkworth WT, Cimini D. 2012. Transient defects of mitotic spindle geometry and chromosome segregation errors. Cell Div. https://doi.org/10.1186/1747-1028-7-19

Suzuki A, Hori T, Nishino T, Usukura J, Miyagi A, Morikawa K, Tatsuo Fukagawa. 2012. Spindle microtubules generate tension-dependent changes in the distribution of inner kinetochore proteins. J Cell Biol 193 (1) 125–140.

Suzuki A, Badger B, Wann X, DeLuca JG, Salmon E. 2014. The Architecture of CCAN Proteins Creates a Structural Integrity to Resist Spindle Forces and Achieve Proper Intrakinetochore Stretch Development Cell 30(6): 6717–730.

Thompson RE, Larson DR, Webb WW. 2002. Precise Nanometer Localization Analysis for Individual Fluorescent Probes. Biophys J. 82(5): 2775-2783.

Tokunaga M, Imamoto N, Sakata-Sogawa K. 2008. Highly inclined thin illumination enables clear single-molecule imaging in cells. Nature methods, vol 5, no 2, 159-161. Distribution of ESCRT machinery at HIV assembly sites reveals virus scaffolding of ESCRT subunits. Science 343 (6171):653-656

Varma D, Wan X, Cheerambathur D, Gassmann R, Suzuki A., Lawrimore J, Desai A, Salmon ED. 2013. Spindle assembly checkpoint proteins are positioned close to core microtubule attachment sites at kinetochores. J Cell Biol 202: 735–746.

Xu K, Zhong G, Zhuang X. 2013. Actin, spectrin and associated proteins form a periodic cytoskeletal structure in axons. Science. 25; 339(6118): 452-456

Wan XO, Quinn RP, Pierce HL, Joglekar AP, Gall WE, DeLuca JG, Carroll CW, Liu ST, Yen TJ, McEwen BF, Stukenberg PT, Desai A, Salmon ED. 2009. Protein architecture of the human kinetochoremicrotubule attachment site. Cell 137: 672–684.

Westhorpe FG, Straight AF. 2013. Functions of the centromere and kinetochore in chromosome segregation Curr Opin Cell Biol 25:334–340.

Wynne D, Funabiki H. 2016. Heterogeneous architecture of vertebrate kinetochores revealed by three-dimensional super resolution fluorescence microscopy. Mol Biol. Cell 27 (22) 3395-3404

Appendix

Acknowledgments

I would like to thank my supervisor Prof. Dr. Rainer Heintzmann for giving me the opportunity to work on this project, enabling me to work in his optical laboratory and for enabling me to use all the equipment, necessary to build STORM microscope, and to perform *d*STORM experiments. I would also like to thank him for his trust and patience when he gave me the freedom to build a microscope and to perform experiments independently. I would like to thank him for his help and his guidance during my research, and for the reading of the manuscript of my doctoral thesis and all his constructive comments on how to improve the thesis. I would also like to thank him for his formal supervision and attendance at my Ph.D. committee meetings.

I would like to thank my other supervisor Prof. Dr. Stephan Diekmann for enabling me to prepare samples in his bio lab and for his formal supervision and attendance of Ph.D. committee meetings. I would also like to thank to other members of my PhD committee: Dr. Thomas Cremer, Prof. Dr. Andreas Gebert, and Dr. Ingo Kleppe for attending PhD committee meetings and for their usefull comments about my research.

I would like to thank Dr.Martin Kielhorn for teaching me how to build and helping me to build the second and the third version of the *d*STORM microscope and for his help with practical problems with the optical setup. I would also like to thank Dr. Kai Wicker for helping me to build the first version of the STORM microscope and helping me to solve practical problems with the optical setup.
I would like to thank Andreas Kopielski for preparing DNA origami samples and AFM images of the DNA origami.

I would like to thank Jena School of Microbial Communication for giving me the stipend for my work on this project and for funding the chemicals and the part of the equipment used in this work.

I would like to thank my husband Martin Sebastijan for taking care of our three children while I was writing this thesis.

Selbständigkeitserklärung

Ich erkläre, dass ich die vorliegende Arbeit selbständig und unter Verwendung der angegebenen Hilfsmittel, persönlichen Mitteilungen und Quellen angefertigt habe.

Ort, Datum, Unterschrift der Verfasserin

_____

Zussamenfassung

Das Kinetochor ist ein Chromatin-Protein-Komplex auf dem Chromosomenzentromer. Kinetochore binden Chromosomen an die Mikrotubuli des Spindelapparates. Sie erkennen die Anhaftung von Mikrotubuli und regulieren den Fortschritt der Mitose. Der Kinetochor-Proteinkomplex ist auf dem peripheren Zentromer Chromatin aufgesetzt. Es scheint, dass Kinetochore auf Kräfte der Mikrotubuli des Spindelapparates reagieren. Aufgrund des begrenzten Auflösungsvermögens optischer Mikroskope und der Einschränkungen des Elektronenmikroskopie ist die räumliche Anordnung von Kinetochorprotein und Chromatinkomplex ungelöst. In dieser Arbeit wurde menschliches, peripheres Zentromer Chromatin mit CENP-A (Kinetochor-Chromatin im weiteren Text) mit hochauflösender Optik abgebildet. Das Kinetochor-Chromatin ist der Grundbestandteil des Kinetochor-Komplexes. Mit hilfe der direkten stochastischen optischen Rekonstruktionsmikroskopie (dSTORM) wurde ein Auflösungsvermögen von unter 30 nm erreicht und der Aufbau von mehr als 900 Kinetochoren in verschiedenen Teilstadien von Interphase und Mitose wurden aufgenommen.

Kinetochor-Chromatin bildet eine rechteckigen Struktur mit einer Länge zwischen 250 und 400 nm und einer Breite von 150 bis 270 nm. Das Kinetochor-Chromatin besteht aus parallelen und orthogonalen Linien mit 12 bis 75 nm Breite. Das Die Anordnung von Kinetochorchromatin bei Mitose war enger und Linien länger als in der Interphase. In Interphase wurden subtile Änderungen in den Dimensionen der Kinetochorlinien gemessen. Das mitotische Toxin Nocodazol stört die Kinetochor-Chromatin-Organisation und bewirkt die Bildung kompakter Rechtecke. Die beobachtete Änderung der Anordnung des mit CENP-A zusammengesetzten Kinetochorchromatins während des Zellzyklus könnte der physikalische Mechanismus für die Erkennung der richtigen Anhaftung und Positionierung der Chromosomen an die Äquatorialebene sein. Basierend auf der entdeckten Kinetochorstruktur und dem Verhalten im Zellzyklus wird ein neues Schnürsenkel-Modell für den Aufbau und die Funktion von Kinetochorchromatin vorgeschlagen.

Curriculum vitae

Education

2010-2014: doktoral researcher at the Friedrich Schiller University Jena, supervisor; Prof. Dr. Rainer Heintzmann

2002-2008.-University of Zagreb, Faculty of Science, Department of Biology, study of molecular biology, GPA: 4,6 (Excellent)

1998-2002. II High School, Zagreb, graduated with excellent success

Working experience

3. 2014-12.2015: Max Planck Institute of Molecular Cell Biology and Genetics, working on a project: „Forces in the mitotic spindle "

10. 2010- 3.2014: Leibniz Institute of Photonic Technology (IPHT); doctoral research on the project: „High-resolution Direct Stochastic Optical Reconstruction Microscopy of the human kinetochore chromatin "

3.2006 -11.2006: University of Zagreb, Faculty of Science, Department of Molecular Biology: student assistant on the internatinal scientific project „Molecular aspects and mechanistic bases of gamete differentiation, establishment of cell polarity and gamete fusion ".

Scientific publication

Mandula O, Šumanovac Šestak I, Heintzmann R, and CKI Williams: Localisation micrroscopy with quantum dots using non-negative matrix factorisation 2014. Optic-Express Vol 22, 20:24594

Kajtez J, Solomatina A, Novak M, Polak B, Vukušić K, Ruediger J, Cojoc G, Milas A, Šumanovac Šestak I, Risteski P, Tavano F, Klemm AH, Roscioli E, Welburn J, Cimini D, Glunčić M, Pavin N, Tolić IM. 2016. Overlap microtubules link sister k-fibers and balance the forces on bi-oriented kinetochores. Nature Communication 7:10298-10307

Participation on international scientific conferences

• Focus on Microscopy, Konstanz, Germany, 17.-20. 4. 2011.
• International School of Physics "Enrico Fermi"/Microscopy applied to biophotonics, Varenna, Italy, 12.-22.7.2011.
• 47th Winterseminar (Biophisical chemistry, Molecular Biology and Cybernetics of Cell Functions), Klosters, Switzerland, 21.-28.1.2012, poster
• Manfred-Eigen-Gespraeche 2012. Molecules, Light and Life 12.-14.-11. 2012, poster
• MiCom, student conference on microbial communication, Jena -11-2013, presentation

Other

Family status: married and mother of 3 children of age 2, 4, and 6 years

Ivana Šumanovac Šestak

Permissions

UNIVERSITY of TASMANIA | MENZIES Institute for Medical Research

Dr Owen Marshall
Menzies Institute for Medical Research
17 Liverpool St
Hobart, Tas, 7000
Australia

October 30, 2017

To whom it may concern,

I hereby grant permission for Ivana Šumanovac Šestak to use images from the following publication in her thesis:

Marshall OJ, Marshall AT, and Choo KHA. (2008) Three-dimensional localisation of CENP-A suggests a complex higher-order structure of centromeric chromatin. *J Cell Biol.* **183**:1193-1202.

Yours Sincerely,

Owen Marshall

Menzies Institute for Medical Research
Medical Science Precinct
17 Liverpool Street
Hobart Tasmania
7000 Australia

T +61 3 6226 7700
enquiries@menzies.utas.edu.au
www.menzies.utas.edu.au
ABN 30 764 374 782 / CRICOS 00586B

Ivana Šumanovac <sumanovac.ivana@gmail.com>

AW: Kontakt for Andreas Kopielski

Csaki, Andrea // Leibniz-IPHT <andrea.csaki@leibniz-ipht.de> 7. kolovoza 2018. u 09:52 Prima: Ivana Šumanovac Šestak <sumanovac.ivana@gmail.com>

Dear Ivana, no people have a contact more to Andreas. As I was wriϴng you, you can use the AFM images.

Best wishes from the IPHT, Andrea

Dr Andrea Csáki

Head of Workgroup/Nano Biophotonics Leibniz InsϴtuteofPhotonicTechnology, (IPHT) PO Box 100 239,

07702 Jena, Germany Postal adress: A.-Einstein-Str. 9, 07745 Jena Phone: +49-(0)3641-206316, Fax: -206139

andrea.csaki@leibniz-ipht.de http://www.ipht-jena.de

Von: Ivana Šumanovac Šestak [mailto:sumanovac.ivana@gmail.com] **Gesendet:** Montag, 6. August 2018 19:38 **An:** Csaki, Andrea // Leibniz-IPHT **Betreff:** Re: Kontakt for Andreas Kopielski

Dear Dr. Csaki

Sorry to bother you again

As it is written in previous mails, I worked as a PhD student on IPHT and I had a collaboration with Andreas Kopielski. I need a permission to put his AFM images of the DNA origami rectangles in my thesis. Of course I state that he imaged them and prepared them. Unfortunately I can not reach him, although the address you gave me seems to be valid.

Dear Ivana Šumanovac Šestak,

We hereby grant permission for the requested use expected that due credit is given to the original source.

Any third party material is expressly excluded from this permission. If any of the material you wish to use appears within our work with credit to another source, authorization from that source must be obtained.

Credit must include the following components:

Journals: Author(s) Name(s): Title of the Article. Name of the Journal. Publication year. Volume. Page(s). Copyright Wiley-VCH GmbH. Reproduced with permission.

This permission does not include the right to grant others permission to photocopy or otherwise reproduce this material except for accessible versions made by non-profit organizations serving the blind, visually impaired and other persons with print disabilities (VIPs).

Kind regards

Bettina Loycke
Senior Rights Manager
Rights & Licenses

Wiley-VCH GmbH
Boschstraße 12
69469 Weinheim
Germany

www.wiley-vch.de

T +(49) 6201 606-280
F +(49) 6201 606-332
rightsDE@wiley.com

Von: Angewandte <angewandte@wiley-vch.de>
Gesendet: Montag, 14. September 2020 3:35
An: Rights DE <RIGHTS-and-LICENCES@wiley-vch.de>
Betreff: WG: permission to publish a figure from Angew.Chemie. in doctoral thesis

Von: Ivana Šumanovac Šestak <sumanovac.ivana@gmail.com>
Gesendet: Montag, 14. September 2020 2:34
An: Angewandte <angewandte@wiley-vch.de>
Betreff: permission to publish a figure from Angew.Chemie. in doctoral thesis